June 1980 LRP 168/80

A STUDY OF THE FEASIBILITY OF MEASURING THE PLASMA ION TEMPERATURE IN JET BY THOMSON SCATTERING USING A FAR-INFRARED LASER

M.R. Green, P.D. Morgan, M.R. Siegrist and
R.L. Watterson

A Study of the Feasibility of Measuring the Plasma Ion Temperature in JET by Thomson Scattering Using a Far-Infrared Laser

Completed under JET Contract B-Z-412

by

M.R. Green
P.D. Morgan
M.R. Siegrist
R.L. Watterson*

of

Centre de Recherches en Physique des Plasmas,
Association Euratom-Confédération Suisse,
Ecole Polytechnique Fédérale de Lausanne,
21, Avenue des Bains,
CH-1007 Lausanne,
Switzerland.

* now at

Francis Bitter National Magnet Laboratory,
Massachusetts Institute of Technology,
170 Albany Street,
Cambridge, MA 02139, U.S.A.

June 1980

CONTENTS

Contents (cont'd)

Contents (cont'd)

SUMMARY

Thomson scattering using a pulsed far-infrared (FIR) laser, of wavelength $\sim$ 50 - 500 μm, is a potential technique for unambiguously determining the plasma ion temperature in the present generation of large tokamaks under construction. In this report, we present the results of a study into the feasibility of applying the technique to the JET plasma.

We first review the basic principles of Thomson scattering. The performance required from the FIR laser is established for the successful application of the technique using existing detector technology, viz. power $\gtrsim$ 1 MW, pulse duration $\gtrsim$ 1 μsec and line-width $\lesssim$ 50 MHz.

A discussion of the principles of optically-pumped FIR lasers follows, together with an evaluation of the current performance of the FIR laser best suited to our requirements; that employing D_2O as active medium and emitting at 385 μm. The development needed to achieve the required performance from this laser is assessed. We present the design of a D_2O laser for use on JET together with its CO_2-laser pump source.

The principles of heterodyne detection are then discussed and a number of potentially-interesting mixers and detection systems are examined. Errors inherent in the determination of T_i are estimated, using a computer simulation program based on a Monto Carlo technique. A detection system which employs a GaAs-Schottky-diode mixer is proposed for use on JET, with an overall NEP of $\lesssim 3 \times 10^{-19}$ WHz^{-1}.

We consider the outcome of using the proposed laser and detection systems on JET. It is predicted that, over the parameter ranges n_e = 3×10^{13} to 3×10^{14} cm^{-3} and $T_i = T_e$ = 2 to 12 keV, T_i can be determined with an error of less than $\pm$ 20%. Using a pair of large vertical slit ports the achievable spatial resolution is better than 20 cm. A scan across slightly more than half of the vertical plasma diameter is possible, with an average separation of $\sim$ 32 cm between the points of measurement.

Multiple pulsing of the D_2O laser would permit $\sim$ 10 measurements to be made during a 10 sec interval.

Practical details associated with interfacing the diagnostic and JET are discussed. Designs for the input and collection optics, windows and dumps are proposed. The space requirements and those for data acquisition and control are outlined.

The cost of the diagnostic is tentatively estimated as being $\sim$ SFr. 2,000,000, without contingencies. A possible time-schedule for installing the diagnostic on JET by the end of 1983 is given.

Finally, the conclusions of the design study are presented and areas requiring further work are identified.

1. INTRODUCTION

At present, plasma ion temperature in tokamaks is routinely determined from the spectrum of charge-exchange neutrals. In the current generation of large tokamaks under construction, of minor diameters one metre or more, this technique will not be reliable for the plasma interior because the neutrals will have mean free paths shorter than the plasma radius. Spectroscopic analysis of impurity radiation in the ultraviolet will also be unsatisfactory in these plasmas because of their high purity and the relatively-large impurity radiation from their surfaces. Thomson scattering using a pulsed far-infrared (FIR) laser, of wavelength 50 - 500 μm, is a technique which appears very attractive as an alternative to these, provided certain technical problems can be overcome.

In this report, we present a conceptual design of a FIR Thomson-scattering diagnostic to measure T_i in JET. Although such a measurement has yet to be realised on any tokamak, the conclusion of this design study is that the technique is viable and that the development needed to improve the performances of existing laser and detection systems to the required level is achievable using current technology. Furthermore, this development is compatible with the time scale for the construction and operation of JET.

The proposed diagnostic system is based on components which require the least amount of development work and, hence, which have the least number of unknowns associated with them. This was considered preferable to choosing a system which, on paper at least, appeared more attractive but which relied on considerable development. The proposed diagnostic uses a D_2O laser emitting at 385 μm together with a detection system based on a GaAs Schottky-diode receiver. However, in many institutes research on FIR lasers and detectors is being pursued vigorously and it is quite conceivable that a system installed on JET would be different from that described in this report.

Already there exist lasers of sufficient power and detectors of adequate bandwidth and sensitivity at 385 μm to enable a measurement of T_i on a tokamak to be attempted. Indeed, such attempts are currently being made in a number of laboratories. However, as yet the pulse duration for which such power levels can be sustained is insufficient for obtaining accuracies of better than $\pm$ 50% in any determination of T_i.

At CRPP, the laser group is engaged in developing a FIR-laser scattering system with which it will be attempted to measure T_i in the Lausanne TCA tokamak. Much of the effort and development work needed for the successful application of the technique runs parallel with the requirements of a diagnostic for use on JET. A large part of the system described in the conceptual design is already in operation at CRPP or is under construction.

The layout of the report is as follows: In section 2 the principles of Thomson scattering are reviewed and the performance required from the FIR laser is established. Section 3 discusses the principles of FIR laser operation, assesses the present status of such lasers and proposes a system for use on JET. In section 4 the technique of heterodyne detection is examined, a number of suitable mixers are considered and a receiver and detection system for use on JET are described. Section 5 is essentially a discussion of the predicted performance of the scattering system when used on JET; among the topics considered are the ranges of plasma parameters which can be covered and the achievable accuracy and resolution. In section 6 we address ourselves to a number of practical problems associated with the interfacing of the diagnostic and JET. We present, in section 7, a cost estimate for the development, construction and installation of the diagnostic on JET and a tentative time-table for its completion. Finally, in section 8, the conclusions of the design study are presented and areas requiring further work and development are identified.

All tables and figures to which reference is made in the text are to be found at the ends of the relevant sections.

2. GENERAL CONSIDERATIONS

In this section we briefly review the principles of Thomson scattering and consider the application of the technique to measuring ion temperature in a tokamak plasma. The performance required from the FIR laser is discussed in terms of laser power, spectral purity and laser pulse duration.

2.1 A Brief Review of Thomson Scattering

The principles of using Thomson scattering to measure various plasma parameters are now well established (1).

Scattering of electromagnetic radiation from a plasma is a three-wave interaction, Figure 2.1.1. An incident e.m. wave, of frequency υ_o and wavelength λ_o, interacts with electron density fluctuations, characterised by υ_f and λ_f, to produce an e.m. wave, of frequency υ_s and wavelength λ_s, at an angle Θ to the incident wave. Momentum conservation requires that $\underline{k}_s = \underline{k}_o + \underline{k}_f$, where $|\underline{k}| = 2\pi/\lambda$. Neglecting momentum transfer between photons and electrons, $|\underline{k}_s| = |\underline{k}_o|$. Hence $|\underline{k}_f| = 4\pi \sin(\Theta/2)/\lambda_o$. Only periodic fluctuations in a direction parallel to $\underline{k}_f$ and of wavelength $2\pi/|\underline{k}_f|$ will be detected. We may determine the scale length and propagation direction of the fluctuations that will be observed in any scattering experiment by a judicious choice of the collection angle θ and the laser wavelength λ_o.

When $\alpha = (k_f\lambda_D)^{-1} << 1$, where λ_D is the Debye length, $2\pi/|\underline{k}_f| << \lambda_D$ and we only detect uncorrelated electron density fluctuations. The scattered radiation is Doppler broadened due to the electron thermal motion, Figure 2.1.2a. For a plasma in thermal equilibrium, the spectrum is a Gaussian of half-width $2\,\underline{k}_f|v_e|/2\pi$, where v_e is the electron thermal velocity, which is thus proportional to $\sqrt{T_e}$. When

$\alpha >> 1$, $2\pi/|\underline{k}_f| >> \lambda_D$ and we observe the correlated motions of the electrons, e.g. due to scattering off electron clouds Debye-shielding the ions and off plasma waves. If $T_e \stackrel{\sim}{=} T_i$, the scattered-radiation spectrum is as shown in Figure 2.1.2b. The width of the central ion feature is proportional to $\sqrt{T_i}$ for a thermal plasma. The two shoulders arise from scattering off ion-acoustic waves and the two detached features are due to electron plasma waves.

Two phenomena could cause problems in an attempt to measure T_i by Thomson scattering. The first arises because the presence of impurity ions in the plasma can greatly distort the ion feature (2). Even concentrations as little as 10 ppm of highly-ionised Mo or W can be detected, the heavy ions manifesting themselves as an intense narrow spike at the centre of the feature which is due to the fundamental ions of the plasma. Lighter impurities of lower charge, such as O, have a broader spectrum (due to their higher velocity), which is much less intense (because their Debye-shielding electron clouds contain fewer electrons and the spectrum is broader). Generally, the high-frequency part of the spectrum of the fundamental ions is not much changed by the presence of impurities at a concentration where the tokamak plasma might still be termed "clean". Under this condition, a reasonably-accurate value of T_i can be extracted from the upper half of the frequency spectrum. With adequate laser power and high spectral resolution it should be possible to determine a value of the effective charge z_{eff} from the low frequency part of the ion feature, although this would be an ambitious undertaking.

The second difficulty would arise if the tokamak plasma had a high level of microturbulence such that the radiation scattered off electron density fluctuations due to this was more intense than the radiation scattered off fluctuations due to ion thermal motion. In this event, the plasma ion temperature could not be determined from the spectrum of scattered radiation. However, the technique could now be

used to obtain valuable information concerning the spectrum of turbulence in the plasma. In any case, provided α is not much greater than unity, in a stable tokamak discharge it should be possible to select a direction for $\underline{k}_f$ such that the level of the fluctuations due to microturbulence, in the high-frequency part of the spectrum due to ion thermal motion, is negligible.

In a tokamak plasma, the combination of high temperatures ($T \sim 1$-10 keV) and low densities ($n \sim 10^{13}$-10^{14} cm^{-3}), results in a relatively-large Debye length ($\lambda_D \sim 0.1$mm). Using an optical laser, the wavelength λ_o would be so short (< 1 μm) that in order to observe cooperative scattering, i.e. to achieve a value of $\alpha > 1$, collection angles θ of less than 0.1^o would be needed. This would result in extremely-poor spatial resolution, since scattered light would be collected from along almost the whole length of the incident light beam in the plasma. Using a CO_2 laser, of wavelength 10.6 μm, collection angles of a degree or so at most could be used, resulting in rather poor resolution (3). However, using FIR lasers of wavelength 50 μm, or more, the collection angles that would be used are sufficient to permit good spatial resolution.

2.2 The Performance Required from the FIR Laser

Currently, the pulsed FIR lasers that are the most developed are those employing heavy-water vapour as active medium, which is pumped by the output of a pulsed CO_2 laser (4). D_2O exhibits strong lasing action on one of three principal wavelengths, viz. 66, 114 and 385 μm, when excited by the appropriate CO_2-laser emission line. In principle, this permits the choice of three collection angles θ for a fixed value of the scattering parameter α. Taking "typical" tokamak plasma parameters ($n_e = 3 \times 10^{13}$ cm^{-3} and $T_e = T_i = 2$ keV) for $\alpha = 1.2$ and using the above wavelengths in increasing order we obtain the following angles: 8.3^o, 14.3^o and 49.8^o.

At present, it is envisaged that the development of the D_2O laser will be continued until its performance meets the requirements of a scattering measurement. This performance, in terms of output power, pulse duration, beam quality and emission line-width, is not only governed by the parameters of the plasma to be studied but also by the characteristics of the detector to be used to record the spectrum of scattered radiation.

The FIR detectors that would be used to record the ion feature have a relatively-high level of internal noise, termed noise equivalent power (NEP), when used in a video or photon-counting mode. The NEP may be considerably reduced if a heterodyne detection system (5) is used, in which the scattered signal is mixed at the detector with the output of a local oscillator. Even so, in a scattering measurement, under most conditions it is the mixer or IF amplifier that will be the dominant source of noise rather than, for example, radiation from the plasma.

At 385 μm a GaAs Schottky diode or a Nb : Nb Josephson junction may be used (6). These have wide band-widths, many GHz, and a good NEP, $\lesssim 3 \times 10^{-19}$ WHz^{-1}. However, they are rather delicate devices and because of their point-contact construction it is not easy to couple radiation into them efficiently. It is unlikely that these devices can be made to operate satisfactorily below a wavelength of $\sim$ 250 μm. At 66 and 114 μm a Ga : Ge photoconductive mixer (6) appears to be the most promising device currently available. Whilst a fast response and a good NEP have been achieved independently in this mixer, these two requirements are mutually conflicting. Consequently, while a band width of $\gtrsim$ 1 GHz is realisable, the NEP associated with this is unlikely to be better than $\sim 5 \times 10^{-18}$ WHz^{-1}, without further development. However, these detectors are quite robust and have an area of several mm^2 so that efficient coupling of radiation into them is straightforward.

In general, either the receivers themselves or the associated recording electronics are limited to band widths $\Delta\nu$ of a few GHz - this necessitates the choice of the differential scattering vector $\underline{k}_f$ such that the Doppler broadening due to ion thermal motion, $|\underline{k}_f| v_i/\pi, \lesssim 2$ GHz. Hence, in order to observe Doppler broadening in the scattered signal the emission line-width of the FIR laser must be relatively narrow - a half width of $\sim 50 - 75$ MHz is required to achieve this. It is also important that the output from the laser propagates in the TEM_{oo} mode, to ensure the lowest beam divergence and to achieve focusing to a diffraction-limited spot in the plasma.

For $\alpha > 1$, the power P_S scattered in the ion feature by the plasma is related to the laser power P_o incident on it by (1)

$$P_S = P_o \cdot n_e \cdot \ell \cdot d\Omega \cdot r_o^2 \cdot S(k),$$

where n_e is the plasma electron density, ℓ is the interaction length over which scattered radiation is collected ($\ell = 2r/\sin\Theta$ is the spatial resolution, where r is the radius of the focused spot), $d\Omega$ is the collection solid angle, $r_o^2 = (e^2/m_e c^2)^2$ is the Thomson differential cross-section for incident radiation polarised normal to the plane of scattering and $S(k) \simeq \alpha^4/((1 + \alpha^2)(1 + 2\alpha^2))$ is the integrated dynamic form factor for the ions.

The maximum solid angle that can be employed is limited by the condition (5), necessary for heterodyne detection, that the collection etendue $\pi r^2 d\Omega \lesssim \lambda_o^2$, i.e. $d\Omega \simeq \lambda_o^2/\pi r^2$ - this preserves phase coherence across the wavefront of the collected radiation. For a Gaussian beam propagating in the TEM_{oo} mode, the smallest diameter to which it can be focused is limited by diffraction and is given by $d = 1.27\, F\lambda$, where F is the f-number of the focusing element and the diameter is defined at the e^{-2} intensity points. However, it is necessary to ensure that this diameter is large enough to accommodate many wavelengths λ_f of the fluctuation being observed, otherwise $\underline{k}_f$ is poorly defined (3). Since $\lambda_f = 2\pi/|\underline{k}_f| = \lambda_o/2 \sin(\Theta/2)$, if we want 2r to be at least 10 λ_f, we require that $r \gtrsim 2.5\, \lambda_o/\sin(\Theta/2)$. Hence, focusing to the diffraction-limited spot size is not always desirable.

We may rearrange the above equation relating P_S to P_o, defining Θ by the band-width restriction of the detection system, i.e. $\sin(\Theta/2) = \Delta\nu\ \lambda_o/4\ v_i$, and taking the other constraints discussed into account, to calculate the power P_o necessary to achieve a scattered power P_S that equals the noise power $P_N = \Delta\nu \cdot NEP$ - the product of the noise equivalent power and band width of the receiver. Thus, for a D_2 plasma,

$$P_o = 1.26 \times 10^{25}\ \Delta\nu\ \sin\left[2\sin^{-1}\left\{\frac{\Delta\nu\ \lambda_o}{3.91\times10^6\sqrt{T_i}}\right\}\right]\ \frac{F}{n_e\lambda_o}\ \frac{NEP}{S(k)}\ . \qquad 2.2.1$$

For a tokamak plasma with $n_e = 3 \times 10^{13}$ and $T_e = T_i = 2$ keV, using a wavelength $\lambda_o = 385$ μm, with a receiver of NEP = 3×10^{-19} WHz^{-1} and band width $\Delta\nu = 2$ GHz, and for a focusing element with f-number F = 40, then $P_o = 1.0$ MW. The necessary scattering angle is $\Theta = 52.2^o$ giving a scattering parameter $\alpha = 1.15$. We will take this figure of 1 MW as being representative of the laser power needed, for further considerations of signal-to-noise ratios.

Consider a detector and recording system of total bandwidth B divided into N_c channels. For heterodyne detection, the overall signal-to-noise ratio S in any channel is given by (3)

$$S = \frac{P_S}{P_S + P_N} \cdot \sqrt{1 + \frac{B \cdot \tau}{N_c}}\ ,$$

where P_S is the scattered power, $P_N = B \cdot NEP$ is the noise power and τ is the laser pulse duration. In section 4.3 it is shown that the optimum signal-to-noise ratio is obtained when the FIR laser energy is delivered in a time τ so that $P_S = P_N$. Furthermore, in the same section it is shown, from the results of a computer simulation program , that in order to determine the plasma ion temperature with an accuracy of better than $\pm$ 20% a signal-to-noise ratio S of at least 7 is required.

Thus, using a receiver of band width 2 GHz and dividing the spectrum into 10 channels, we see from the above equation that a value of $S \gtrsim 7$ is achieved for a laser pulse of duration $\gtrsim 1$ μsec.

In summary, we require a FIR laser output propagating in the TEM_{oo} mode, of power $\sim$ 1 MW, of pulse duration $\gtrsim$ 1 μsec and of line width $\sim$ 50 MHz FWHM.

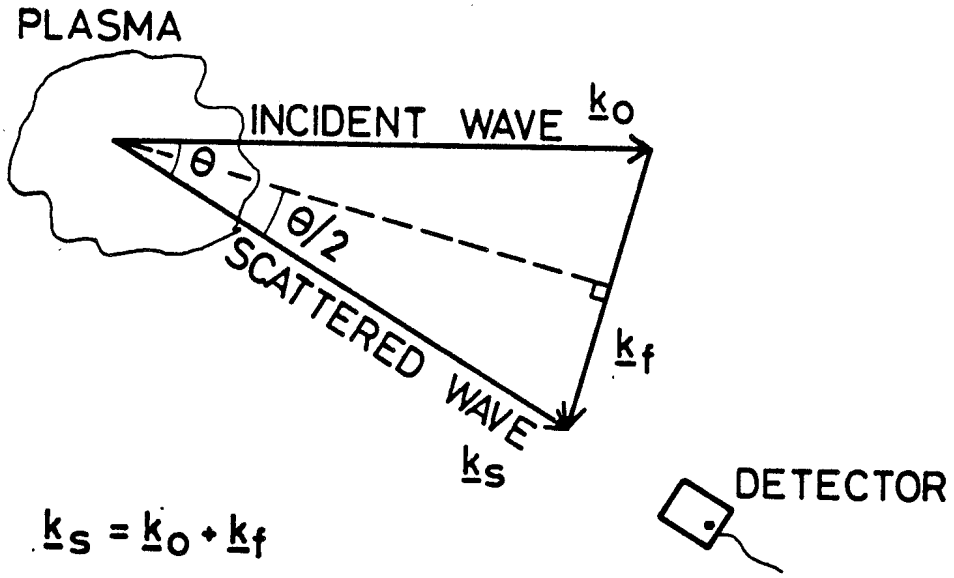

$$\underline{k}_s = \underline{k}_o + \underline{k}_f$$

$$|\underline{k}_f| = 2|\underline{k}_o| \sin(\theta/2) = \frac{4\pi}{\lambda_o} \sin(\theta/2)$$

Figure 2.1.1 : Vector Diagram of the Scattering of an E.M. Wave by a Plasma

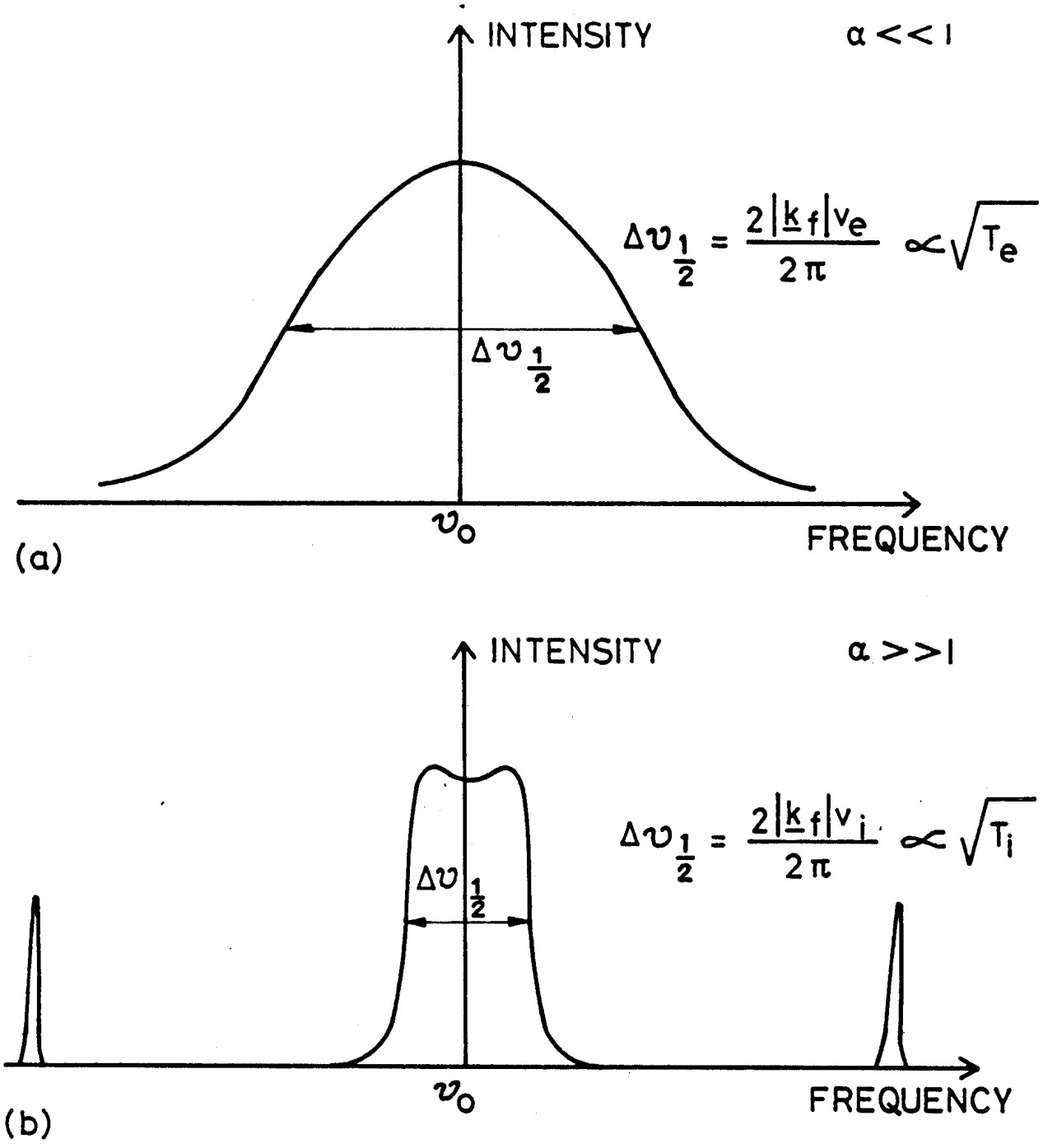

Figure 2.1.2 : Electron and Ion Features for Scattering from (a) Uncorrelated and (b) Correlated Density Fluctuations

3. FAR-INFRARED LASERS

In this section the generation of far-infrared (FIR) radiation suitable for an ion-temperature measurement on JET is discussed. Where it clarifies the dénouement, some principles of the physics of optical pumping are explained. Two FIR lasers are described; namely a high-power pulsed device, the origin of the radiation to be scattered and a low power FIR source for use as the local oscillator to heterodyne with the scattered signal. The energy for the former device is supplied by a large CO_2-laser system. Three design philosophies for this system are considered and the proposed scheme described in some detail. The section is concluded with a summary of the system proposed for use on JET.

3.1 The Pulsed FIR-Laser

The more important specifications for the pulsed FIR-laser have been derived in section 2.2. These are summarized in table 3.1.1, together with a number of additional requirements.

Table 3.1.1

A Summary of the More important Specifications for the Pulsed FIR-Laser

a. Wavelength, λ, : 100 μm $\lesssim \lambda \lesssim$ 400 μm.
   (i.e. 750 GHz $\lesssim \nu \lesssim$ 3000 GHz)
b. Line-width, $\Delta\lambda$: $\Delta\lambda \leq 50$ MHz
c. Pulse duration, T, : $T \geq 1$ μs
d. Power level, P, : $P > 1$ MW
e. Pulse shape : flat topped
f. Single transverse mode
g. Plane polarized

Implicit in the criteria is that there exist a suitably sensitive mixer and local oscillator source, also that any broad background radiation from the laser is of an extremely low level.

Conventional excitation techniques (e.g. electron impact, chemical, energy transfer, etc.) are poorly suited to the production of intense FIR radiation via stimulated emission. This is because of the small energy difference between the initial and final lasing states. Only optical pumping offers us a satisfactory state-selective excitation.

3.1.1 Principles of Optically-Pumped FIR Lasers

The basic principles of optically-pumped FIR lasers are now generally well understood (7-9). In Figure 3.1.1, we illustrate the processes leading to the achievement of a population inversion and FIR laser emission, for the simple case of a polar symmetric-top molecule such as CH_3F. A chance near-frequency coincidence between the emission line of the pump laser, generally emitting in the infrared, and a certain vibrational absorption line (transition $\nu = 0,J \rightarrow \nu = 1,J$) of each of an ensemble of the polar molecules results in the selective population of a rotational level ($\nu = 1,J$) in an excited vibrational state. In general, the coincidence must be within a few hundred MHz. A population inversion is achieved between adjacent rotational levels ($\nu = 1,J$ with respect to $\nu = 1,J-1$). Because of the high permanent dipole moment of each molecule the active medium has a high gain and laser emission occurs as a result of purely-rotational transitions ($\nu = 1,J \rightarrow \nu = 1,J-1$). Frequently, there is additional laser emission due to accompanying cascade transitions ($\nu = 1,J-1 \rightarrow \nu = 1,J-2$) and refilling transitions ($\nu = 0,J+1 \rightarrow \nu = 0,J$). For frequency offsets between pump and absorption line of more than a few hundred MHz, under certain conditions of molecular concentration and pump intensity the emission process is of the stimulated-Raman type.

In principle, optical pumping of an active medium using a laser source is undesirable because of the inherent low efficiency in pumping one laser with another. However, in the case of pulsed FIR lasers there is generally no broad-band pumping mechanism that will selectively channel energy into the desired upper state because the rotational levels are so closely spaced. Thus, we usually find that excitation methods are restricted to selective laser pumping which, in fact, works well for the generation of coherent FIR radiation. The most widely used pump source is the pulsed CO_2 TEA laser, which is one of the most highly-developed lasers and is capable of generating high intensities at relatively-good efficiencies. Furthermore, with over 150 emission lines between approximately 9.1 and 11.3 μm, it is possible to match the output frequency of the laser to vibrational modes in a wide variety of molecules. This is demonstrated by the existence of well over 1000 FIR laser lines between about 40 μm and 2 mm (10, 11).

Intense FIR pulse generation cannot be achieved using conventional Q-switching techniques because, due to molecular collisions, the short lifetime of the upper rotational levels makes significant energy storage impossible. This lifetime is typically 10 nsec at 1 torr pressure; that of the excited vibrational state is at least four orders of magnitude greater. Under the conditions of saturating pump and FIR intensities, the power extraction from a FIR laser is proportional to the rate of pump absorption from the ground-state rotational level. This process is limited by the collisional refilling of the absorbing ground state and by the emptying of the upper rotational laser states, both of which occur at the rate $\nu_r \simeq 10^8 \text{ sec}^{-1} \text{ torr}^{-1}$. If n_m is the molecular density and f is the fraction of molecules in the ground state at equilibrium, then the maximum pumping rate will be $\nu_p = f n_m \nu_r$. The maximum FIR power that can be extracted is $P_{FIR} = 0.5\, h\nu_{FIR}\nu_P (\text{Wcm}^{-3})$.

There is an optimum working pressure, governed by the pump duration and by molecular dynamics, above which the FIR output decreases due to a "bottleneck" effect. Molecules are pumped at a maximum rate ν_p until the limiting excited vibrational-state population 0.5 n_m is reached. The population of the ground and excited vibrational states are now equal, the rotational levels achieved thermal equilibrium and FIR laser emission ends. The time scale for this to occur is $\tau \simeq 1/2\ f\nu_r$. In symmetric top molecules, we can take f to be about 1% at best, which means for a pump pulse of order 100 nsec we must maintain the working pressure below about 5 torr or the collision rate becomes too high for efficient FIR power extraction. Taking a wavelength of 0.5 mm, and at a molecular density set by the 5 torr limit, the maximum FIR power that can be generated is $P_{FIR} \simeq 150$ kW/litre. It is clear that in order to reach power levels of greater than 1 MW, systems of large volume will be needed.

There exist considerable difficulties in obtaining simultaneously high powers and a narrow line width from optically-pumped FIR lasers, the details of which can be found elsewhere, for example (4). The basic problem is the presence of a superradiant background of low intensity spread over a broad frequency range superimposed on the main narrow-band signal, termed amplified spontaneous emission (ASE).

In 1977 there was a significant advance in the understanding of the optically-pumped mechanisms with the demonstration that the 66-μm line of D_2O is produced by stimulated Raman emission (12). The difference between this type of emission and laser emission may be understood by reference to Figure 3.1.2(a). We depict the three rotational levels involved in FIR emission by optically-pumped molecules. Level 1 is in the ground vibrational state, level 2 is in an excited vibrational state and level 3 is adjacent to 2. A laser process consists of two separate steps involving single-photon transitions at the pump and FIR wavelengths. In the first step, the molecule absorbs a pump photon, of wavelength corresponding to the energy difference between levels 1 and 2, and is excited from level 1 to 2. Subsequently, in the second step, the excited molecule undergoes a FIR-laser transition by stimulated emission from level 2 to 3, emitting a FIR photon corresponding to the difference in energy between these levels. The two steps are uncorrelated in time.

The Raman effect is the inelastic scattering of photons by a quantised system (13). If the molecules in the system can undergo a transition of frequency ν_t the non-linear interaction of the incident radiation, of frequency ν_i, with the system, the polarisability of which is modulated at frequency ν_t, generates scattered radiation at frequencies $\nu_R = \nu_i \mp \nu_t$ (the Stokes and anti-Stokes lines). These components have random phases since the vibrations of molecules are uncorrelated. Essentially, the Raman effect results in isotropic emission, of intensity $\sim 10^{-6}$ of that incident. In the case of laser irradiation, as the incident intensity rises so that part of the Stokes radiation which is coherent with it plays an increasingly-important role. The interaction of the laser and Raman fields in the medium generates a frequency component $\nu_i - \nu_R$, i.e. ν_t. This component forces the molecules into resonant vibration, the motion modulates the laser field resulting in Raman scattering of greater intensity which, in turn, leads to more vigorous molecular vibration. For sufficient laser intensity, the process builds up and stimulated Raman scattering results in the generation of coherent radiation at high conversion efficiencies.

Returning to Figure 3.1.2(b), stimulated Raman emission is evidently a two-photon process; a photon is absorbed from the pump field and simultaneously a photon is emitted into the Raman field (at the FIR wavelength), the molecule being excited from level 1 to 3. A population inversion between levels 2 and 3 is not required - unlike in a laser process - indeed level 2 itself need not exist. However, the process is resonantly enhanced by the proximity of level 2. If the pump frequency is off resonance by $\Delta\nu$ with the frequency difference representing the energy between levels 1 and 2, then the FIR emission will also differ by $\Delta\nu$ from the frequency corresponding to the energy difference between levels 2 and 3. In principle, a Raman process can be twice as efficient as a laser process in generating FIR radiation. In the former case, one FIR photon is emitted for each pump photon absorbed whilst in the latter case once 50% of the molecules - each of which was excited by absorbing a pump photon - have emitted a FIR photon a population inversion no longer exists and lasing

ceases. Also, the Raman process relaxes the condition that a close coincidence, within a few hundred MHz, is needed between the centres of the pump and absorption transitions.

Spectroscopic data had shown that the line centre of the 9P(32) pump line was separated by $\sim$ 1.4 GHz from that of the absorbing vibrational transition of D_2O leading to FIR emission at 66 μm and at 50 μm (the latter is due to a refill transition). Careful measurements showed that the emission lines were detuned from their respective transitions also by about 1.4 GHz, when a CO_2 laser confined to working on a single longitudinal mode on line centre was used as pump (12). Subsequent work (14) showed that emission at 385 μm, where the frequency difference between the line centres of the 9R(22) pump line and the absorption transition is about 320 MHz, was also due to a stimulated Raman process. The broad line-width due to ASE in D_2O lasers could now be explained in terms of the broad line-width ($\sim$ 1.5 GHz) of the CO_2 laser pump - each frequency increment of the pump beam, off resonance with the absorbing transition, giving rise to FIR emission detuned by the same amount. It thus became apparent that a narrow-line-width pump was necessary to achieve FIR emission of narrow line-width.

A survey of the several thousand candidate gases/transitions shows that it is the 385 μm line of D_2O that comes closest to satisfying those specifications listed in table 3.1.1 at the beginning of this section. However because of the restricted access to the JET plasma, and to minimise the plasma-noise contribution that arises from e.c.e. emission a laser operating in the 150 - 250 μm wavelength range would be preferable. In the following sub-section a FIR laser and pump source are described, designed primarily for 385 μm, but of sufficient flexibility to require little change should a superior gas/transition be found.

3.1.2 FIR Laser Design

Figure 3.1.3 shows the vibrational and rotational levels of D_2O of interest. The 9.26 μm transition of CO_2 pumps D_2O between the 5_{33} rotational level in the 000 ground vibrational state and the 4_{22} level of the first excited 010 vibrational state. The dashed level just below the 4_{22} level shows that the line-centre of the 9R(22) pump transition of CO_2 is lower in energy than that required for line-centre pumping of D_2O by 320 MHz (15,16), and the shaded area shows the region over which the 9R(22) transition can be tuned (at atmospheric pressure) (17). The characteristics of the 385 μm transition of D_2O have been extensively studied by Woskoboinikow et al (17). Some of the conclusions of their study are listed below.

A) The 385-μm transition of D_2O is definitely a stimulated Raman transition and its frequency is tuned by the pump frequency.

B) The D_2O line-width is reduced considerably when pumping with a single-mode CO_2 line. This is another indication of a Raman transition.

C) Maximum output of the D_2O laser is frequency off-set from the D_2O low-power absorption line centre, and the conversion efficiency of CO_2 laser energy shows a broad minimum near the D_2O line-centre and maxima away from it, Figure 3.1.4.

D) The conversion efficiency, of CO_2 laser energy to D_2O laser energy, is considerably larger when pumping with a single-mode line as compared to the efficiency when pumping with a multi-mode line.

Both the FIR pulse-shape and the polarization are determined by those of the pump pulse, i.e., they are independent of the FIR oscillator resonator configuration. Thus, what is required from this resonator

is as follows :

a) A Large Volume. As we have mentioned previously, there is an upper limit to the extractable power per unit volume of pumped gas, and even before this limit is reached, the decrease in the conversion efficiency becomes prohibitive. For the transition of interest, the 385 μm line of D_2O, about 30 kW/litre can be extracted with an acceptable conversion efficiency (0.25%, single mode pump). Consequently an oscillator volume of $\gtrsim$ 33 litres is required.

The FIR resonator can incorporate a frequency-selective element, e.g. a Fox-Smith interferometer (4). However, it is more simple to arrange that the overall resonator length, L, be such that the frequency difference between adjacent cavity modes $\Delta\nu$ (given by $\Delta\nu = \frac{2L}{c}$) is somewhat greater than the frequency-width of the FIR gain, $\Delta\nu_{FR}$, thereby ensuring that oscillation only takes place on a single longitudinal mode. Since $\Delta\nu_{FR}$ is typically $\sim$ 25 MHz for narrow band pumping, $\Delta\nu$ should be $\sim$ 30 - 40 MHz, i.e. L should not exceed 400 cm. This value has been confirmed experimentally (18). Consequently, for the necessary volume of $\gtrsim$ 33 litres the beam diameter should be $\gtrsim$ 10 cm. Such beam diameters are readily achievable. Diameters of greater than 15 cm are to be avoided owing to the cost and difficulty in fabricating such large diameter optics.

b) Transverse Mode Control. The diameter to which the laser beam is to be focussed in the plasma is subject to conflicting constraints, discussed in section 2.2. Briefly, to obtain the best spatial resolution the beam waist should be as small as is possible. However, it is necessary to ensure that the diameter is large enough to accommodate many wavelengths of the fluctuation being observed. By substituting the values arrived at in section 6.2 into the expressions given on page 10, we find that for 385 μm the diffraction limited spot size of a Gaussian beam propagating in the TEM_{00} mode satisfies these constraints. Control over the transverse mode structure of the FIR laser is more easily determined by the FIR resonator itself rather than by the pump radiation. Consequently, the resona-

tor should provide sufficient discrimination against high order modes to ensure that oscillation takes place only for the lowest order mode.

c) Optimum Output Coupling. Laser efficiency depends on, amongst other things, the cavity feedback; it is an advantage then to be able to vary its value so as to select the optimum.

d) Small Intra-Cavity Losses. These should be as low as possible.

e) Efficient Coupling of the pump energy to the D_2O vapour.

Our proposed design, a folded unstable resonator* is shown schematically in Figure 3.1.5.

For single-transverse-mode oscillation from high-power large-diameter lasers, the unstable optical resonator has many attractive properties (19). Using such a resonator, excellent transverse-mode selection and optimal output coupling may be achieved using all reflective optics.

The CO_2 pump-beam enters the evacuated chamber by a salt window, then passes through a free-standing fine-wire grid. This grid is constructed from parallel strands of 5 μm diameter wire with a spacing between the strands of 50 μm (20). It is relatively transparent to the pump radiation, transmitting more than 80%. The reflectivity of a metal grid becomes significant for wavelengths which are longer than the grid spacing (for polarized radiation the E-vector should lie parallel to the wires). At a wavelength of 385 μm the reflectivity

---

* The results of our parametric study of a D_2O FIR oscillator having an unstable resonator can be found in reference 21.

of such a structure can exceed 95%. The selection rules of quantum mechanics dictate that the 385 μm transition produces radiation preferentially polarized perpendicular to that of the pump beam ($\Delta J = \overline{+} 1$). As a consequence, the E-vector of the pump is arranged to be perpendicular to the direction of the wires, as shown in the figure.

The mirror separation is 400 cm and the active diameter 15 cm. At the working pressure of 3 - 5 torr approximately 75% of the incident CO_2-pump energy is usefully absorbed by the D_2O. The remaining energy is partly absorbed, partly transmitted by the polyethylene output window. This thin window is mechanically supported by a an open metallic grid, which is optically transparent. This window is tilted at 10^o to the optic axis to (a) prevent reflected pump radiation from returning up the amplifier chain, and (b) to avoid the formation of a sub-cavity between it and the concave mirror. Pump radiation is back-reflected too by the convex mirror, which causes it to diverge. The CO_2-laser amplifier is situated some tens of meters distant from the FIR oscillator. Consequently, the solid angle subtended by the amplifier window is very small. It is important that pump (or parasitic 10.6 μm) radiation feedback be kept small in this way if self-oscillation of the CO_2-amplifier is to be avoided.

The output of the laser will comprise a mixture of different wavelength radiations; namely, 385 μm, 359 μm (a cascade transition) and 239 μm (a refill transition). An intra-cavity grating can be used to suppress oscillation on these lines (18). However, since they are not competing (i.e. alternative relaxation pathway) transitions, it is not apparent that any advantage is to be had by their suppression. It is not evident either that they need be separated at all as only the 385 μm wavelength will fall within the bandwidth of the mixer.

For a design of similar dimensions and pumped on CO_2 line-centre with a single-longitudinal mode laser beam, FIR powers of approximately 1 MW of duration 100 ns have been achieved with a conversion efficiency, ε_{FIR}^{385}, of 0.26%, (18).

Consequently, to extend the duration to 1 μs a total pump energy of 390 Joules is required.

At a frequency displaced by $\mp$ 0.75 GHz away from the CO_2 line-centre frequency, ε_{FIR}^{385} rises to 0.4% (see Figure 3.1.4) and consequently only 250 Joules are necessary; this option is considered in greater detail in the next sub-section. These figures together with some other major specifications of the pump laser-beam derived in the foregoing discussion are summarized in table 3.1.2.

Table 3.1.2

A Summary of the Specifications of the CO_2-Pump Beam

CO_2-Laser transition		:	9P(22)
Approximate wavelength		:	9.260 μm
Minimum duration		:	1 μs
Power,*	(a) at CO_2 line-centre	:	390 J/μs
	(b) at $\mp$ .75 GHz off line-centre	:	250 J/μs
Line width		<	25 MHz
Temporal pulse shape		:	flat topped
Polarization		:	plane

* For pump frequencies still further displaced from line-centre even lower powers may be sufficient.

3.2 The Pulsed CO_2 Laser System

The specifications of the optical pump pulse have been discussed and defined in the previous section and summarized in table 3.1.2.

Here we describe how these criteria may be realized.

There are 3 obvious approaches to the problem of the pulsed CO_2-laser system :

(A) Using one large oscillator, obtaining a single longitudinal mode by means of a low pressure section (22).

(B) Using one large oscillator, obtaining a single longitudinal mode by means of injection tuning (23).

(C) To amplify a signal from a small, low energy oscillator (21).

Figure 3.2.1 illustrates these systems. Some of the pros and cons of each approach are listed and compared in table 3.2.1.

We have adopted the oscillator-amplifier arrangement. It offers the greatest control over, and flexibility of, the pump pulse. It is the only arrangement which has demonstrated (a) single mode operation for pulse lengths of >300 ns; and (b) tunability from line-centre operation.

TABLE 3.2.1

A COMPARISON BETWEEN THREE APPROACHES TO THE DESIGN OF A HIGH ENERGY PUMP LASER SYSTEM

Optical arrangement	Pros	Cons	Comments
1. Large Oscillator with low pressure section	Stable Efficient Simple	Line-centre operation only. Partial control over pulse length/shape	a) If a single transverse mode is required, the unstable resonator optics shown in figure 3.2.1(b) could be used with a low pressure section incorporated into the relay section marked as Y-Y'. (But see note (2.b) below).
2. Large Oscillator with injection locking	Efficient	Fairly complicated. Only line-centre operation has been demonstrated. Partial control over pulse length/shape.	a) To maintain a single longitudinal mode for > 300 ns has been shown to be problematic. (24). b) If injection tuned off-line centre high pressures ∿ 3 atmos. would probably be needed to avoid a frequency chirp toward the maximum of the gain curve. c) An unstable resonator produces an annular beam in the near field. This is undesirable for optical pumping. In the far field the central hole will fill in and will comprise a central lobe surrounded by concentric rings. Depending on the magnification of the optics these rings can contain a sizable fraction of the total energy.
3. Oscillator/ Amplifier	Tunable > ∓ 1.5 GHz from line-centre. Pulse length adjustable as required. Rectangular pulse shapes possible.	Inefficient. Fairly complicated.	a) Oscillator section would make an ideal injection source for 2 above.

3.2.1 The Oscillator

A suitable oscillator has been developed at the CRPP and is shown schematically in figure 3.2.2.

The Laser

The TEA CO_2-laser has an active length of 50cm and a cross-section that measures 5 x 5 cm. The design of a similar device is given in (25) together with a parametric study of its performance. The salt windows of the laser are set at Brewster's angle. As a result of these intra-cavity polarizing elements the fractional power in the plane-polarized component exceeds 96%. At atmospheric pressure the available tuning range about line-centre is approximately $\mp$ 1.5 GHz.

The Resonator

Transverse Mode Control:

The pump pulse intensity should be spatially uniform as there is no re-distribution of the energy within the FIR laser. Consequently, the oscillator should operate on a single transverse mode, or on many modes. Low-order intermediate cases result in a non-uniform intensity distribution. It would be advantageous too to have a cavity configuration that is insensitive to misalignment so that the pump pulse is as reproducible as is possible. This constraint precludes the use of a plane-plane resonator. Furthermore, we wish to minimize cavity losses since axial mode selection techniques (see later) can be lossy; thus unstable resonator optics are unsuitable. Concentric and hemispherical cavities each dictate an intracavity focus, this is undesirable because of the high power densities which result leading to possible damage to cavity optics. There remain the confocal geometries. Whilst curved diffraction gratings can be manufactured, a simple and cheaper solution is to adopt a half-symmetric confocal system. In this

arrangement one mirror (the grating) is plane and the other curved. The cavity is equivalent to half of a symmetric system that is twice as long.

The output coupler is made from ZnSe and cut as a meniscus having equal radii of curvature for each face. This prevents the element behaving as a diverging lens. The concave surface has a reflectivity of 25% at 9.6 μm whilst the convex surface is anti-reflection coated for the wavelength region 9 - 11 μm. An aluminium master grating (150 grooves/mm, blazed at 8 μm) completes the arrangment.

For a laser cavity consisting of curved mirrors, each transverse mode oscillates at a different frequency (26). Since we want to restrict the FIR-laser line-width, the CO_2 pump line-width should be as narrow as is possible. Consequently, a single transverse mode is to be preferred to many modes. To ensure operation on the lowest order transverse mode we take advantage of the higher losses suffered by higher order modes when an aperture is introduced into the laser cavity.

For the arrangement described here, an aperture of 4.1mm diameter placed in front of the grating will reliably provide the necessary discrimination.

Longitudinal Mode Control:

Before we consider the techniques of longitudinal mode-selection, we turn our attention again to Figure 3.1.4. The conversion efficiency ε_{FIR}^{385}, between pump and FIR radiation rises as the pump frequency moves away from line-centre. For a CO_2 laser operated at atmospheric pressure the gain falls rapidly with off-tuning and, consequently, the energy available for pumping. It is apparent from the figure that for a pump system comprising TEA lasers it is disadvantageous to tune from line-centre.

For a CO_2-laser amplifier that operates at, say, 3 atmospheres absolute, the individual gain curves broaden considerably, for example, at a frequency of 1.5 GHz away from line-centre the gain has fallen by only 5%. Con-

sequently, the energy available for pumping is about the same as that at line-centre with the advantage of a much higher CO_2/FIR conversion efficiency ($\sim$ 1.6x). The amplifier we propose for use with JET (section 3.2.3) is designed for operation at this elevated pressure.

Two alternative techniques for longitudinal mode control are described, the first tunable but capricious, the other fixed at line-centre, but simple and stable.

(a) Using a Fabry-Perot Etalon

Figure 3.2.3 shows schematically the variation of conversion efficiency of the pump to FIR energy as a function of pump frequency tuning about line-centre, discussed in the previous section. Below this, figure b, is the gain curve for an individual CO_2-laser line. The horizontal dashed line represents the threshold level at which the gain exceeds intrinsic cavity losses. Thus lasing can occur within the frequency range marked as A - A'. The row of vertical bars, figure c, indicates the laser-cavity resonances where oscillation can be sustained. For a cavity of length L these will occur with a spacing, $\Delta\nu = \frac{2L}{c}$.

The frequency spectrum of the multimode oscillation that results can be seen in figure d. An individual mode, that lying closest to the maximum of the CO_2/FIR conversion efficiency, may be selected by a suitable narrow-band pass filter (e.g. a Fabry-Perot etalon) situated within the laser cavity. The transmission function of an etalon is shown in figure e.

Tuning of the transmission maximum is accomplished by changing the plate separation of the device. In fact, generally it is sufficient only to favour the chosen mode rather than to suppress the others. Thus, whilst several modes might lie within the high-transmission envelope, provided there is a discrimination in gain of $\gtrsim$ 5% the most favoured mode will develop and grow at the expense of all others.

The free-spectral-range (FSR) of the etalon is chosen so that only one transmission maximum lies within the limits (A - A') of lasing.

At the CRPP we use an air-spaced etalon having ZnSe plates separated by 40 mm (FSR = 3.75 GHz) coated to have a reflectivity of 60% in the wavelength range 9 - 10 μm and polished flat to $\frac{\lambda}{100}$. Tuning (translation of the plates) is accomplished by means of 3 piezo-electric transducers that linearly vary the separation of the plates within a 8 μm range.

(b) Using a Low Pressure Section

An alternative and a much more simple and stable technique for producing a single mode, but one that is not tunable from line centre (22) involves incorporating a low pressure (narrow gain width) continuous gain section in the same laser cavity as the atmospheric pressure discharge (figure 3.2.1(a)). Thus we can ensure the presence in the resonator of a significant level of radiation in a single longitudinal mode at the time when the high gain, high pressure section is pulsed. In this case, one mode has a considerable head start in the pulse growth (other modes grow from spontaneous emission levels of the order of 10^{-14}W) and can deplete the available gain well before other modes have built up appreciably. Thus a high power, single-longitudinal-mode pulse can be obtained, superimposed on the low power c.w. output. A further refinement is to use a quasi-c.w. ($\sim$ 100 μsec. duration) discharge as a much higher gain can be realized with a consequent enhancement of the efficacy of the technique.

The construction and operation of both the power source and laser is extremely simple. The c.w. laser head comprises two annular electrodes (the central hole is 25mm in diameter) mounted within and at each end of a 80 cm long, 50 mm diameter quartz cell; a third, pin-type electrode is situated mid-way along the cell. The salt end-windows are mounted at Brewster's angle and simply glued in place. The total working pressure of the laser gas (comprising CO_2, N_2 and He in the ratio of 1 : 1 : 8 respectively) is about 12 torr. Connected between each annular electrode and the centre pin is a 0.5 μF ca-

pacitor - via a thyratron switch. To excite the gas each capacitor is first charged to 10 KV then the circuit made complete by the switch, thereby generating a glow discharge in the gas.

Apart from determining the longitudinal mode of the TEA CO_2-oscillator, the low pressure section can modify the temporal profile too. In general, the pulse profile tends to flatten, the extent to which this will occur depends upon the gas mix ratio, gain (of each section) cavity Q, etc. A flat-topped pulse is well suited to the needs of the experiment, (notwithstanding this, the resulting pulse-shape may not be sufficiently flat-topped for our needs and consequently an alternative technique for temporal pulse-shape control is described in sub-section 3.2.2). Which of these two techniques is more suitable for use on JET is not immediately obvious. However, the decision between them can be left until sufficient working experience with each has been gained; such tests using both schemes are underway at the CRPP.

Auxiliary Components:

For either technique of longitudinal mode control, cavity alignment and overall length should be maintained to be as stable as is possible, ideally to within fractions of a CO_2-wavelength - see figure 3.2.2.

To provide the necessary stability we have adopted a massive (400 kg) aluminium honey-combed table on which to mount the resonator optics. The working surface of the table is a skin of super invar (thermal expansion coefficient = $0.36 \times 10^{-6}/C^{o}$). The optics are mounted on this, and the grating on a steel plate. This plate is mounted in such a way as to expand in the opposite direction to the invar. When the ratio of the lengths of the steel and invar is in the inverse ratio of the expansion coefficients, then the overall cavity length remains constant (27) independent of (small) temperature changes. The table top is enclosed and a positive pressure dust-filtered temperature-controlled air supply incorporated. Isolation from floor-borne vibrations is achieved by pneumatic supports. Two He-Ne lasers are used as aids during the alignment of the set-up; also shown

are various beam monitors and a low-pressure gas cell. This cell is used in conjunction with the F.P. etalon. By diverting the oscillator beam through the cell and monitoring the transmission as a function of piezo-electric voltage a convenient calibration of voltage/off-tuning can be made, see for example figure 3.1.4(b).

To prevent coupling between the oscillator optics and the amplifier for wavelengths other than the pump line an absorbing gas cell is placed in the beam path. The properties of this isolating element are described later.

The optics of the low power section of the system are protected against amplified reflections from the components in the FIR laser by a confocal beam expander of unit magnification. The focal length is chosen to be 50 mm in order to be able to adjust the focused power density below breakdown conditions for a beam leaving the oscillator section and to be above threshold for the reflected beam.

3.2.2 Pulse Shaping

The effect of the FIR pulse-shape on the S/N ratio in the scattering experiment is discussed in section 4.3.3. It is shown that a flat-topped FIR pulse would be an advantage. Now because the FIR transition of interest is a Raman process then the FIR pulse shape will closely follow the pump in time.

The most general form of a CO_2-laser oscillator pulse is sketched in figure 3.2.4. It comprises an initial spike of about 50 ns duration followed by a tail lasting some microseconds. Some degree of control over the pulse shape is possible, by varying the cavity Q and the relative proportions of the laser gas mix (CO_2:N_2:He). For example, one may choose to have a spike alone, or a small spike together with a long, flat-topped tail. In the case of an oscillator/amplifier system, the interval between firing the stages can be varied, that is to amplify the spike alone or progressively more and more of the tail. This is illustrated by figure 3.2.5. The resulting pulse shape is however approximately triangular. As pre-

viously mentioned an intra-cavity low-pressure section can significantly modify the temporal pulse shape, generally by lowering the peak power and flattening the pulse, and this technique alone may be adequate for our needs. If, however, further shaping is necessary there remains an alternative approach to consider. This is to choose a gas mix that gives a long, flat-topped tail and to chop out the required pulse length using an electro-optic shutter. The active element of the shutter can be an anti-reflection coated CdTe rod. The transverse Pockels effect can be employed to electronically change the polarization of the transmitted beam. If the incoming beam is vertically polarized, application of the halfwave voltage to the CdTe crystal rotates the polarization 90^{o}, to the horizontal, and a following high extinction ratio polarizing element, oriented to pass the horizontal will transmit the beam. This continues until the halfwave voltage is removed and the transmitted power returns to its null value.

The rise-time, duration, and fall-time of the optical switching are determined by those of the electrical waveform passing through the switching head. The electric pulse should be between 6 to 11 kV lasting between 0.2 and 1.5 μs (adjustable) and have a rise/fall-time of about 30 ns. A suitable wave form can be generated with a circuit that utilises a Krytron switch (28). For a crystal measuring 10 x 10 x 50 mm the half-wave voltage is 10.5 kV. This results in a contrast ratio* of 500 : 1. Calculations predict that with this contrast a 2-3 Joule prepulse will be generated. However, this is negligible compared to the 500 Joules of the main pulse.

---

* (Ratio of the intensity, I_o, of the radiation incident on the second polarizer to the transmitted intensity, I, when no field is applied.)

3.2.3 The Final Amplifier

Four CO_2-laser amplifiers were considered for this optical pump system. Details of the decision to purchase a Systems, Science and Software Model 1353 E-Beam-Controlled Device can be found elsewhere (29). This laser has an active volume of 200 x 16 x 16 cm and operates at a pressure of 3 atmospheres absolute. An important advantage of operating at an elevated pressure is that the gain width of the individual laser lines becomes pressure broadened. This results in a much increased energy extraction efficiency for a signal whose frequency is displaced from the line-centre. It will also reduce the frequency chirp towards line-centre that occurs (30) when such a signal is amplified.

The Model 1353 utilizes a double-sided cold cathode electron gun. Only one side is used in the present arrangement so that the system can be expanded in the future. This possibility is discussed in the section dealing with the feasibility of making multi-pulse measurements. The laser operates on Helium-free gas mixtures, a feature that significantly reduces operating costs. Some specifications of this device are listed in table 3.2.2.

In an E-beam controlled CO_2-laser amplifier the temporal gain profile may be easily altered so that pulses of duration 100 ns to several μs can be amplified with similar extraction efficiences. The main disadvantage of using such a laser is that the titanium foil used in the electron gun is fragile and periodically ruptures, necessitating replacement. However, in the case of the triode guns currently used by S^3, the foil lifetime is in excess of many thousands of shots. This does not present a serious problem. The other disadvantage to E-beam lasers - the production of X-rays - may be overcome by judicious use of lead screening.

Table 3.2.3 shows some calculated values of the E-beam amplifier output for various input energies, wavelength and optical arrangements. These values have been obtained using the Franz-Nodvick equation (31) which describes laser amplification in a simple 2-level system. It seems clear from the table that for those wavelengths of interest if the 100 mJ

oscillator output is passed twice through the amplifier, substantially more energy than the minimum required should be extracted, although certain observations should be borne in mind with respect to these estimates:

a. Damage limit of optical components

The salt windows of the amplifier set a limit to the energy density that can be extracted from the laser. Values of the damage threshold vary with pulse length and beam uniformity. Presuming no hot-spots and a 1 μs pulse length, the best estimates of safe working energy densities give a value of about 3 Joules/cm^2 (32,33). Thus the values tabulated below are the limits to the extractable energy under normal working conditions.

Beam Dia. (cm)	5	10	12	15
Upper limit of extractable energy (Joules)	60	240	345	540

Clearly we need a pump beam diameter as large as is possible.

b. Limit to Pump Beam Diameter

The pump beam diameter may be restricted by a variety of considerations: an upper limit to the length of the FIR resonator is set by the need to obtain a single longitudinal mode. However, the ratio of diameter to length cannot be decreased indefinitely. The largest diameter reported for single mode operation at 385 μm is 10 cm (18). Optical components of sufficient size eg. mesh, z-cut quartz etc. can be difficult to obtain particularly as some items are placed at 45^{o} to beam.

It remains to be seen whether the full 15cm diameter can be utilised.

c. Accuracy of the Calculation

The energies listed in the table have been calculated assuming conservative values for the constants α_0, and E_s. It is probable that they underestimate the energy available for extraction.

The arrangement of the oscillator and amplifier that we propose is shown in figure 3.2.6.

A 100 mJ, $\sim$ 1 μs long pulse leaves the oscillator having a beam diameter of about 6 mm. It is directed by beam steering optics through an isolation gas-cell (details of this gas cell are given in the next sub-section).

The beam has a natural divergence and the optical path between the two lasers is arranged so that the diameter is 30 mm on arrival at the amplifier. The beam enters the laser through a special port of 50 mm diameter and passes diagonally through the active region then leaves by the main salt window. (Although this port is shown in figure 3.2.6 to lie in a horizontal plane in fact its orientation is in a vertical plane to the optic axis so as to avoid mechanical supports within the pressure vessel.) Upon leaving the chamber, the beam once again traverses an isolating gas-cell and is allowed to expand to the required size of between 12 and 15 cm diameter, then it is redirected through the amplifier, along the optic axis, thence toward the FIR oscillator.

3.2.4 Isolation Between Amplifying Stages Using Absorbing Gases

Amplifiers cannot be coupled together in series indefinitely: after a certain gain-length product they become unstable to parasitic modes or superradiance.

From the experiences of several groups working with large CO_2-laser chains (34, 35), on any emission line the general condition necessary to avoid self oscillation and parasitic feedback is that the sum of the gain-length products $\Sigma g_o L < N$, where N is a number between 10 and 15, depending on the optical arrangement involved.

We have described (36) a general method for selecting and optimising a gas mixture which serves to isolate successive stages of the large CO_2-laser chain of amplifiers at the CRPP. Unlike previous work using gas cells as isolators (34, 37) the technique achieves high values of small-signal transmission at the operating wavelength whilst suppressing unwanted, higher-gain lines.

Saturation of absorption to produce bleaching is not a prerequisite to efficient energy extraction.

For the 10P(20) line the single pass value of $\Sigma g_o L = 8$ i.e. the laser amplifier is stable, for a double pass, however, it is not. The 9R(22) line has a $\Sigma g_o L$ of 5.2. Thus even for a double pass the amplifier may be stable on this line. Figure 3.2.7 shows an IR spectrum of 2 gases, viz. SF_6, C_4F_8-cyclic, mixed in a ratio 1 : 1. The total pressure was 200 torr. The small-signal transmission at, and near to, 10P(20) is very low, i.e. the laser would be stable using this mix as isolator. The peak gain lines of the 9P branch too are reduced by between 15 - 22% whilst at the 9R(22) line an absorption of 10% is measured. If we allow for reflection losses due to the windows of the gas cell ($\sim$ 14% on average) the overall $\Sigma g_o L$ for a double pass through the amplifier for the 9R(22) line becomes 7.8. Whilst, no doubt, some fine-tuning of this mix will be necessary, adequate isolation should be achievable with

this technique.

3.2.5 Concerning the Feasibility of Multi-Pulse Ion Temperature Measurements

It would be of interest to be able to follow the time history of the ion temperature of the JET plasma, particularly during heating experiments. In this sub-section we explore the feasibility of repeating the measurement several times, within the lifetime of a JET discharge.

The FIR laser itself, the receiver and the associated signal processing equipment need practially no modification. However, the demands on the CO_2 pump-laser would be as follows :

Number of pulses	:	$2 \sim 10$
Minimum interval between pulses (set by energy confinement time in plasma)	:	0.1 s
Burst duration	:	10 - 20 s
Burst repetition rate	:	20 mins.

To modify the CO_2-oscillator for operation in bursts at 10 Hz presents no major difficulty or expense.

The problem reduces to that of obtaining multiple pulses from the E-beam amplifier. The difficulties involved have been examined on our behalf, by the manufactures of the device,Systems, Science and Software (who have had previous experience supplying similar devices). Their engineers report that for two pulses only, the double-sided gun, supplied as a standard feature with this model, can be used. All that is required is to replace the present gun power-supply with the double-sided version, and to modify the trigger system.

Three factors which limit the repetition rate are acoustic disturbance created by previous pulses, impurity build-up and temperature rise of the gas. However, provided that small (cheap) blowers are mounted within the discharge chamber, of volume 1650 lt, to circulate the laser gas, 10 Hz bursts of about 10 shots seem feasible. Finally, the existing discharge power supply would need to be replaced by a more powerful one that has been carefully matched to the laser pulse-length.

In summary, multiple pulsing of the system, using the existing gun and discharge chambers, requires as a minimum the installation of a second discharge chamber and power supply, and a new gun power supply. To obtain more than two pulses, new discharge supplies are also needed. All of the technology required to design and build the additional equipment is available.

3.3 The C.W. FIR Local Oscillator

The function of the local oscillator (L.O.) is to provide a c.w. FIR signal of a frequency slightly different from that of the pulsed, scattered signal (for this case by some GHz).

Despite there being many thousand optically-pumped laser transitions it is a matter of chance whether a suitable one (i.e. of sufficient power and appropriate frequency off-set) exists for an arbitrary scattered wavelength. That no tunable c.w. source of FIR radiation is readily available is a serious handicap in the search for alternative wavelengths more appropriate to the JET conditions. It is unfortunate too, that a transition may only work pulsed but not c.w. because the transition is inaccessible to the very narrow tuning range of a c.w. CO_2 laser and/or is below the threshold for stimulated Raman scattering.

For the system we have proposed for JET (385 μm - 779.5 GHz - with a Schottky barrier diode mixer) the optically-pumped 381 μm (787.7 GHz) transition of deuterated formic acid, DCOOD, can be used. Whilst the frequency off-set (i.f. centre-frequency) of 8.25 GHz is somewhat greater than ideal it is, nevertheless, acceptable. In fact, we may be able to reduce this i.f. centre-frequency somewhat. We have previously discussed the advantage to be gained by pumping the pulsed FIR-laser with a beam whose frequency is shifted by + or - 1 GHz from the CO_2 line-centre. The resulting FIR frequency will be shifted by the same amount. Thus by choosing the positive sign we should be able to diminish the i.f. centre frequeny to about 7 GHz.

The most commonly employed laser resonators are schematically illustrated in Fig. 3.3.1. The input coupling hole for admitting the infrared pump radiation is a common feature and may also be used with a splitter arrangement to outcouple the FIR as illustrated for the parallel-plate waveguide structure in Fig. 3.3.1(d). Each of these geometries has certain advantages relative to the others; however, the hollow circular waveguide is the most widely used because of its smaller size, better transverse mode control, and beneficial effects of de-exciting collisions with the walls. In addition, the smaller transverse dimensions of the waveguide resonators, typically 1 - 4 cm, permit the use of hybrid output coupling techniques. The larger diameters required by Fabry-Perot resonators make fabrication of hybrid couplers too expensive and difficult, but excellent performance in terms of power has been reported using Fabry-Perot resonators with hole coupling.

It is difficult to compare data available in the literature and then select an optimum laser geometry for a particular system. Different molecules and different transitions from the same molecule have exhibited optimum performance from a variety of waveguide and Fabry-Perot cavities. However, as a general rule the best transverse mode quality and highest ouput powers have been achieved in hollow dielectric waveguides using some form of hybrid output coupler (8).

Whilst complete CO_2 and FIR systems are commercially available, custom built for a given gas transition, the optimisation of the FIR

cavity is neither a particular difficult nor time-consuming task and could be undertaken in parallel with that of the pulsed FIR-laser. For this transition a conversion efficiency (power CO_2/power FIR) of 0.009% has been reported from a non-optimised arrangement. Disregarding any possible improvements in this ratio accrued during development a c.w. CO_2 laser pump of about 300 W powerwould seem to be required to produce the tens of milliwatts of FIR needed. Fortunately the L.O. need only be c.w. with respect to the pulsed signal i.e. quasi-c.w. operation should suffice. (By quasi-c.w. we mean that the L.O. pulse length should exceed that of the scattered signal by $\sim$ 100 x, i.e. it should last $\sim$ 150 μs.)

For a pulse length of this order, a c.w. CO_2 laser can deliver between 5 and 10 x its rated true c.w. power following minor modifications to the power supply. Thus a laser of about only 60 W power at 10.6 μm (the gain for the pump line, 10R(21) {10.31 μm}, is $\sim$ 80% of that for 10P(20)) will be required.

3.4 Summary and Concluding Remarks

The generation of a FIR pulse suitable for an ion temperature measurement by Thomson scattering from the JET plasma has been considered. The principles of optically-pumped FIR-lasers are sufficiently well-understood that the construction of a suitable device can be undertaken with a reasonable degree of confidence.

To this end, the following proposals have been made:

a) To optically excite the 385 μm emitting line of D_2O vapour using a CO_2-laser beam.

b) A folded unstable resonator be used for the FIR oscillator, and to couple the pump beam into the vapour via a wire grid.

c) That the CO_2-pump-laser system comprise an oscillator and an amplifier.

d) To restrict the oscillator to a single longitudinal mode using either an intra-cavity low pressure section or a Fabry-Perot interferometer.

e) That the amplifier be E-beam controlled and operate at 3 atmospheres.

f) The local oscillator too, is optically pumped. The vapour in this case to be deuterated formic acid.

Three related questions were examined, namely :

i) The possible need for some auxiliary pulse shaping of the oscillator pulse, and ways to achieve it.

ii) The prevention of self-oscillation of the amplifier.

iii) The feasibility of obtaining more than one FIR laser pulse within the time-scale of the JET plasma.

Satisfactory techniques to overcome the difficulties involved appear to exist.

TABLE 3.2.2

SPECIFICATIONS - MODEL 1353-2 E-BEAM-CONTROLLED AMPLIFIER

1. Amplifier performance

Aperture	15 cm x 15 cm
Gain length	200 cm
Operating pressure	3 atm absolute
Gas mixture	0:1:4 ($He:N_2:CO_2$)
Small signal gain (centreline)	greater than or equal to 0.04 per cm [10P(20)]
Gain uniformity	plus-minus 7 per cent with respect to average
Energy input to gas	greater than or equal to 200 J/l

2. Electron gun

Electron beam area (each beam)	16 cm x 200 cm
Electron gun voltage	300 kV
Weight	955 kg

3. Laser discharge chamber

Laser gas pressure	3 atm absolute
Active laser gas volume	16 cm x 16 cm x 200 cm
Optical aperture	15 cm x 15 cm
Weight	3'400 kg

4. Electron gun power supply

Type	2 stage Marx generator with triggered spark gap switches
Output voltage	200 to 300 kV (adjustable)
Stored energy	20 kJ at 300 kV
Weight	2'180 kg (inc. oil)

5. Discharge power supply

Type	7 stage Marx generator close-coupled to discharge chamber
Output voltage (matched load)	350 kV
Stored energy (maximum)	35 kJ (for 350 kV into matched load)
Pulse length (FWHM)	2.2 μsecs.
Weight	7'100 kg (inc. oil)

TABLE 3.2.3

E-BEAM AMPLIFIER OUTPUTS CALCULATED* FOR VARIOUS INPUT ENERGIES, WAVELENGTHS, AND OPTICAL ARRANGEMENTS.

FIR Molecule	λ FIR (μm)	CO_2 Pump-line	λ CO_2 (μm)	Estimate of small signal gain	Single Pass Energy (Joules) a) 100 mJ, b) 1 J, c) 5 J } input energy			Double Pass Energy (Joules) Including gas cell. (25% loss) See text.	
					Beam Diameter (cm) 5	10	15	10	15
D_2O	385	9R(22)	9.260	$0.65\ \alpha_o$	a) 12 b) 39 c) 63	16 83 167	17 115 275	a) 186 b) 236 c) 226	339 516 526
D_2O	113	9R(12)	9.317	$0.58\ \alpha_o$	a) 7.9 b) 31 c) 55	9.5 60 137	10 77 213	a) 132 b) 201 c) 202	217 418 461
D_2O	66	9P(32)	9.657	$0.41\ \alpha_o$	a) 2.5 b) 16 c) 36	2.6 22 71	2.6 24 93	a) 29 b) 99 c) 132	34 163 269

* Using the Frantz-Nodvik equation which describes laser amplification in a simple two-level system to give the flux $E_o(x)$ $\{J/cm^2\}$ at any position x, along the path of the beam through the medium, from the input window :

$$E_o(x) = E_i + \alpha_o x E_s + E_s \ell n \left\{ 1 - \exp\left(\frac{-E_i}{E_s}\right). \left[1 - \exp(-\alpha_o x)\right] \right\}$$

where E_i is the input flux $\{J/cm^2\}$,

E_s is the saturation flux $\{J/cm^2\}$ = 0.25 J/cm^2/atmosphere

α_o is the small-signal gain $\{cm^{-1}\}$ = 4% cm^{-1} at 10.6 μm.

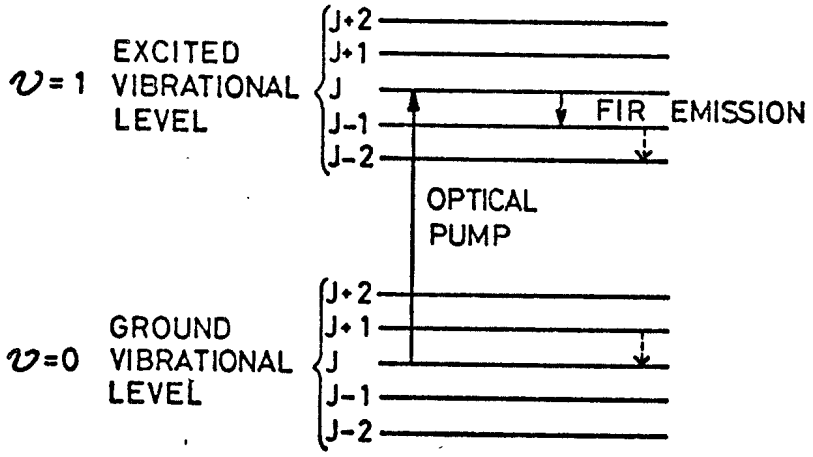

Fig. 3.1.1 Energy-level diagram of an optically-pumped far-infrared laser. The FIR transition occurs between two rotational levels of the upper vibrational state. Also shown are possible cascade and refilling transitions.

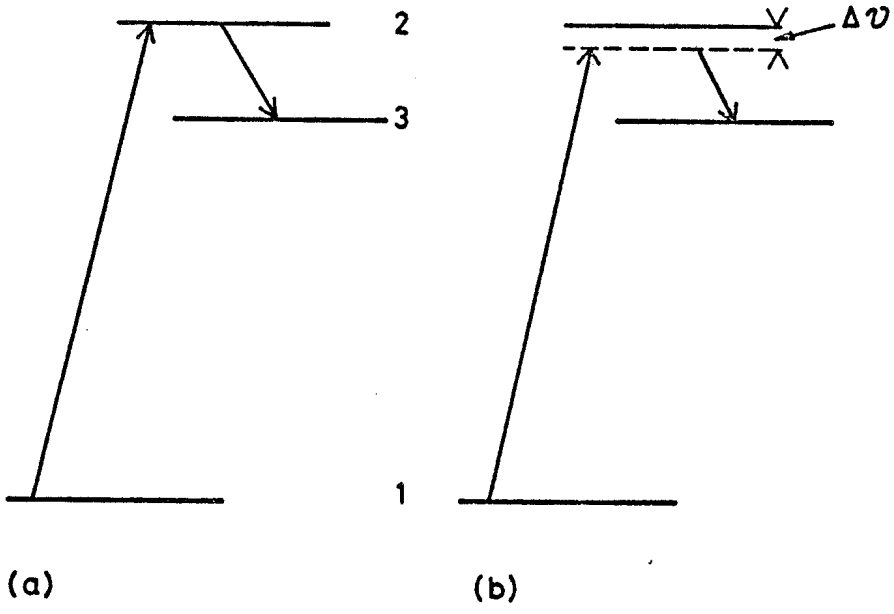

Fig. 3.1.2 Energy-level diagrams illustrating differences between (a) emission by a laser process and (b) emission by a stimulated Raman process. For further details see text.

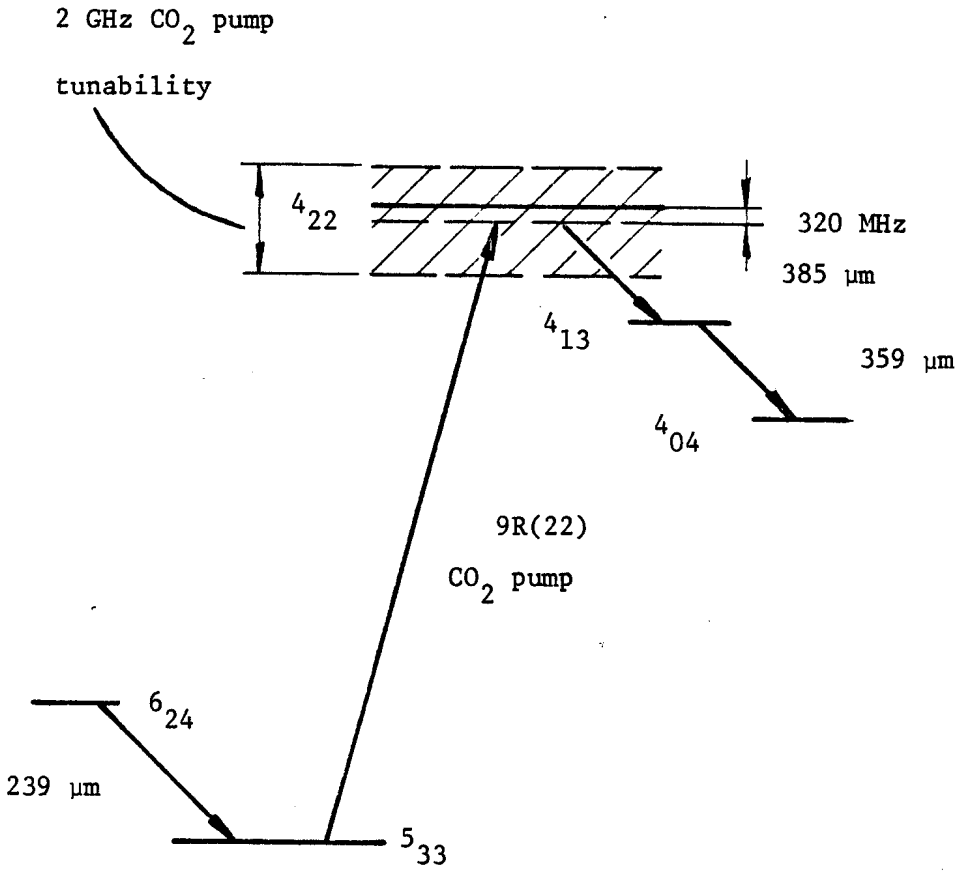

Fig. 3.1.3 Partial energy level diagram of the D_2O molecule. The tunability of the 385 μm transition and of the 9R(22) CO_2 pump transition is illustrated by the shadowed region. The relative spacings of the rotational energy levels and of the tuning range are greatly exaggerated. The 6_{24} and 5_{33} rotational levels are in the 000 vibrational ground state, and the 4_{22}, 4_{13} and 4_{04} are in the 010 first excited vibrational level (17).

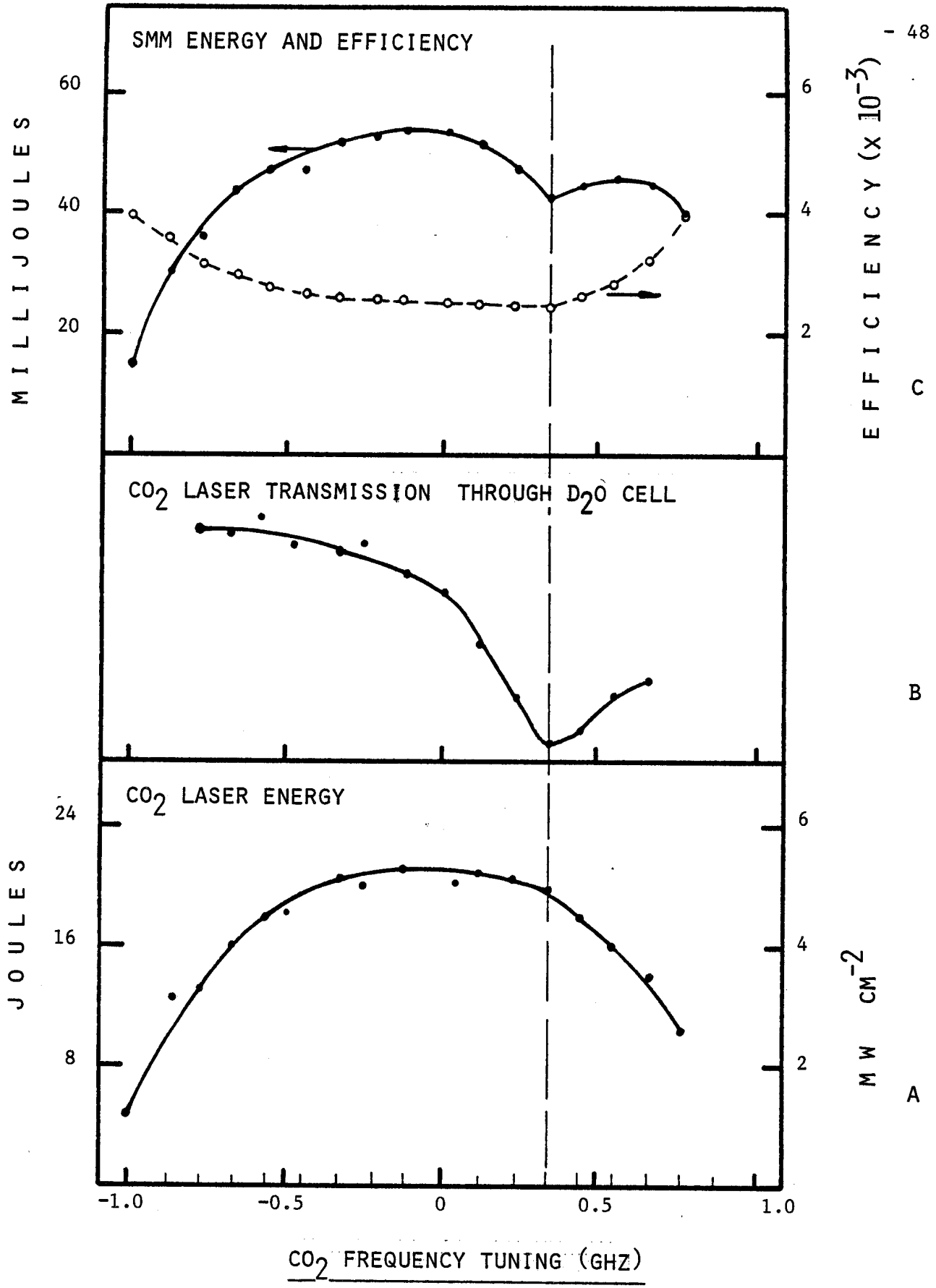

Fig. 3.1.4: (A) CO_2 laser energy and power density as a function of tuning the CO_2 laser frequency around the 9R(22) line centre. (B) Relative transmission of 1% of the CO_2 laser energy plotted in (A) through a 3-m-long cell with 0.5 torr D_2O. A sharp absorption peak occurs $\sim$+320 MHz above CO_2 line centre. (C) Solid circles show total submillimeter energy output of a 3-m-long D_2O oscillator filled to 3.0 torr with D_2O and optically pumped by the CO_2 laser energy plotted in (A). There is a dip at D_2O line centre and maxima when the CO_2 laser is tuned away from D_2O line centre. The open circles show the conversion efficiency of CO_2 laser energy to D_2O laser energy uncorrected for the contributions from the other transitions and losses at windows, mirrors, and beam splitters. These results are taken from Woskoboinikow et al (17).

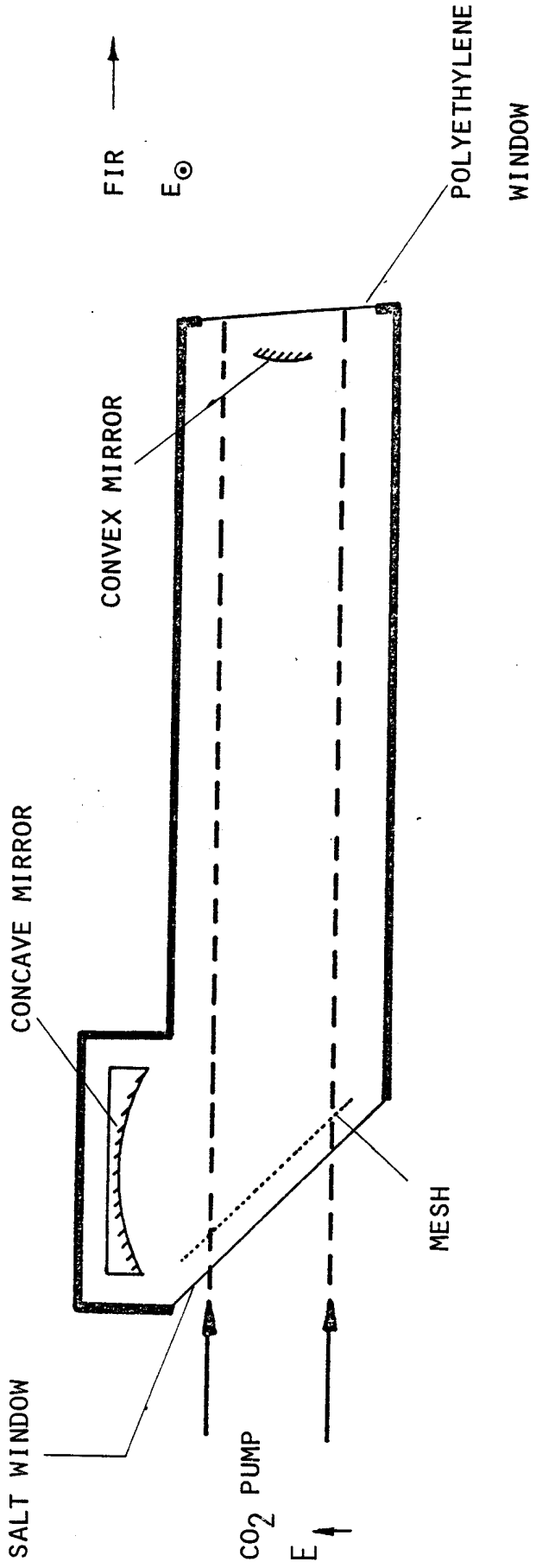

Fig. 3.1.5: THE FOLDED, UNSTABLE FIR RESONATOR

Figure 3.2.1 : Three Configurations for the CO_2-Pump System

a)

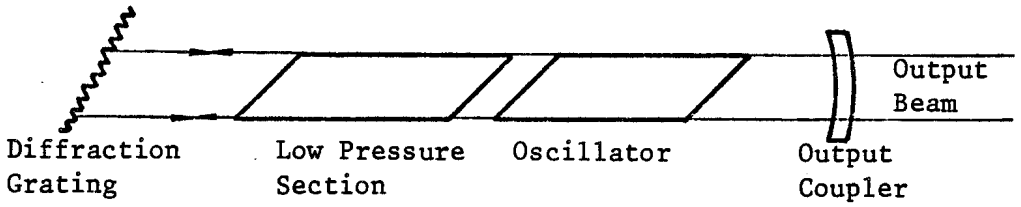

1. LARGE OSCILLATOR WITH LOW PRESSURE SECTION

b)

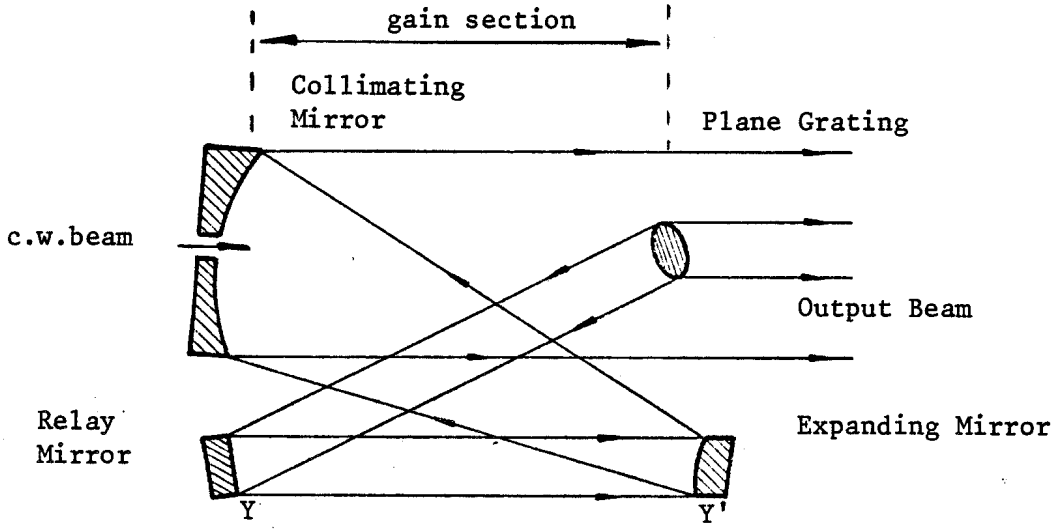

2. LARGE OSCILLATOR WITH INJECTION LOCKING

c)

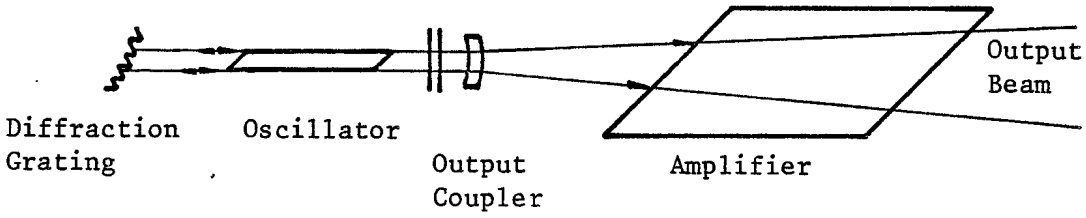

3. OSCILLATOR / AMPLIFIER

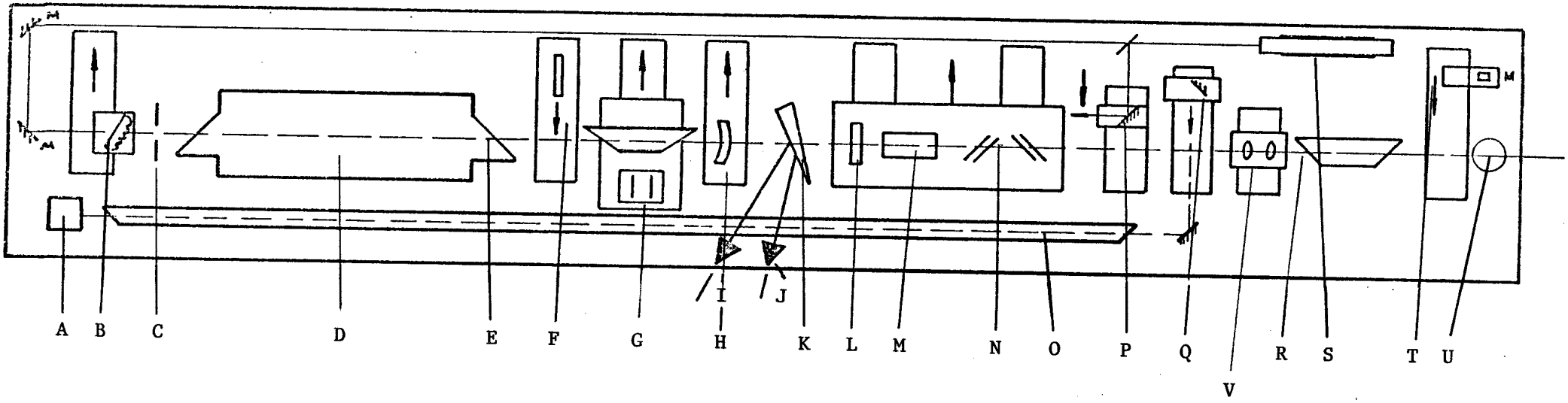

A. Energy monitor
B. Diffraction grating and compensating mount
C. Aperture
D. TEA CO_2-laser
E. Salt window at Brewsters angle
F. Auxiliary output coupler
G. Fabry-Perot etalon or low pressure section
H. Meniscus output coupler
I. Photon drag monitor
J. Energy monitor
K. Salt wedge-beamsplitter
L. Polarizer
M. CdTe electro-optic crystal } Pulse shaping assembly
N. Polarizer
O. Low pressure gas cell
P. Alignment mirror
Q. Mirror
R. Isolation gas cell
S. He-Ne alignment laser
T. Beam steerer for 2nd He-Ne laser
U. Access hole for 2nd He-Ne laser
V. X 1 Beam expander

(Not shown: Temperature-stabilized, dust-filtered enclosure)

Figure 3.2.2 : The CO_2-Laser Oscillator

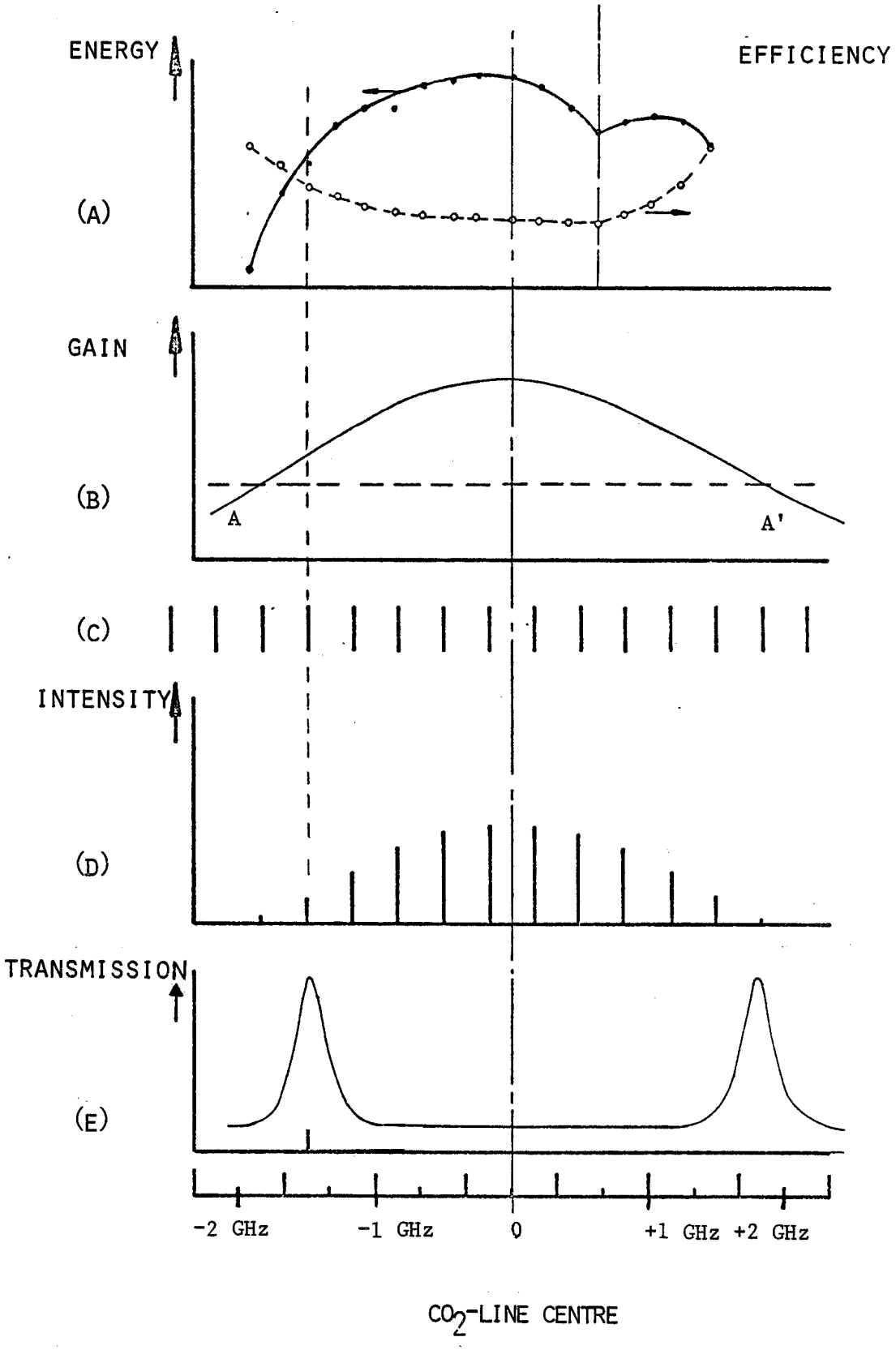

Figure 3.2.3 : Off-Tuning from CO_2 line-centre using a Fabry-Perot Etalon

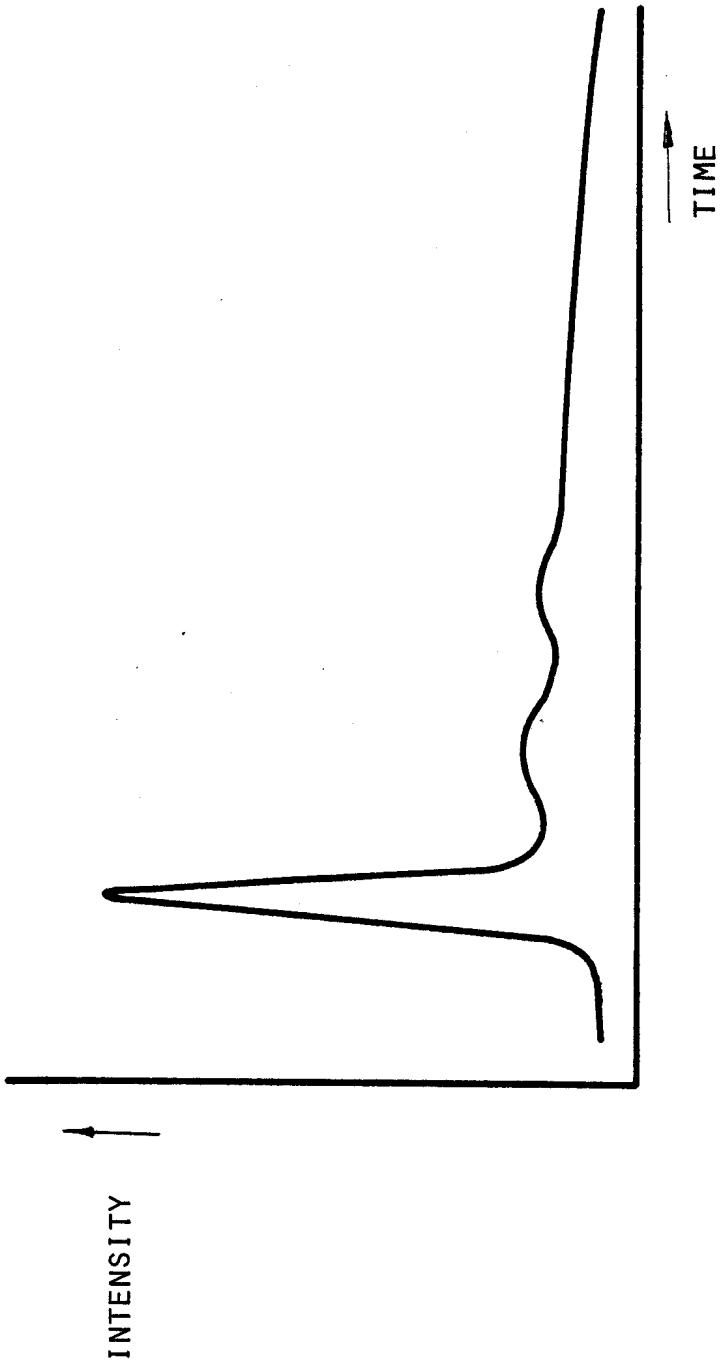

Figure 3.2.4 : A Sketch of the Most General Form of a Gain-Switched CO_2-Laser Pulse

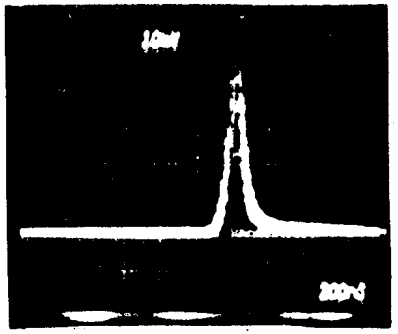

ΔT = 0 μsec

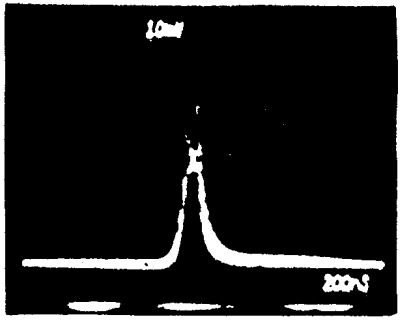

ΔT = 0.4 μsec

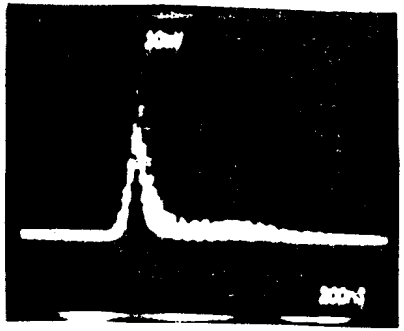

ΔT = 0.8 μsec

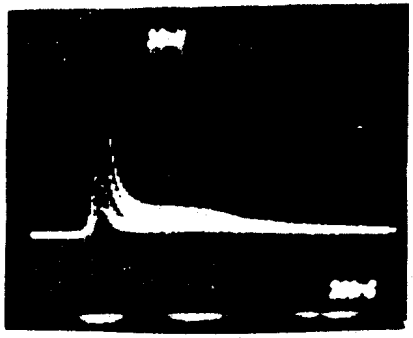

ΔT = 1.2 μsec

ΔT = 1.6 μsec

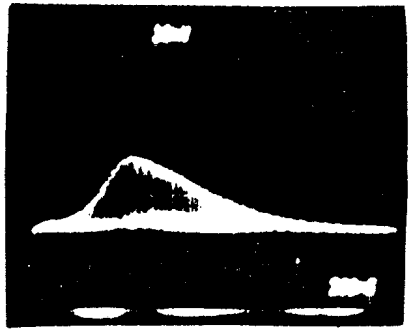

ΔT = 2.0 μsec

Figure 3.2.5 : Temporal output of CO_2-Laser system as a function of delay between oscillator and amplifiers

Vertical scale : 10 mV/Div.

Horizontal scale: 200 ns/Div.

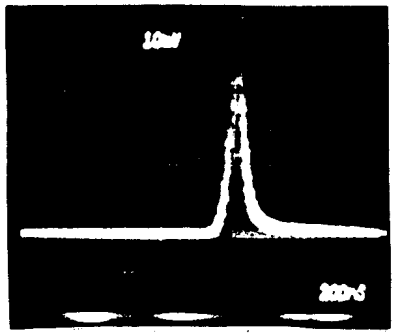

ΔT = 0 μsec

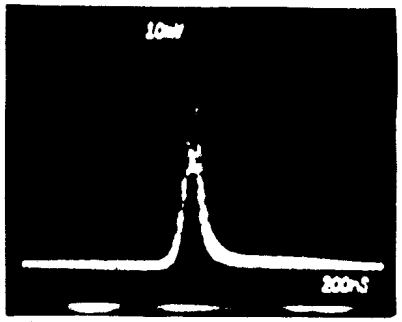

ΔT = 0.4 μsec

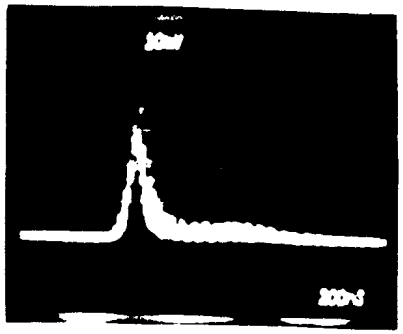

ΔT = 0.8 μsec

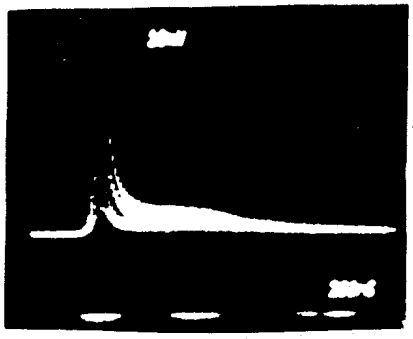

ΔT = 1.2 μsec

ΔT = 1.6 μsec

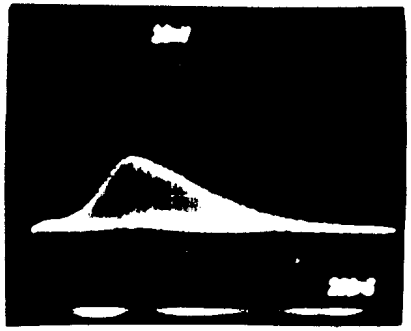

ΔT = 2.0 μsec

Figure 3.2.5 : Temporal output of CO_2-Laser system as a function of delay between oscillator and amplifiers

Vertical scale : 10 mV/Div.

Horizontal scale: 200 ns/Div.

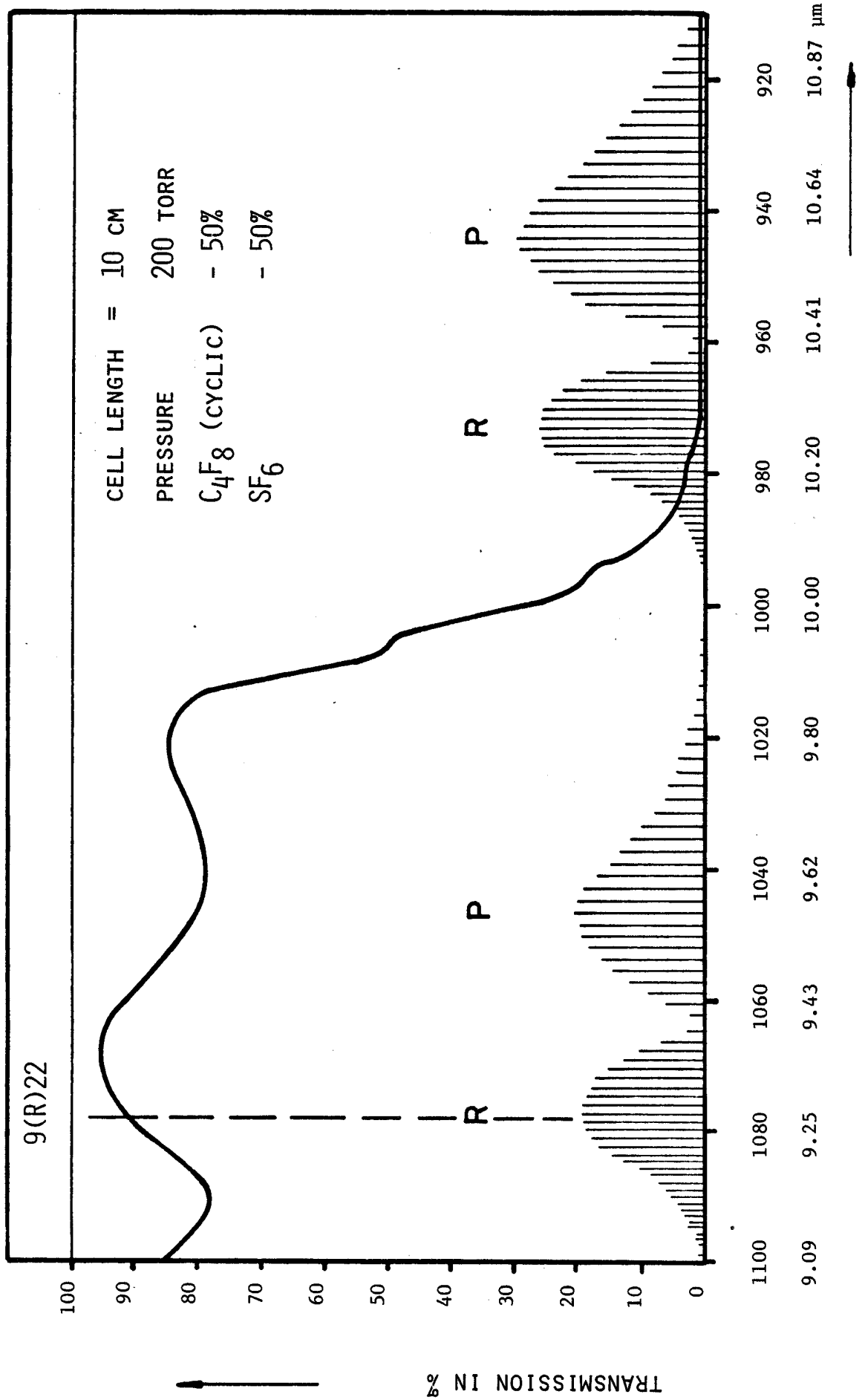

Figure 3.2.7 : IR Spectrum of the Isolation Gas Mixture

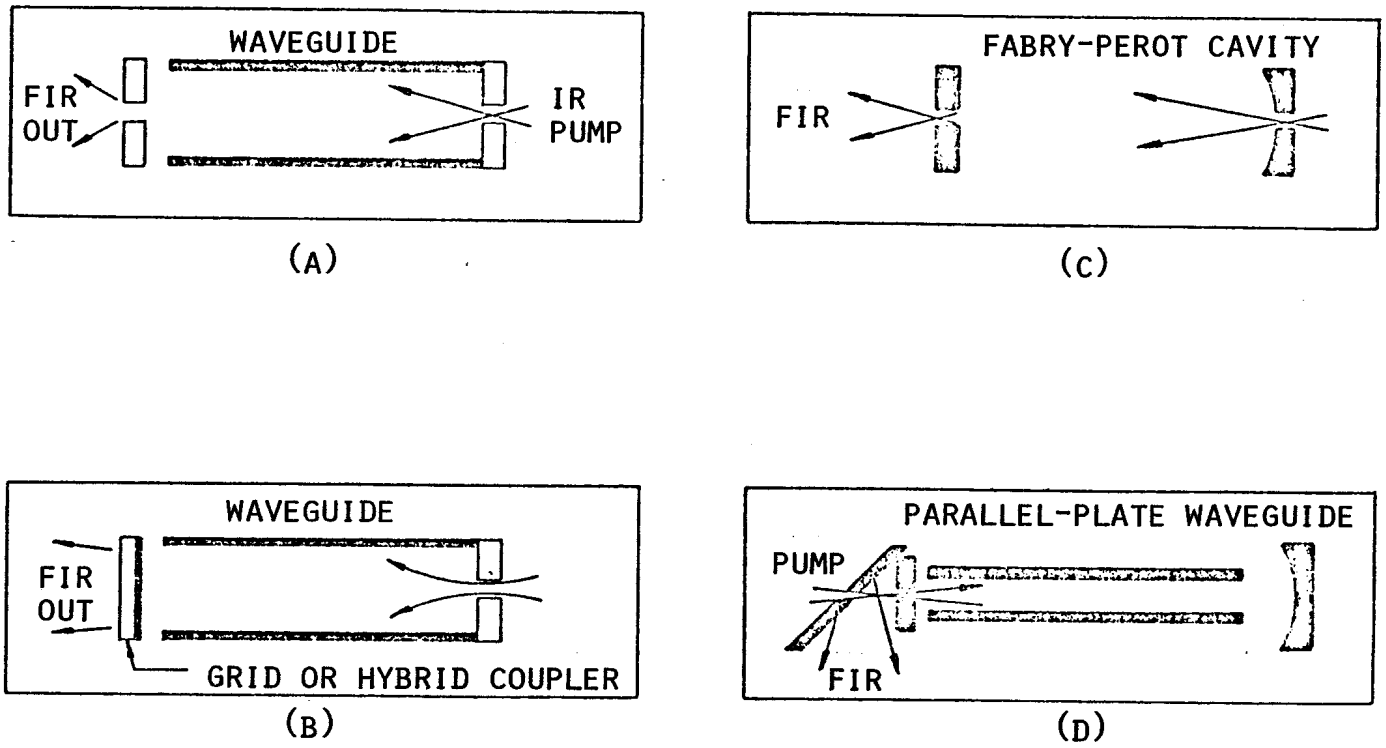

Figure 3.3.1 : Four resonators commonly employed for c.w. operation. The hollow circular waveguide structures illustrated in (a) and (b) are widely used because of their relative compactness, favourable dimensions for wall de-excitation collisions, and allowable variety of output coupling techniques. For metal waveguides, transverse dimensions are typically a few wavelengths whereas hollow dielectric guides must have diameters greater than 100 wavelengths for low propagation loss. The latter geometry provides best mode quality as discussed in text.
(c) illustrates conventional Fabry-Perot resonators. Transverse dimensions are 10 - 15 mm.
The parallel plate waveguide (d), suitable for Stark tuning, is a very compact structure. Plate separation is only a few wavelengths, and the small mode volume restricts available output power.

4. DETECTION AND SIGNAL PROCESSING

This section is concerned with the detection and analysis of the spectrum of scattered radiation. The principles of heterodyne detection are reviewed and the various types of detector that can be used are discussed. Two schemes for obtaining the power spectrum from the detected signal are considered and the accuracy with which plasma ion temperature can be determined is estimated. Finally, a complete system for use on JET is proposed.

4.1 Heterodyne Detection of Submillimetre Radiation

To record the spectrum of the scattered radiation heterodyne detection is necessary, not only to achieve the required sensitivity but, also, to shift the spectrum into a frequency region where technology exists to analyse it.

We assume that a monochromatic local oscillator field $E_{LO} = A_{LO} \exp(i\omega_0 t + \phi_0)$ is superimposed onto a signal field $E_S = A_S \exp(i\omega_S t + \phi_S)$ in the diplexer of a receiver system. The detector responds with a current which is proportional to the total incident power

$$i(t) = \sigma P(t), \tag{4.1.1}$$

where σ is the conversion efficiency of the detector. The incident power can be expressed, in terms of the radiation field, by

$$P(t) = \eta E(t) \cdot E^*(t), \tag{4.1.2}$$

where η takes into account coupling losses and impedance mismatch.

The resultant detector current is

$$i(t) = \sigma\eta(E_{LO} + E_S)\ (E_{LO} + E_S)^*. \qquad (4.1.3)$$

Making the assumption that $A_{LO} >> A_S$, which should always be the case for a heterodyne system, we may drop terms of the order A_S^2 and find for the detector current

$$i(t) = \sigma\eta(A_{LO}^2 + 2\ A_{LO}\ A_S\ \cos(\Delta\omega t + \Delta\phi)), \qquad (4.1.4)$$

where
$$\Delta\omega = \omega_S - \omega_{LO} \qquad (4.1.5)$$

and
$$\Delta\phi = \phi_S - \phi_{LO}.$$

The information-carrying part of the photocurrent, denoted by i_{IF}, is that part of i(t) which oscillates at the IF beat frequency $\Delta\omega$

$$i_{IF}(t) = 2\ \sigma\eta\ A_0\ A_S\ \cos\ (\Delta\omega t + \Delta\phi). \qquad (4.1.6)$$

The signal power at the output of the detector is the mean-squared IF current, viz.

$$S = \overline{i_{IF}^2} = \tfrac{1}{2}\ (2\ \sigma\eta\ A_{LO}\ A_S)^2, \qquad (4.1.7)$$

where the factor of $\frac{1}{2}$ results from averaging the square of the cosine.

The mean-squared noise current (shot noise) for detection limited by the signal noise is (38)

$$\overline{i_N^2} = 2e\overline{i(t)} \cdot B \qquad (4.1.8)$$

where e is the electronic charge and B the bandwidth of the detector or the filter following the detector. Since the average current $\overline{i(t)}$ is essentially the current resulting from the LO term (see 4.1.4)

$$\overline{i(t)} = \sigma\eta A_{LO}^2 , \tag{4.1.9}$$

the noise power is obtained as

$$N = \overline{i_N^2} = 2e\sigma\eta A_{LO}^2 B. \tag{4.1.10}$$

From (4.1.7) and (4.1.10) the signal-to-noise ratio is now obtained as

$$S/N = \sigma\eta A_S^2 / eB = \sigma\eta P_S/eB, \tag{4.1.11}$$

where P_S is the signal power. Introducing a noise equivalent power (NEP) as the signal power per unit bandwidth necessary to achieve a signal-to-noise ratio of one, the above equation can be rewritten in the form of

$$S/N = \frac{P_S}{NEP \cdot B} . \tag{4.1.12}$$

The main conclusions from the last two equations are the following: the signal-to-noise ratio is proportional to the overall efficiency $\sigma\eta$ and to the total signal power collected, but it is independent

of the local oscillator power (provided that $A_{LO} >> A_S$). The signal-to-noise ratio cannot be improved by increasing the local oscillator power. Since excessive LO power results in additional (thermal) noise due to heating of resistive components in the detector, the local oscillator power used should be no greater than that necessary to make the detector shot noise the dominant noise source - assuming the availability of adequate power. Not directly retrievable from the above treatment but shown elsewhere, e.g. by Forrester (39), is the observation that the power spectrum of the detector current exactly reflects the power spectrum of the optical signal.

We will return to the noise problem in section 4.3, where the signal-to-noise ratio of the whole signal processing chain will be discussed

4.2 State of the Art of Sensitive Wide-Band Detectors

The selection of a suitable detector is mainly governed by the following considerations :

(a) the wavelength of the laser used,
(b) the sensitivity or NEP of the detector at that wavelength,
(c) the detector bandwidth, and
(d) the ease and reliability of operation.

We will briefly discuss the selection of a suitable detector in terms of these parameters.

The number of laser wavelengths that is available in the FIR is restricted and depends on the chance existence of molecules which can be pumped efficiently by a CO_2 laser and which emit strongly in this wavelength region - see section 3.1. When selecting one of these wavelengths, it is necessary to ensure that there exists a powerful c.w. or quasi-c.w. transition (some tens of mW) nearby, for use as a local oscillator for heterodyne detection. The local-oscillator frequency must

not be separated from that of the pulsed FIR laser by more than the detector band-width. Finally, plasma conditions and the scattering geometry employed influence the choice of wavelength.

The sensitivity of the detector is governed by noise considerations, as discussed in section 4.1 and should approach 10^{-18} W/Hz, at least, to ensure compatibility with currently-available FIR-laser powers.

The detector bandwidth has to be large enough to accommodate the expected spectrum of the scattered laser radiation. The spectral width can be adjusted within certain limits by changing the scattering angle. A lower limit is set by the requirement that the spectrum has to be significantly broader ($\gtrsim$ 10 times) than the FIR laser line to distinguish the contribution due to ion thermal motion from stray laser "light". The width of a single mode FIR laser line is of the order of 50 MHz. Thus a detector bandwidth of at least 500 MHz is necessary. The upper limit, $\sim$ 2 GHz, is often set by other components in the signal processing chain (e.g. the IF amplifier). The detection bandwidth B does not necessarily have to cover the range from 0 to B Hz. However, if the difference frequency between the local oscillator and pulsed laser is υ and the scattered radiation has spectral half-width $\Delta\upsilon$, the detection system has to cover the spectral range from υ to $\upsilon + \Delta\upsilon$ for single sideband operation.

Ease and reliability of operation are not of prime importance in a feasibility experiment but have to be considered for routine operation. Room temperature operation of a device is convenient, but with the current state of cryogenic technology the need to cool a detector is not in itself a great disadvantage. Combined with the need for frequent maintenance or adjustments it can, however, be a great impediment. Cooled bulk device detectors such as photoconductors are therefore preferable to cooled point-contact devices and maybe even to such devices operated at room temperature, from this point of view.

It is mainly the requirements of high speed (large band-width) and low NEP which restrict the choice of a suitable detector, out of the large number currently available, to basically one of three types :

the Nb -Nb superconducting Josephson junction, the GaAs point-contact Schottky diode and the Ga-doped Germanium photoconductor. The only possible way of achieving the necessary sensitivity in any one of these devices is to operate it as a heterodyne receiver. This allows a high conversion gain. The combination of strong directivity and frequency selectivity permits a small noise band-width.

In the remainder of this subsection, 4.2, we review the current state of development of the three types of detector best suited to our needs. Emphasis is placed on the Schottky diode which at present is the most highly-developed of the three and on which the detection system proposed for use on JET is based.

4.2.1 The Schottky - Diode Detector

The metal-semiconductor contact, or Schottky-barrier diode has a long history of utilization as a mixer element. Its use has progressed to higher and higher frequencies. Mixing at 3 THz has for example been achieved with a GaAs Schottky diode by Fetterman (40). In order to minimise parasitic loss, as the operating frequency is increased the area of the diode has to be reduced. This poses technical difficulties.

The mixer conversion loss L_c, defined as the ratio of available power from the FIR source to the power observed in the IF load, can be expressed in the form (41)

$$L_c = L_o L_p \qquad (4.2.1)$$

The intrinsic conversion loss L_o is the loss arising from the conversion process within the nonlinear resistance of the diode and includes the impedance mismatch losses at the FIR and IF ports. The parasitic loss L_p is associated with the parasitic elements of the diode, the junction capacitance C (typically 10^{-15}F) and spreading resistance R_S (typically some 10 Ω). This resistance results from the constricted current flow (diameter d) in the semiconductor near the contact. R_S is in series with the parallel elements C and the nonlinear barrier impedance at the signal frequency. The deleterious effect of these two parasitic elements on the conversion efficiency is the following: C allows current to bypass the junction resistance, while R_S is a source of power dissipation, heat production and, consequently, of excess diode noise. Since $C \propto d^2$, $R_S \propto d^{-1}$ and the cutoff frequency $\omega_c = \frac{1}{R_S C}$, d has to be reduced as the frequency of operation is increased.

With the development of electron beam fabrication techniques, the ability to produce Schottky barriers with dimensions of the order of a few hundred Ångstroms is imminent. However, the effect of a reduction in area on the intrinsic conversion loss L_o must also be evaluated to determine overall mixer performance. The dependence of L_o on area is connected with the requirements of impedance matching and, as shown by McColl (41), can increase rapidly as the area is reduced. Careful optimisation of the diode parameters is therefore necessary in constructing a Schottky mixer for sensitive high-frequency operation. In general, characterizing a particular diode by contact diameter, capacitance and dc resistance determines its performance. Fig. 4.2.1 reproduced from (42) shows an optimised diode size for operation at wavelengths below 1 mm. At a frequency of 780 GHz (corresponding to the 385 µm line of D_2O) the optimum point contact is found to be ∿ 1 µm diameter. The video sensitivity at 385 µm is of the order of 1 V/W.

It is considered unlikely that the wavelength range over which Schottky diodes operate can be extended to wavelengths shorter than about 250 μm without considerable development, and that 200 μm represents the limit.

Under most conditions the principal source of noise from a dc-biased Schottky barrier is shot noise. Hence, our previous observations on noise in heterodyne detection can directly be applied. A further consequence of this is that the cooling of Schottky diodes, and hence reduction of thermal noise, cannot significantly improve performance of the device. Factors of 2 to 4 have been observed by cooling down to cryogenic temperatures.

4.2.2 Josephson-Effect Heterodyne Receivers

Quantum mechanical phenomona which occur when two superconductors are weakly connected together, allowing the flow of superconducting electrons, are labelled by the generic term "Josephson effect". The barrier, or junction, in such a weakly-coupled system of two superconductors can take various forms : a thin ($\sim$ 15 Å) layer of insulator, such as oxide, semiconductor or normal metal, a connection of two superconductors by a small ($\sim$ 0.5 μm diam.) metallic bridge, or a point contact. So far, all successful Josephson effect mixers have been built with point-contact Josephson junctions.

Contrary to other types of mixers, Josephson junctions are active. They generate internal oscillating currents which interact with radiation induced currents to give rise to detection and other phenomena. We do not propose to discuss the relatively complex mechanisms taking place in a Josephson mixer since there are adequate references to these in the literature (43 to 47).

The strong nonlinearity of the Josephson junction reduces the required local oscillator power and hence the sensitivity to noise generated by the local oscillator signal. The conversion efficiency depends on the local oscillator power used. One finds an optimum local oscillator power which maximises the conversion efficiency. In the submillimeter range, local oscillator powers from 1 - 10 μW are necessary. This low power requirement greatly simplifies the method of coupling the local oscillator to the junction. For example, a beam splitter which transmits most of the signal, and reflects a small fraction of the local oscillator power can be used.

As mentioned above, the Josephson detector is an active device, its detection process is a mixing rather than a lossy resistive effect. Hence, contrary to other rectifying detectors, a modest conversion

gain ($\sim$ 1) is possible when used as a mixer: more power can exit at the intermediate frequency than arrives at the signal frequency.

The conversion gain is related to the ratio of output impedance to input impedance. For high conversion gain a high output impedance is desirable. This may conflict with the requirement of matching the input impedance of high-speed IF-amplifiers which are generally designed for 50Ω.

The sensitivity of Josephson mixers is very high although decreasing towards shorter wavelength as λ^{-2}. Probably about 250 μm represents the short wavelength limit for useful operation. Theory conservatively predicts a single sideband mixer noise temperature of $\sim 300^{\circ}K$ at 0.5 mm. In an experiment at 337 μm (48) a system noise temperature of $500^{\circ}K$ ($1.4 \cdot 10^{-20}$ W/Hz NEP) was measured, which was, however, IF-amplifier dominated. This is an order of magnitude above the quantum noise limit, $h\nu/k = 42^{\circ}K$ at 337 μm.

Josephson junctions are sensitive over a wide band, stretching far into the long wavelength region. To avoid saturation of the mixer due to the high level of electron cyclotron emission from the plasma at wavelengths longer than $\sim$1mm, in a Thomson scattering measurement, pre-mixer bandpass filtering is necessary. This could be achieved, e.g.,with a wire-mesh Fabry-Perot interferometer.

Current dependence is on point-contact Josephson junctions, rather than on intrinsically more stable and reproducible forms. Unfortunately, it is not easy to build thermally-recyclable point-contact junctions. The problem has, however, been solved in a 2.6mm mixer (49) with a technique that has also been applied to sub-millimetre wavelengths.

Operating in the same wavelength range, Schottky diodes and Josephson junctions are direct competitors for a receiver system in Thomson scattering arrangements. While Josephson devices have some very attractive features such as low power requirements for the local oscillator and potentially very high sensitivity, their state of development trails behind that of Schottky

diodes. In this design study we have opted for existing technology whenever possible, rather than rely on future development. Thus, Schottky receivers are chosen in preference to Josephson-junction receivers because of the commercial availability of the former.

4.2.3 Photoconductive Detectors

Photoconductive detectors depend on the change of the electrical conductivity of certain materials, usually semiconductors, when subjected to radiation, by processes other than a temperature change of the material. The photoconductive process often involves the excitation of charge carriers across an energy gap, which is accomplished by individual radiation quanta. This requires a minimum quantum energy resulting in a long-wavelength cut-off for the detection process. FIR photoconductive detectors require cryogenic operating temperatures, usually in the liquid helium range.

The element, of dimensions a few mm or less, is typically biased from a battery, through a load resistor. Changes of the detector conductance are observed across the element or the load resistor. The intrinsic response time of the photoconductive element is short. However, to achieve high responsivity, the resistance of the element has to be large, so that relatively small system capacitances can limit practical system speed. Usually a compromise has to be made between fast response time (large bandwidth) and high sensitivity (NEP).

IF amplifiers with large bandwidth usually have low input impedances (50 Ω) so that impedance matching becomes a problem. It is often necessary to use cryogenically-cooled amplifiers, placed near the detector.

The operating principle of Ge-photoconductors is based on the excitation of impurity holes or electrons into the conduction band. The typical response time of about 100 ns can be reduced to 1 ns or less by increasing the compensatory dopant level, usually with degradation of responsivity. They operate at wavelengths up to about 140 μm.

To the best of our knowledge, the NEP and bandwidth necessary for a Thomson-scattering measurement have not been simultaneously achieved for a doped Ge detector - although both have been achieved independently.

Gornik has described a Ge : Ga detector with a measured response time of 0.5 ns (50). It has not, as yet, been operated in the heterodyne mode. In his review paper (6) Blaney indicates that heterodyne NEP's of 10^{-18} to 10^{-19} might be possible and in a recent publication Haller (51) reports a video NEP of $2.4 \cdot 10^{-17}$ $WHz^{-\frac{1}{2}}$ at 94 μm. If this is converted into a heterodyne NEP by means of the approximate formula (6)

$$NEP_{HET} = NEP_{VID} \cdot B_{IF}^{-\frac{1}{2}} \qquad (4.2.2)$$

one obtains the figure of $7.6 \cdot 10^{-22}$ for a 1 GHz bandwidth. Despite the fact that this figure is probably over optimistic, it lends credibility to the optimism expressed by experts in the field (50).

4.3 Description of the Signal Processing Equipment

The output of the mixer, or IF-amplifier, is a fluctuating noise-like signal with zero mean amplitude and a frequency-spectrum which is that of the scattered radiation. The signal has to be processed so that one obtains a certain number of points on a frequency versus intensity distribution, the half width of which yields the plasma ion temperature. As will be shown later, 10 is a reasonable number of points to choose but even as few as 6 points will still permit us to obtain an accurate value of ion temperature by spectral fitting.

We will describe two possible signal processing chains. The first one is most likely to be implemented in an initial scattering measurement. The second one is described mainly because it allows us to model certain additional aspects of general interest.

As shown in fig. 4.3.1, the signal processing chain consists of a receiver (diplexer and mixer) and an IF-amplifier followed by a multiplexer-filter, a power detector and an integrator in the first chain or a digitizer and a microprocessor, or mini computer, to perform a discrete Fourier transformation in the second chain. The centre frequency of the IF-signal is not necessarily zero, but depends on the frequency offset between the pulsed laser and the local oscillator. In case this offset is too large for the multiplexer-filter and follow-up electronics, a second local oscillator-mixer pair has to be inserted between the IF-amplifier and the multiplexer.

The multiplexer-filter comprises an array of filters with adjoining passbands, of equal width, that are rectangular, to a good approximation. Filter arrays with 10 channels, each of width $\sim$ 200 MHz, are commercially available (52). Such arrays are easier to construct if the frequency range covered is, for example, 2-4 GHz, instead of from 0-2 GHz. Thus, a difference of a few GHz between the frequency of the pulsed laser and that of the local oscillator would be desirable, from this point of view. We also remark here that an adequate frequency offset is necessary to separate the power spectrum due to the ions into two halves, one on either side of the probing laser frequency. This permits any asymmetries in the spectrum, due for example to a drift between ions and electrons, to be revealed. For a laser frequency and local oscillator frequency that are coincident, the two halves of the spectrum would be superposed.

Power detectors and integrators are commercially available. If necessary, the second mixer could comprise an in-phase and quadrature detector - these are available in package form.

Turning to the second signal processing chain, a number of transient digitisers are commercially available, although their performances, as yet, are too limited for our applications. We will return to this aspect, in more detail, in section 4.3.3.

With further development, two other devices might prove to be useful in the signal processing chain. The first of these is the Bragg cell real-time spectrum analyser. At present, the maximum bandwidth of 500 MHz is too restrictive. The second device of potential interest is the surface-acoustic-wave dispersive delay line, as described by Fetterman (53). Once again, its performance is limited by the bandwidth.

4.3.1 Signal to Noise in the Electronic Spectrum Analyzer

The signal-to-noise ratio at the output of the IF-amplifier has been discussed in section 4.1. We will briefly analyse its modification by the remainder of the signal processing chain which is basically an electronic spectrum analyzer. Since the noise current is a statistically-fluctuating signal, we expect some improvement in the final signal-to-noise ratio due to the averaging process of the integrator. The influence of a filter-squarer-integrator chain (fig. 4.3.1) on the signal-to-noise ratio has been discussed by Cummins and Swinney (54) using standard methods of electrical signal analysis.

Let $P_i(\omega)$ be the spectrum of the detector current $i(t)$. The fluctuations and the average signal current at the output of the chain are

$$\langle i_{out} \rangle = C\, P_i(\omega) \tag{4.3.1}$$

$$\left[\langle (\Delta i_{out})^2 \rangle \right]^{\frac{1}{2}} = C\, P_i(\omega)\, (1 + \Delta\upsilon \cdot \tau)^{-\frac{1}{2}}$$

where τ is the integration time (laser pulse length), $\Delta\upsilon$ the width of the filter bandpass and C a constant. The input current spectrum $P_i(\omega)$ consists of a signal component $P_S(\omega)$ and a noise background $P_N(\omega)$, so that

$$P_i(\omega) = P_S(\omega) + P_N(\omega) \tag{4.3.2}$$

Only the fraction $P_S(\omega)/P_i(\omega)$ of the observed output current $\langle i_{out} \rangle$ is the desired signal, but both $P_S(\omega)$ and $P_N(\omega)$ contribute to the fluctuations in i_{out}. Thus the final signal-to-noise ratio in the observed spectrum is the ratio of the signal amplitude $\langle i^S_{out} \rangle = CP_S(\omega)$ to the r.m.s. fluctuation in the signal plus noise,

$$\left[\langle (\Delta i_{out})^2 \rangle \right]^{\frac{1}{2}} = C(P_S(\omega) + P_N(\omega)) \, (1 + \Delta\upsilon\tau)^{-\frac{1}{2}},$$

viz.

$$(S/N)_{out} = \frac{P_S(\omega)}{P_S(\omega) + P_N(\omega)} \, (1 + \Delta\upsilon\tau)^{\frac{1}{2}} \tag{4.3.3}$$

$$= \frac{P_S(\omega)/P_N(\omega)}{1 + P_S(\omega)/P_N(\omega)} \, (1 + \Delta\upsilon\tau)^{\frac{1}{2}}$$

It can also be shown that the noise statistics follow a χ^2-probability distribution with the number of degrees of freedom n given by $n = 2(\Delta\upsilon \cdot \tau + 1)$, for a Gaussian noise distribution at the input.

Let us assume that the multiplexer filter consists of N_C filters, each of bandwidth $\Delta\nu$, such that the total bandwidth covers that of the receiver

$$N_C \cdot \Delta\upsilon = B \tag{4.3.4}$$

Since the noise power in one channel is $P_N = B/N_C \cdot (NEP)$ the signal-to-noise ratio per channel becomes

$$(S/N)_C = \frac{P_S}{P_S + NEP \cdot B/N_C} \sqrt{1 + \frac{B \cdot \tau}{N_C}} \tag{4.3.5}$$

We see that for $P_S >> P_N$ the signal-to-noise ratio is independent of the scattered power P_S and depends only on the product of B and τ. Thus, under this condition, no improvement in S/N can be achieved by increasing the incident laser power P_0; the only recourse, for a fixed band-width, is to increase the laser pulse duration τ.

Let us suppose that the FIR laser delivers a pulse of constant energy, i.e. $P_0 \propto 1/\tau$, and that a pulse of duration τ_0 yields a scattered power $P_S = P_N$ in a particular channel. Then a pulse of duration τ yields a scattered power $P_S = P_N \tau_0/\tau$ in that channel. We find that the pulse duration τ which maximises the signal-to-noise ratio is given by $\tau = \tau_0 (1 - 2 N_C/(B \cdot \tau_0))$. Thus, for $B \cdot \tau_0/N_C \gtrsim 20$, $\tau \simeq \tau_0$. In other words, the best signal-to-noise ratio in a scattering measurement is obtained by operating the FIR laser so that it produces a pulse of duration such that the total scattered power P_S equals the noise power $P_N = NEP \cdot B$. In Table 4.3.1 we tabulate the variation of S/N with τ, for $N_C = 10$ and $B = 2$ GHz and with $P_S = P_N$.

4.3.2 Computer Simulation of Spectral Fitting

A computer simulation program has been used to estimate the accuracy in the determination of T_i for various values of S/N. Using a Monte Carlo technique, for each channel a noise signal is generated, according to a χ^2 distribution, and is superposed on the signal due to the scattered power in that channel, calculated using an analytical expression obtained from standard scattering theory (2). This resultant noisy spectrum is a realistic approximation to what the experimenter would obtain in the laboratory. A nonlinear least squares fitting routine is then applied to identify the theoretical spectrum which best fits the noisy one, thereby enabling an ion temperature to be determined. The procedure is then repeated about thirty times, always using the same noiseless spectrum initially, each time with a different random noise signal in the various channels. In this way,

the mean value of T_i and the shot-to-shot statistical variation in T_i can be determined.

The fitting routine allows a multiparameter fit, thus simultaneously fitting T_i, T_e and n_e. Alternatively, it can be assumed that T_e and n_e are known from an independent measurement with a certain accuracy ΔT_e and Δn_e. Values of temperature and density for each simulation are then randomly chosen from Gaussian distributions having the measured values as means, with variances ΔT_e and Δn_e.

In Table 4.3.1 the results obtained from the simulations in the case of a pure deuterium plasma are tabulated. The mean ion temperature $\bar{T}_i$ and the error $\Delta T_i/T_i$ associated with estimating the ion temperature are given for different values of the laser pulse duration τ. The simulations are for B = 2 GHz and N_C = 10. It is assumed that $P_S = P_N$. The ion temperature used in calculating the initial spectrum, to which noise is added, is 1 keV. Each value of $\Delta T_i/T_i$ and $\bar{T}_i$ is calculated using the statistics of 31 simulations. It can be seen that, although the mean temperature derived from 31 spectra is insensitive to the pulse duration T, the error associated with the ion temperature derived from a single spectrum rapidly increases with decreasing pulse duration. Thus, for example, for a pulse duration of 5 μsec the values of ion temperature from the 31 spectra were spread between 917 and 1078 eV, in a distribution that approximated to a Gaussian, yielding an error of $\pm$ 73 eV at the 90% confidence limit, while for a pulse duration of 100 nsec the values were spread between 419 and 1561 eV, yielding an error of $\pm$ 429 eV. Consequently, on a single shot, to obtain a value of T_i with an accuracy better than $\pm$ 20% a laser pulse of duration greater than 1 μsec will be needed when using a detector of bandwidth 2 GHz.

In the above, it was assumed that both T_e (set equal to T_i) and n_e were precisely known. The effects of errors in the values of these parameters will be discussed in the section 5.5, when conditions pertinent to JET will be investigated by means of the simulation code.

4.3.3 Spectral Analysis with Digital Fourier Transformation

As illustrated in Fig. 4.3.1 an alternative approach to analysing the signal from the mixer is to record it on a transient digitizer and to compute the spectrum by discrete Fourier transformation. While this approach is conceptually simple, its implementation is not without difficulties.

Digitization of the detector signal i(t) yields N discrete points i_n of total length T and separation Δt. Discrete Fourier transformation of the N real values i_N according to

$$F_m^r = \sum_{n=0}^{N-1} i_n \cos \frac{2\pi mn}{N}$$

$$F_m^i = -\sum_{n=0}^{N-1} i_n \sin \frac{2\pi mn}{N} \qquad (4.3.6)$$

gives N/2 real Fourier terms F_m^r and N/2 imaginary Fourier terms F_m^i from which the power spectrum is obtained, since

$$Sm = (F_m^r)^2 + (F_m^i)^2. \qquad (4.3.7)$$

The integer m can take on values between 0 and N/2 - 1, S_0 is the dc term and $S_{(N/2-1)}$ is the highest possible frequency before fold-over (aliasing) occurs. The folding frequency is

$$f_F = \frac{1}{2\Delta t} = \frac{N}{2T} \cdot \qquad (4.3.8)$$

If the series i_n follows a Gaussian random distribution (which is true for the signal and noise component of the current) then the Fourier components F_m^r and F_m^i also follow a Gaussian distribution. The two distributions in frequency space have the same mean value (zero) and variance σ_o and can thus be combined into one distribution. Forming the power spectrum according to (4.3.7) signifies drawing a sample of two elements and forming the sum of the squares, which is the definition of a χ^2-distribution with 2 degrees of freedom (55).

If a number of M neighbouring frequency points are lumped together in a channel of width

$$\Delta\upsilon = \frac{M}{N/2} f_F \tag{4.3.9}$$

then the total intensity per channel is

$$S_m^M = \sum_{m=1}^{M} (F_{m\epsilon M}^r)^2 + \sum_{m=1}^{M} (F_{m\epsilon M}^i)^2. \tag{4.3.10}$$

This is a χ^2-distribution of 2M degrees of freedom. The expectation value and variance of a χ^2-distribution of n degrees of freedom, based on a Gaussian of variance σ_o are (55)

$$\begin{aligned} E(\chi^2) &= n \cdot \sigma_o^2 \\ \sigma(\chi^2) &= \sqrt{2n} \cdot \sigma_o^2 \end{aligned} \tag{4.3.11}$$

Hence for (4.3.10) one finds

$$\begin{aligned} E(S_m^M) &= 2M\sigma_o^2 = P(\omega) \\ \sigma(S_m^M) &= 2\sqrt{M}\,\sigma_o^2 \end{aligned} \tag{4.3.12}$$

The power $P(\omega)$ again consists of a signal and noise component

$$P(\omega) = P_S(\omega) + P_N(\omega). \tag{4.3.13}$$

The final signal-to-noise ratio, viz the ratio of the expectation value of the signal component to the variance of the total signal, is thus obtained as

$$S/N = \frac{E(P_S(\omega))}{\sigma(P_S(\omega) + P_N(\omega))} = \sqrt{M}\,\frac{P_S(\omega)}{P_S(\omega) + P_N(\omega)} \qquad (4.3.14)$$

If the detector bandwidth B is chosen equal to the folding frequency, then from (4.3.8) and (4.3.9)

$$M = T\Delta\upsilon \qquad (4.3.15)$$

and (4.3.14) becomes

$$S/N = \frac{P_S(\omega)}{P_S(\omega) + P_N(\omega)} \sqrt{\Delta\upsilon \cdot T} \qquad (4.3.16)$$

which is identical to (4.3.3) for $\Delta\upsilon \cdot T \gg 1$. Hence, with respect to the signal-to-noise ratio, the signal processing method using the technique of Fourier transformation is equivalent to that using filters and integrators.

Mathematically the Fourier transform method is interesting because of its greater transparency than the filter method. Experimentally, however, it has a severe drawback: the number of points to be digitized, N, is connected to the detector bandwidth B and the pulse duration T by

$$N \geq 2\,BT \qquad (4.3.17)$$

This is due to aliasing and is sometimes referred to as the Nyquist condition (56). For a given bandwidth and a given digitizer this limits the pulse length, as illustrated in Table 4.3.2.

Turning to examine the performance of a commercially-available transient digitizer, the Tektronix type 7912 AD records 512 discrete points and has a bandwidth of 1 GHz. The maximum pulse length of 256 ns is too short for an adequate precision in T_i, as shown earlier. Even using two digitizers and a 512 ns pulse length, an experiment seems marginally possible, but for this the problem of precise sequential synchronization of the two digitizers has to be solved. The Fourier transform method becomes feasible if at least 2000 points in a 1 μs pulse can be recorded with 1 GHz bandwidth. With the rapidly developing field of electronics it is not unreasonable to forecast the development of such a digitizer, provided it has a potentially large market.

A computer programme has been developed to simulate signal processing with the Fourier transform method. A time series representing the detector signal is produced according to

$$i(t) = \sum_{n=1}^{N} \sqrt{P_S(\omega)}\ \cos(\omega_n t + \phi_n)\ \sqrt{\Delta\upsilon_n} \qquad (4.3.18)$$

where the spectrum $P_S(\omega)$ is divided into N unequal strips $\Delta\upsilon_n$. The phases ϕ_n and width $\Delta\upsilon_n$ are random ($\overline{\Delta\upsilon_n} = B/N$). Eq. (4.3.18) ensures that the current follows a random Gaussian distribution and has the desired spectrum $P_S(\omega)$ (54). To this, random noise is added with an average amplitude governed by the desired S/N ratio. An N-point Fourier transform is performed and the N/2 spectral points are divided up into channels. The number of channels can vary from a reasonable lower limit ($\sim$ 6) up to N/2. A least squares fit is then performed to extract T_i.

We varied the number of channels within this range to see if there is an optimum number. This does not seem to be the case.

More importantly, we investigated the influence of different laser pulse shapes on the precision in the determination of T_i. We simulated this effect by convoluting the current of eq. (4.3.18) with the shape of the laser pulse. We studied three types of laser

pulse of equal duration and equal energy content (shape under curve), viz. a square pulse, a triangular pulse and a peak-tail pulse typical of experimentally-observed CO_2 laser pulses. The latter was obtained by summing two Gaussians of unequal height and width. The three pulses are shown to scale in fig. 4.3.2. Gaussian spectra were chosen for this test and hence Gaussian curves of variable width were fitted to the simulated spectra. Table 4.3.3 shows the results of 30 simulations/spectrum for spectra obtained from a 200 point Fourier transform.

The precision obtained with a peak-tail pulse shape is about half that of a triangular pulse shape which in turn is about half as good as a square pulse. Systematic errors are also quite large for non-square pulses. Each of the 25 channels contained M = 4 points, so that for a post-mixing S/N of unity the overall S/N ratio according to eq. (4.3.14) is $\sqrt{4} \cdot \frac{1}{2} = 1$. This small value explains the large errors in the width "measurement".

The importance of square pulses prompted us to investigate experimental methods of pulse shaping, as discussed in section 3.2.2.

4.4 Proposed Detection System for JET

Having, in the previous sections, reviewed the various detector types and the different methods of signal processing, together with estimates of the accuracy with which T_i can be determined, in this final section we describe a detection system for proposed use on JET. In section 3, we have described the D_2O laser operating at 385 μm as being the most-developed pulsed FIR laser and we have given the design of such a laser for use on JET. Consequently, the proposed detection system is also suited to this wavelength.

A Schottky diode receiver used for a scattering measurement with the 385 μm line of D_2O would consist of a quasi-optical diplexer followed by a mixer, incorporating an IF low-pass filter. The signal would be amplified by a large-bandwidth, low-noise IF amplifier and processed by signal processing electronics which have been described earlier (in section 4.3). A promising solution for a diplexer would be a polarisation rotating Michelson interferometer, similar to the one described by Wrixon (42).

Referring to fig. (4.4.1), the incoming, vertically polarised signal is collimated by means of a plano-concave lens, which has surface matching grooves machined on the plane side. The signal passes unimpeded through a horizontal wire grid where it is joined by the horizontally-polarized local oscillator signal which has been totally reflected by the grid. The combined signal and local oscillator beams then enter the interferometer which consists of a wire grid oriented at 45° and two corner reflectors which change the plane of polsarisation 90° upon reflection.

When the round trip differs by one half wavelength at the IF frequency, signal and local oscillator beams will emerge through the plano-convex lens from the diplexer with the same polarisation. With lenses made from high-density polyethylene the losses of this system should be small. Transmission losses could be eliminated completely by alternative arrangements of the Michelson interferometer. Fig. 4.4.2 shows an example: the diplexer consists of a corner reflector and two stretched Mylar film beam splitters. Focussing the output onto the detector would be achieved using an ellipsoidal mirror.

The quasioptical mixer would be a GaAs Schottky diode, mounted in a corner cube reflector configuration. As shown in Fig. 4.4.3, a tungsten whisker antenna, of length 4 λ, is mounted parallel to two highly polished surfaces of the corner reflector and perpendicular to the ground plane. It has been shown (57) that the performance

of such a traveling wave antenna can be improved by 12 dB by the presence of a corner reflector. The contacting is achieved by positioning the chip stud so that the etched antenna whisker is lowered onto one of the many diodes on the GaAs chip. The antenna whisker is directly bonded to the centre conductor of the 50Ω coaxial line connector. The signal and local oscillator frequencies are decoupled by the bend in the antenna and no additional filtering is required.

Farran Research Associates, Cork, Ireland are able to supply a complete receiver incorporating diode, mixer, diplexer, DC bias tee and supply, and IF amplifier for operation at 385 μm. Its specifications would be: Overall double sideband system temperature of less than 20,000°K, corresponding to an NEP of $< 3 \cdot 10^{-19}$ W/Hz, double sideband operation with ∿ 1 GHz IF bandwidth centred at the difference frequency of the pulsed laser and local oscillator. About 10 to 20 mW local oscillator power would be necessary.

Table 4.3.1

Variation of Signal-to-noise Ratio and Accuracy in Determining T_i with Laser Pulse Duration

τ(sec)	S	$\frac{\delta T_i}{T_i}$ (%)	$\bar{T}_i$(ev)
5×10^{-6}	15.82	7.3	990
2×10^{-6}	10.01	12.0	1011
1×10^{-6}	7.09	20.3	1028
5×10^{-7}	5.02	26.7	1009
2.5×10^{-7}	3.57	29.8	1039
1×10^{-7}	2.29	42.9	924

For $P_S = P_N$, $S = 0.5 \sqrt{1 + \frac{B \cdot \tau}{N_c}}$

where $B = 2$ GHz

$N_c = 10$

$\frac{\delta T_i}{T_i}$ is the 90% confidence limit , i.e. for any single spectrum there is a probability of 0.9 that the ion temperature derived will lie within the error limits quoted.

The true value of T_i in these simulations is 1.0 keV.

Table 4.3.2

The limits on pulse length due to aliasing in the discrete Fourier transform approach

No of points that can be digitized	detector bandwidth	max. pulse length
512	1 GHz	256 ns
512	2 GHz	128 ns
1024	1 GHz	512 ns
1024	2 GHz	256 ns

Table 4.3.3

The influence of the laser pulse shape on the precision of a T_1 measurement.

Gaussian spectra of width W fitted to 25 channels of a 200-point Fourier-transformed random signal with Gaussian spectrum.

$\overline{\Delta W}$ average deviation of width W from true width

$\overline{+}\Delta W/W$ accuracy of a single measurement of curve width (sample variance/true width)

pulse shape	S/N >> 1		S/N = 1	
	$\overline{\Delta W}$ (%)	$\overline{+}\ \Delta W/W$ (%)	$\overline{\Delta W}$ (%)	$+\ \Delta W/W$ (%)
square	+ .05	8.5	- 2.6	12.0
triangular	- 5.8	18.5	+ 5.7	30.5
peak-tail	- 9.6	34.0	+ 19.4	43.0

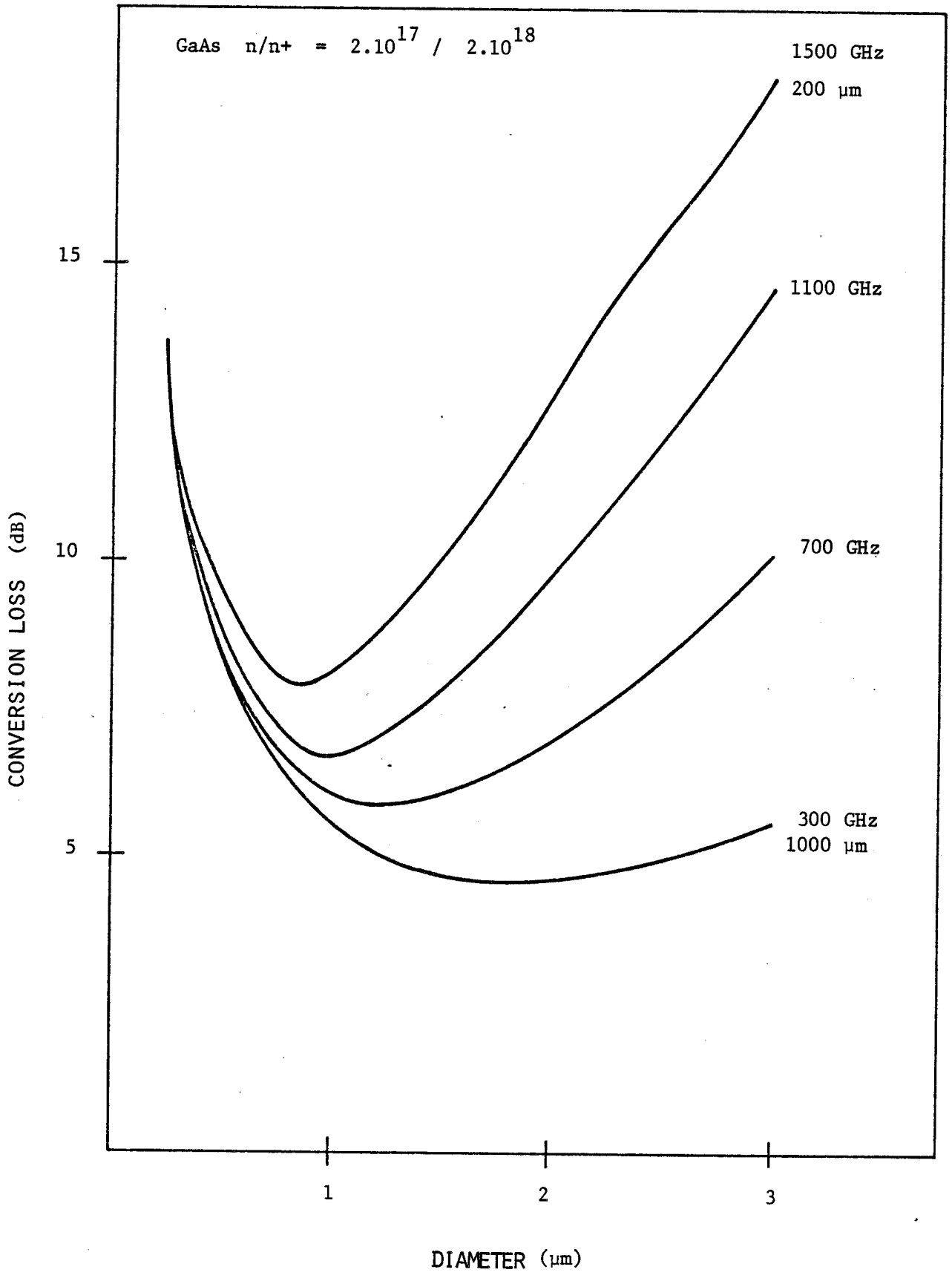

Figure 4.2.1 : Variation of Conversion Loss in Schottky Diode with Diameter of Point Contact

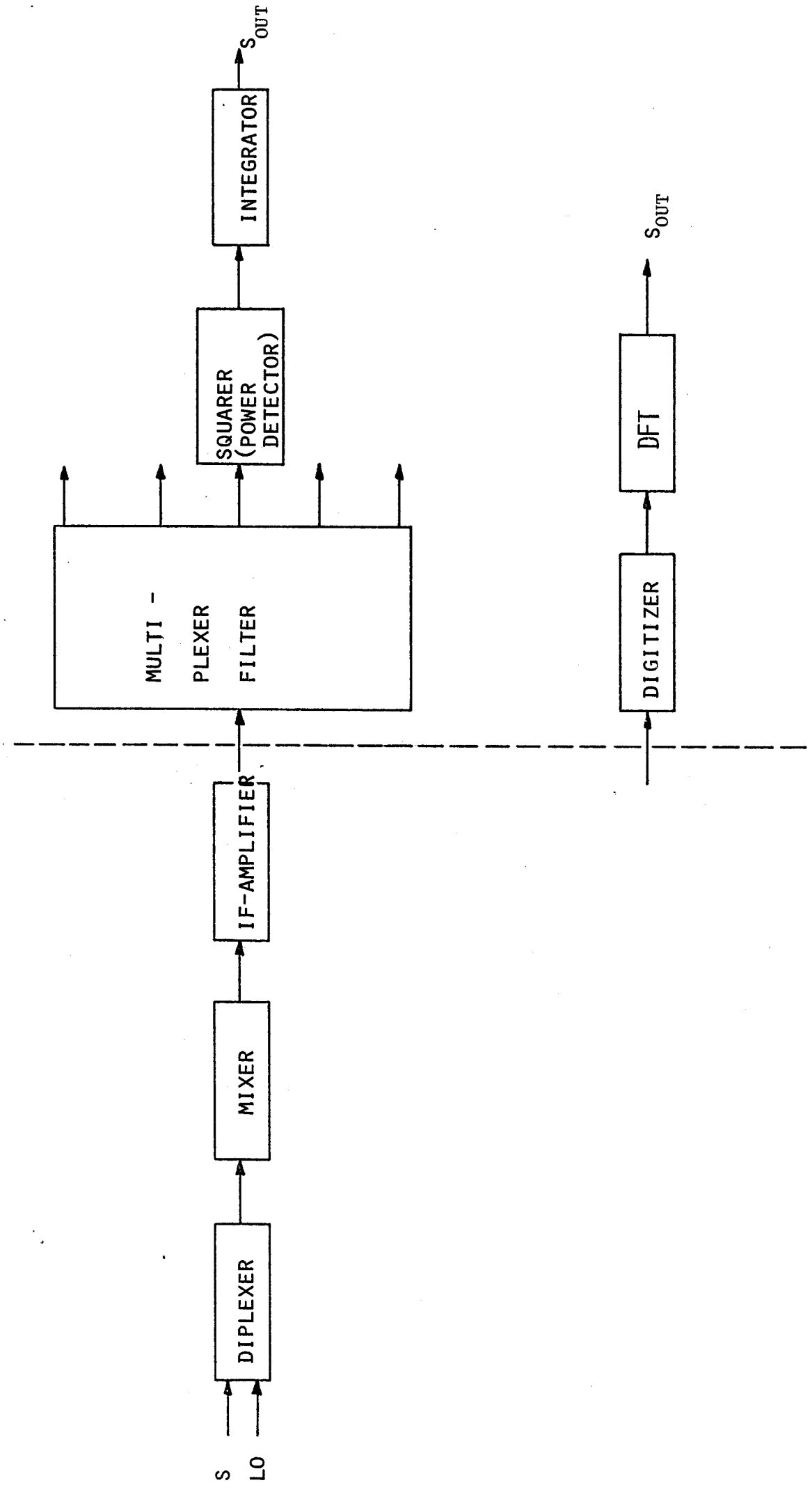

Figure 4.3.1 : The Signal Processing Chain

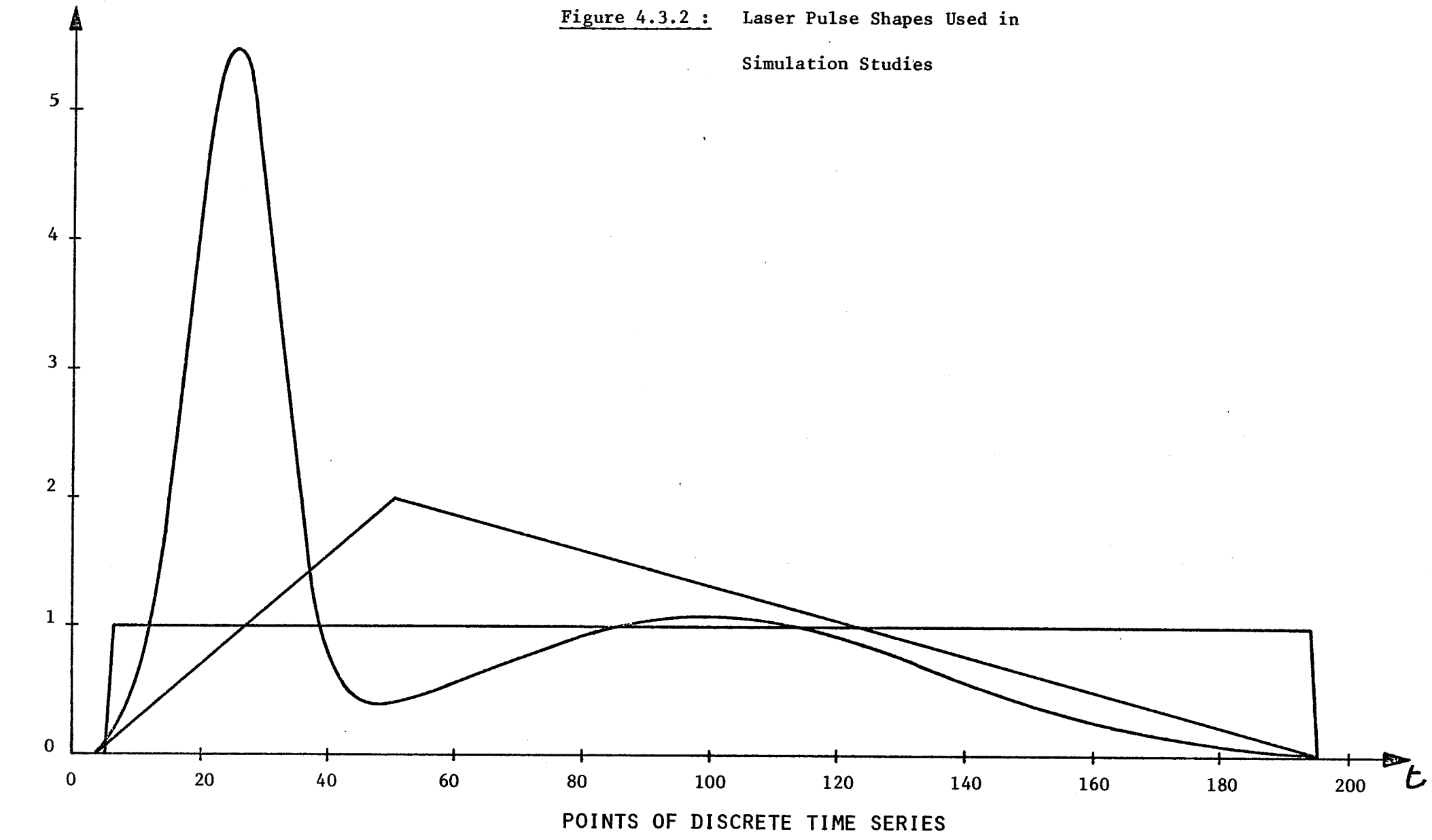

Figure 4.3.2 : Laser Pulse Shapes Used in Simulation Studies

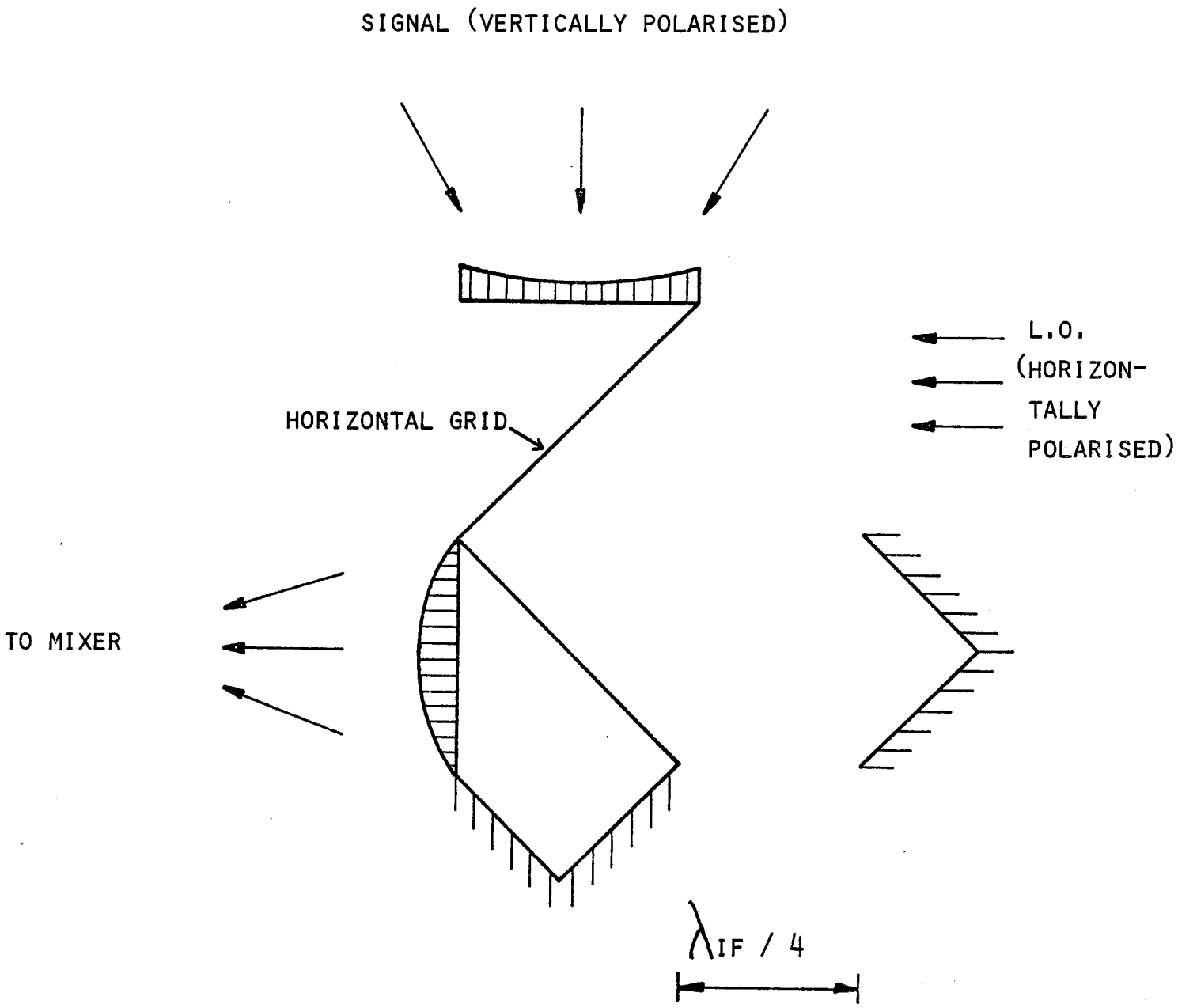

Figure 4.4.1 : Diplexer Based on Polarisation Rotating Michelson Interferometer

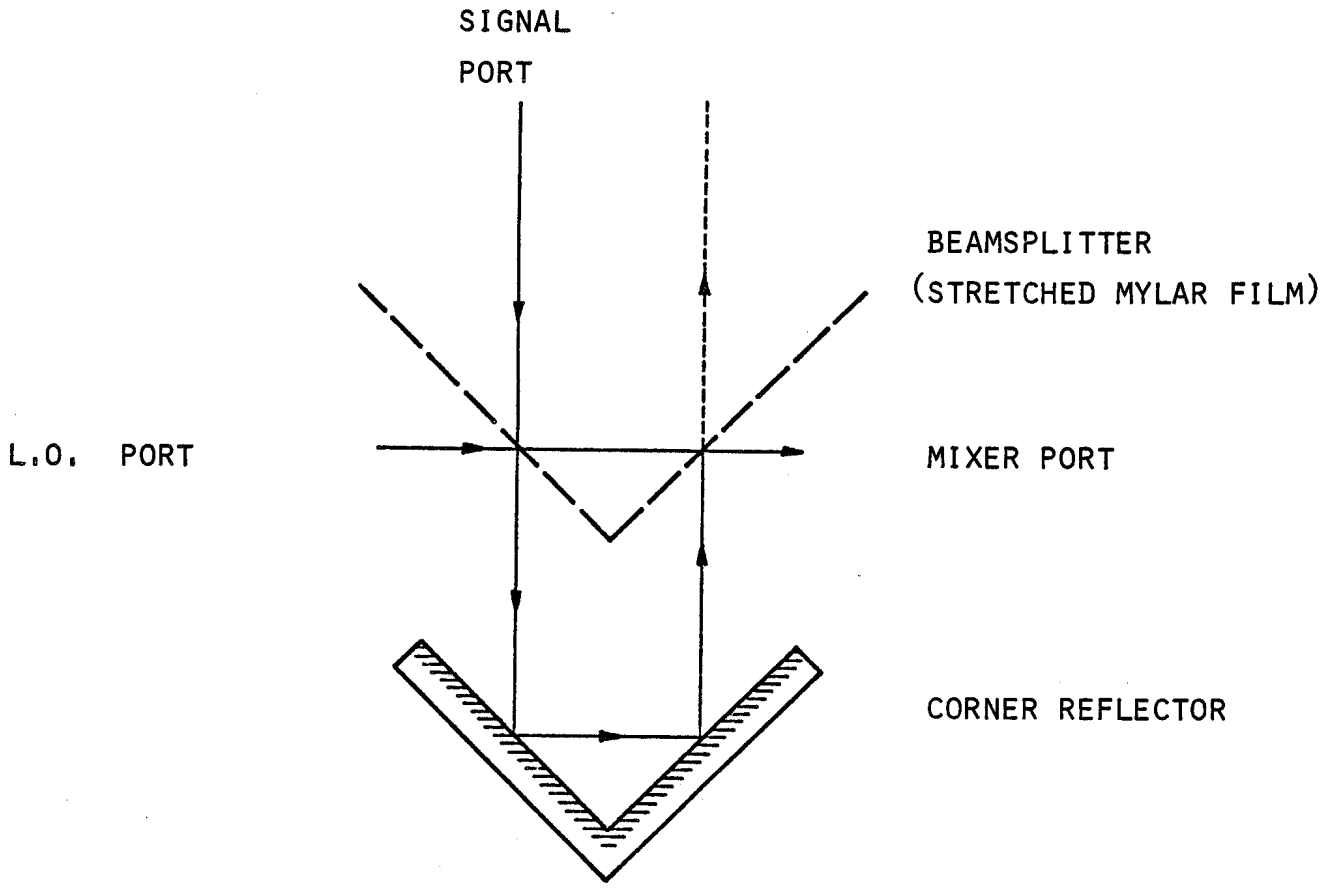

Figure 4.4.2 : Diplexer Comprising Corner Reflector and Two Beam Splitters

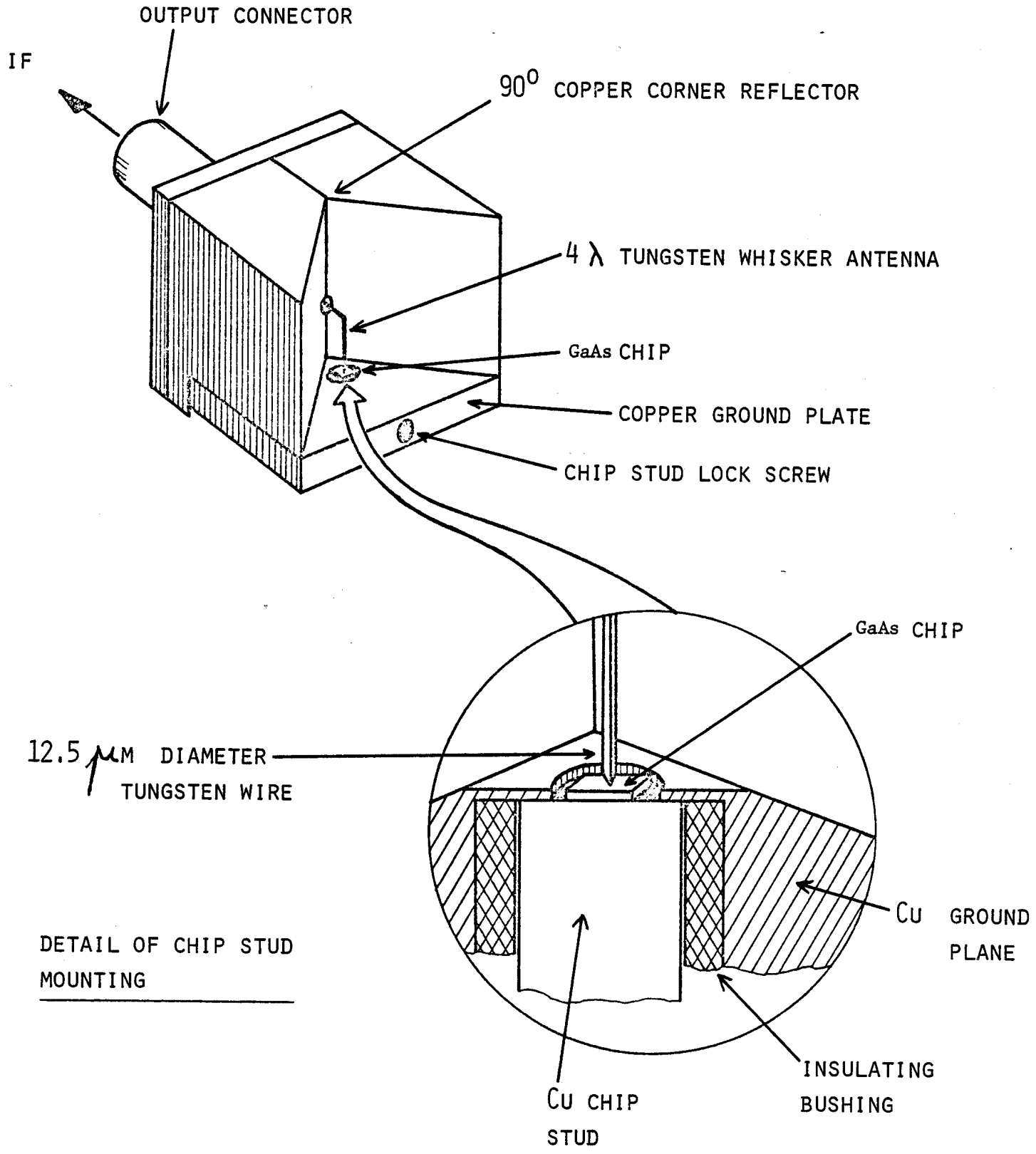

Figure 4.4.3 : Quasioptical Mixer

5. APPLICATION OF THE TECHNIQUE OF FIR-LASER SCATTERING TO MEASUREMENTS ON JET

In this section, we examine the applications of the technique of FIR-laser scattering to a study of JET, over a range of plasma conditions envisaged for the device.

The main topics investigated are: the power required from the laser, the restrictions imposed by limited access (in terms of collection angles), the achievable spatial resolution, the resolution in $\underline{k}$, the accuracy with which T_i can be determined, the effects of plasma impurities, the problems caused by refraction, the effects due to electron cyclotron and bremsstrahlung radiation and the complications due to plasma micro-turbulence.

In considering these topics we assess the situation for the three principal wavelengths of D_2O, viz. 66, 114 and 385 μm. Although we propose a scattering system based on 385 μm, since at present it represents the best achievable performance both in terms of laser and detector, the situation could conceivably change over the next few years. By considering the two other wavelengths, which are sufficiently different that together the three cover a useful range, we aim to illustrate the broader possibilities for FIR-laser scattering.

Finally, we summarise the conclusions reached and estimate the range of JET parameters over which we can obtain useful measurements.

5.1 Required Laser Power

We make use of equation 2.2.1 to calculate the laser power P_o necessary to obtain a scattered signal of power equal to the receiver NEP. The results are shown in Table 5.1.1 for detection bandwidths

of 1 and 2 GHz and assuming an f-number of 40 for the input focusing optics. To calculate the required laser power P_o for a receiver of a certain NEP, it is necessary to multiply the figures in the columns by that NEP.

Assuming an NEP of 3×10^{-19} WHz^{-1}, and for a bandwidth of 1 GHz, at 385 μm P_o varies between 9.3×10^5 W and 5.4×10^3 W for the conditions $n_e = 10^{13} cm^{-3}$, T = 1 keV and $n_e = 3 \times 10^{14} cm^{-3}$, T = 20 keV, respectively. None of the powers tabulated take into account the losses due to transmission of the incident and scattered laser beams through windows, inefficient coupling of the collected radiation into the detector and other losses. Taking these into account, the powers should be multiplied by a factor of at least ~ 5 to obtain the true laser power P_o needed.

It is clear that at densities below $\sim 3 \times 10^{13} cm^{-3}$, for a receiver of NEP = 3×10^{19} WHz^{-1}, a laser power of several MW will be necessary to achieve adequate scattered power. Consequently, a density of $\sim 10^{13} cm^{-3}$ probably represents the lower limit at which a scattering measurement could be performed, and an indication of T_i obtained, without recourse to a more energetic laser than that envisaged in section 3.1.

5.2 Access Requirements

In Table 5.2.1 we tabulate the scattering angles Θ required to accommodate detection bandwidths of 1 and 2 GHz, for the ranges of plasma parameters previously encountered. We see that, to cover all of the possibilities considered, angles between 77.0^o and 1.4^o would be required.

It is evident that at 66 μm the angles required at temperatures above a few keV are so small, 1.9^{o} at 10 keV for $\Delta\nu$ = 1 GHz, that stray light would pose a serious problem. Spatial resolution would also be compromised - as shown later. A bandwidth of 2 GHz is at present beyond the capabilities of the Ge : Ga mixer, without drastically increasing NEP, so 1 GHz probably represents an upper limit.

At 114 μm, the situation is much improved with measurements up to $\sim$ 10 keV feasible for $\Delta\nu$ = 1 GHz. Once again, the same restrictions apply to the Ge : Ga mixer as at 66 μm.

In an idealised situation, the best candidate would be the 385 μm line of D_2O. Angles of between 36^{o} and 16^{o} would cover the range of ion temperatures between 1 and 20 keV, with a judicious selection of detection bandwidth being made to maintain a value of α of between 1.2 and 3.6.

Unfortunately, on JET the arrangement of diagnostic ports is such that the ranges of angles that can be achieved are 0 - 18^{o} and 60 - 120^{o}. For the latter, it is necessary to use a window in one of the horizontal ports - these are very much in short supply. An angle of $\sim 11^{o}$ is needed to collect scattered radiation from the plasma mid-plane. Thus, at 385 μm the spectral width of the scattered spectrum would be less than $\sim$ 350 MHz at T_i = 1 keV and $\lesssim$ 700 MHz at 4 keV. This, in turn, places a stringent demand on the spectral purity of the FIR-laser emission and on the efficiency of the beam and viewing dumps in reducing the level of stray laser light. Taking 500 MHz as the minimum allowable spectral width, scattering measurements at 385 μm could not be performed with adequate precision at temperatures of $\lesssim$ 2 keV.

We will show later that for the 385 μm line of D_2O, and at the higher densities and temperatures envisaged in JET, the use of a viewing dump is essential to minimise the amount of electron cyclotron radiation received by the collection optics. This restricts the maximum scattering angle, when using a pair of vertical ports, to about 11^{o} as shown in figure 5.2.1. In this figure we show the arrangement of windows and dumps that we envisage for JET and the paths of the various

beams.

The laser beam enters the torus at the right-hand side of the upper port and is collected by a beam dump at the left-hand side of the lower port. A series of windows, which permits a spatial scan to be made, is arranged in the lower port for collecting the scattered radiation. On one tokamak discharge the detection system would receive radiation from a single window only. Each window faces the viewing dump which is located at the left-hand side of the upper port. In figure 5.2.2 we show the arrangement of windows and dumps in the covers for the slit ports. The diameter of the input window is 7 cm while that of the collection windows is 5 cm. The beam dump has an aperture of 12 cm and the viewing dump aperture is 10 cm.

Taking the equatorial plane as the zero level, the vertical heights at which the collection cones and the laser beam intersect are -28, -6, 20, 50, 86, 130 and 184 cm, which represents reasonable coverage across the upper half of the torus.

5.3 Spatial Resolution

The spatial resolution achievable (see section 2.2), $\ell = 2r/\sin\Theta$, is given in Table 5.3.1. We set the radius as defined by the diffraction-limited spot size or by the requirement that r is at least five wavelengths of the fluctuation being observed, whichever is the larger.

At 66 μm, the spatial resolution becomes unacceptable for temperatures much greater than $\sim$ 4 keV, for a bandwidth of 1 GHz - at 10 keV ℓ = 58 cm. As discussed in the previous section, greater bandwidths are currently unattainable using a Ge : Ga mixer. Using a wavelength of 114 μm, the spatial resolution seems adequate up to temperatures of 10 keV.

We see that at 385 μm, even at a temperature of 20 keV, which corresponds to an angle of 8^o for 1 GHz bandwidth, the spatial resolution is not worse than 20 cm. Increasing the angle to $\sim 11^o$, whilst permitting a larger spectral width to the scattered radiation, would improve the resolution to $\sim$ 10 cm.

5.4 Resolution in k

We consider the resolution in $\underline{k}_f$, or Θ, that is achievable for the ranges of parameters previously encountered. For focusing limited by diffraction effects the radius of the focused beam is given by $r = 0.635\ \lambda_o F$, as discussed in section 2.2, while for focusing limited by considerations of the fluctuation wavelength $r = 2.5\ \lambda_o/\sin(\Theta/2)$. The maximum solid angle for collection is $d\Omega = \lambda_o^2/\pi r^2$, which has a cone fullangle $\delta\Theta = 2\tan^{-1}(\sqrt{d\Omega/\pi})$. In the first type of focusing, $\delta\Theta = 2\tan^{-1}((\pi \cdot 0.635F)^{-1})$ which gives $\delta\Theta = 1.44^o$ for an f-40 focusing element. Thus, $\delta\Theta$ is independent of wavelength and Θ, while the ratio $\delta\Theta/\Theta$ depends on the value of Θ. In the second case, $\tan(\frac{\delta\Theta}{2}) = \sin(\Theta/2)/2.5\pi$. For both $\delta\Theta$ and Θ small, which is the situation in which the fluctuation wavelength sets the limit on r, $\delta\Theta/\Theta \sim 1/2.5\pi \sim 0.13$. Consequently, under certain conditions, the resolution achievable in Θ is independent of the laser wavelength and the value of Θ itself, for maximum possible collection solid angle. Naturally, $d\Omega$ can always be reduced, but only at the expense of the scattered power.

In Table 5.4.1 we give the values of $\delta\Theta/\Theta$, as a percentage, for conditions previously encountered. To a first approximation, $\delta\Theta/\Theta$ is $\sim$ 13%, except at λ_o = 385 μm and for a bandwidth of 2 GHz. For both Θ and $\delta\Theta$ small, $\delta k/k \sim \delta\Theta/\Theta$. Taking a simple point of view, since the ion temperature is related to the half-width of the power spectrum of scattered radiation (i.e. $T_i = \text{const.}k^2 v_i^2$), the imprecision in the value of T_i is $\delta T_i/T_i = 2\delta k/k \sim 2\delta\Theta/\Theta$. This implies that in almost all of the measurements at 66 and 114 μm there would be an error of at least 25% associated with any value of T_i obtained, for maximum possible collection solid angle. To reduce this error to less than

10%, the angle $\delta\Theta$ would have to be reduced by at least a factor of 2.5, resulting in a loss of light gathering power by more than a factor of 6 and necessitating an increase in laser power by the same amount.

A closer examination reveals that the situation is much better than suggested by the above consideration. Our approach is as follows: We consider a case in which cooperative scattering is observed at an angle Θ with collection angle $\delta\Theta$ in the plane of scattering, centred on Θ. We choose $\delta\Theta/\Theta = 0.44$ and $\delta k/k = 0.35$ - far larger spreads than those likely to be encountered in practice. The theoretical ion feature is calculated for the mean angle $\phi = \Theta$ with solid angle $\delta\Theta$. The next step is to consider the finite range of collection angles. We divide the solid angle into five intervals, each of magnitude $\alpha = \delta\Theta/5$ in the plane of scattering. We evaluate the ion feature for each of the five angles, $\phi = \Theta$, $\phi = \Theta \pm \alpha$ and $\phi = \Theta \pm 2\alpha$, with solid angle α. Finally, a composite spectrum is formed by adding together the individual intensities of the five spectra. The form of the composite spectrum obtained is then compared with that of the spectrum obtained with $\phi = \Theta$ and solid angle $\delta\Theta$.

Purely for illustrative clarity, we assume that scattering occurs under such conditions that the ion thermal feature is well approximated by a Gaussian

$$i(x) = \frac{h}{\sqrt{\pi}} \exp(-h^2x^2),$$

where x is the frequency shift in units of kv_i and h is chosen so that, for the mean angle $\phi = \Theta$, $i(1)/i(0) = 0.5$. The total scattered intensity is given by

$$I_s = \frac{2h}{\sqrt{\pi}} \int_0^\infty \exp(-h^2x^2)dx = 1.$$

Consider one half of the spectrum divided into 10 adjacent channels from x = 0 to x = 1.8, each of width $\delta x = 0.18$. The intensity in the n^{th} channel (n = 1 to 10) is given by (ignoring the spurious factor of 2)

$$I_n = \frac{2h}{\sqrt{\pi}} \int_{x_{n-1}}^{x_n} \exp(-h^2x^2)dx.$$

Changing the variable to hx = t, we express each integral as the difference of two integrals of type

$$\frac{2}{\sqrt{\pi}} \int_0^T \exp(-t^2)\, dt,$$

which is the error function and is well tabulated. In figure 5.4.1 we plot the values of I_n versus x for the mean angle $\phi = \Theta$, at the points $x = (x_n + x_{n-1})/2$.

The exercise is repeated using the four other angles in turn, $\phi = \Theta \pm \alpha$ and $\phi = \Theta \pm 2\alpha$. For each angle, the new value of h is given by $h \sin(\phi/2)/\sin(\Theta/2)$, so that $I_s = 1$. We evaluate, for each value of ϕ, the intensities I_n over the same range of x as previously considered. These are also plotted in figure 5.4.1. The ratios $\sin(\phi/2)/\sin(\Theta/2)$ are 1.16, 1.08, 1.00, 0.91 and 0.81 for the five angles in decreasing order of magnitude, respectively. The spread in the half widths comprises 35% of the mean. Clearly, the spectrum for $\phi = \Theta$ does not represent at all well the spectra for the extreme cases with $\phi = \Theta \pm 2\alpha$. One might conclude from this that any attempt to fit a theoretical spectrum, calculated for $\phi = \Theta$, to one obtained experimentally with a range of angles $\delta\Theta$ would result in an inaccurate value of T_i being determined. For the case in point, according to our earlier argument, the error in T_i should be $\sim 2\, \delta k/k \simeq 70\%$.

However, in a scattering measurement these five spectra would all be overlayed on the various channels. What is important in determining the error in T_i due to the range of collection angles is the departure of the resultant spectrum from that associated with the

mean angle $\phi = \Theta$. Hence, in figure 5.4.2 we plot the spectrum obtained by adding the contributions of the five spectra, for each channel. In addition, the spectrum evaluated for the mean angle is plotted. There is not much difference between the shapes or half widths of the two spectra - the difference in the latter comprises 3.6% of the half width of the spectrum for $\phi = \Theta$. This is almost a factor of 10 less than in the previous case.

Consequently, having experimentally determined a power spectrum with a scattering geometry employing a large range of collecting angles, it is not automatically the case that the value of T_i determined by fitting a theoretical spectrum which ignores this angular spread is highly inaccurate. In the example we have considered, the value of $\frac{\delta k}{k}$ is probably a factor of 2 or 3 greater than that which would be encountered in practice. Hence, the resultant errors in the values of T_i would be $\lesssim$ 4%, which would be considerably smaller than those arising from other sources. In any case, if the theoretical spectrum was calculated using the proper weighting for the range of angles employed, the errors could be reduced drastically to an insignificant level.

As a final comment, for the above argument to hold the scattering conditions should be chosen so that the ion feature is a bell-shaped profile or, at worst, is only slightly hollow. In the event of a pronounced ion-acoustic resonance, the spread in k would probably lead to large errors in any determination of T_i, owing to the sensitive dependence of the width and height of the feature on the parameter $\alpha = 1/k\lambda_D$. Also, in any study of plasma turbulence a large range of k is usually unacceptable since the scattered intensity is often highly dependent on k.

5.5 Results on the Determination of T_i from a Simulated Power Spectrum

In this section we present the results obtained using the Monto-Carlo simulation program described in section 4.3.2.

To investigate the influence of such parameters as pulse length, power, detection bandwidth, the number of channels and the concentration of impurities on the results, we first of all define a set of standard operating conditions - Table 5.5.1. The fact that a wavelength of 66 μm and a receiver bandwidth of 2 GHz were chosen is purely historical but not of great importance, since the results can be applied to other wavelengths by simple scaling. Unless otherwise stated, all results pertain to these standard conditions.

As previously described, section 4.3.2, the estimates of accuracy in the determination of T_i are based on the statistics of 31 fits of a theoretical power spectrum to one that is simulated. This number is at the lower limit for drawing relevant statistical conclusions. However, it is a good compromise between using an excessive amount of computing time and obtaining results which are statistically meaningless.

In what follows, results are presented in terms of three important parameters, which we will now define.

$\Delta\overline{T}_i(\%)$: deviation of the mean value of T_i, obtained from 31 simulations, from the true value, in %. Large values indicate a systematic error in the fitting procedure (e.g. when fitting impurity-free spectra to a simulated spectrum from a plasma with impurities) and, hence, an unsatisfactory answer.

$\pm \Delta T_i/T_i(\%)$: the expected accuracy, in %, of a single measurement of T_i (sample variance/true T_i). This is the main parameter to judge whether or not a single-shot measurement can be relied upon.

90% confidence interval of $T_i(\%)$: the 90% confidence interval of the variance of a sample, expressed in % of the true T_i. This is a measure of the confidence in the value of the calculated precision of T_i.

The effect of varying the laser power and pulse length, on the accuracy of T_i, can be seen in Table 5.5.2. In these simulations it is assumed that both T_e and n_e are already known, from elsewhere, with standard deviations of 10%. As can be seen, the accuracy improves significantly with increasing pulse-length, also with increased laser power.

As shown earlier, section 4.3.2, optimum results are obtained by running the laser at a power level such that the S/N at the mixer is 1 and obtaining as long a pulse as possible. However, it may be difficult to produce a FIR laser pulse of constant energy, irrespective of the pulse duration, within the timescale in which we are interested ($\sim$ 100 nsec - 10 μsec). The above result indicates that it is beneficial to run the laser above its optimum power level if extending the pulse duration proves difficult. From Table 5.5.2 we see that for a scattered power that is three times larger than the product of receiver NEP and bandwidth and a realistic pulse duration of 800 nsec, a precision of better than 10% in T_i is achievable.

In another series of computations the effects of the presence of impurities on the accuracy of the determination of T_i have been investigated. A mixture of impurities was chosen with the same proportions as identified in the DITE tokamak (58), viz. 0.35% of O^{8+}, 0.07% of Fe^{24+} and 0.035% of Cr^{22+} and Mo^{32+}, to give a z_{eff} of 2.03. The procedure did not converge if it was attempted to extract T_i by fitting to the whole part of a simulated spectrum , with no allowance

in the fitting routine for the presence of impurities, i.e. fitting using an impurity-free spectrum.

Rather than try to include the effects of impurities in the fitting routine, since it is considered unlikely that their concentration or charge would be accurately known in practice, the lower part of the spectrum was discarded and a fit was made to the remaining high-frequency part, of width 2 GHz minus the cut-off frequency F_ϕ, divided into N channels. We varied F_ϕ in an attempt to determine the best cut-off frequency. For each cut-off frequency 10 series of runs were performed, each series with 31 simulations, for various numbers of channels (viz. a series with 5, 6, 7, 8, 9, 10, 11, 12, 14 and 16 frequency channels). Within this range of numbers no statistical evidence was found for an optimum number of channels. Consequently, 10 was arbitrarily adopted as being the standard number of channels.

In Table 5.5.3 the dependence of the accuracy in the determination of T_i on the cut-off frequency is shown, for the case of 10 channels. However, the values of $\Delta\overline{T}_i$ showed large fluctuations from one series of 31 simulations to the next. Hence, for each cut-off frequency, the value of $\Delta\overline{T}_i$ given is the average for the 10 series of runs. While the statistical error $(\Delta T_i/T_i)$ seems to remain fairly constant for cut-off frequencies between 400 and 800 MHz, the systematic errors improve considerably with increasing cut-off frequency. Consequently, to avoid errors due to impurities in the determination of the deuterium ion temperature, when fitting an impurity-free power spectrum to the spectrum obtained from an impure plasma the spectral parts up to at least 600 MHz (and preferably up to 800 MHz) should not be included in the fitting process.

The main plasma impurity in our example is oxygen. It is reasonable to expect that lower cut-off frequencies can be used and a better spectral fit obtained if the fitting routine uses the power spectrum

calculated for a plasma containing the known concentration of oxygen. Calculations have shown that, for a cut-off frequency of 600 MHz, by including the effect of the oxygen a more accurate value of T_i is determined since, although $\Delta T_i/T_i$ remains at about 12%, the error $\Delta\overline{T}_i$ is reduced by more than a factor of 5. In principle, it is possible to use even lower cut-off frequencies.

The influence of the precision with which n_e and T_e can be independently measured on the achievable precision with which T_i can be determined is shown in figure 5.5.1. The results are for the case of an impurity-free fit to a spectrum with impurities, for a cut-off frequency of 800 MHz. It can be seen that the determination of T_i is insensitive to the precision of T_e and n_e up to values of 10%. Thereafter, the error in T_i increases approximately linearly with the errors in n_e and T_e. Hence, provided in JET the errors in n_e and T_e are no worse than 10%, with our present state of development in FIR technology we can say that the limitations to the achievable accuracy in the determination of T_i are due to the performance of the apparatus used for the scattering measurement.

In another series of runs we investigated the influence of the ratio T_i/T_e on the precision of an ion temperature measurement. We found that in the presence of impurities the precision is not much affected in the range of $0.8 < T_i/T_e < 2$. For values smaller than 0.8 the precision deteriorates rapidly. Without impurities, where the low frequency part of the spectrum is available for fitting, the precision varies with T_i/T_e. The best precision is obtained around $T_i = \frac{1}{2} T_e$ in this case.

The effect of varying α is shown in Table 5.5.4 for a laser wavelength of 385 μm. The error in the temperature measurement grows roughly linearly with α, from 13% at $\alpha = 1.5$ to 19% at $\alpha = 3$ for the conditions shown. The table also shows how the scattering angle Θ varies with α and how the detection bandwidth has to be adjusted. We also adjusted the laser power in such a way as to obtain a constant signal-to-noise ratio of one at the detector.

Finally a number of runs were undertaken where the simulated power spectrum was evaluated taking into account the finite range of collection angles employed - the principle was similar to that described in section 5.4 but the method was much more rigorous. A fit was made to the simulated spectrum using a theoretical spectrum evaluated for the mean angle and then using a theoretical spectrum which was evaluated for the full range of collection angles. There were no noticeable differences in the values of temperature derived using the two types of spectrum. This finding is in complete agreement with the conclusions of section 5.4.

5.6 Beam Refraction

The incident and scattered beams on their long paths through the plasma will suffer deviation due to refraction. This deviation increases linearly with electron density and as the square of the laser wavelength. Hence, there will be a displacement of the laser beam at its point of focus in the plasma and at the beam dump, and the scattered beam will be displaced at the collection window. We will examine these effects, concentrating on the 385 μm wavelength and a peak electron density of 3×10^{14} cm^{-3} since under these conditions the displacements will be the greatest.

Consider a plasma of circular cross-section, on which a beam travelling in the xy plane parallel to y is incident at a distance x_i from the y axis, figure 5.6.1(a). For small deviations, the path length through the plasma is close enough to $2y_o$ and the deviation is given by

$$\alpha_x = 2 \int_o^{y_o} \frac{\partial}{\partial x} \ell n\, n(x,y) dy \quad ,$$

where n is the refractive index of the plasma. Assuming that the plasma has circular symmetry, and taking the variable $r^2 = x^2 + y^2$, the above equation is transformed to give

$$\alpha_x = 2x_i \int_{x_i}^{a} \frac{1}{n(r)} \frac{dn(r)}{dr} \frac{dr}{\sqrt{r^2 - x_i^2}} \quad , \qquad 5.6.1$$

where a is the plasma radius at the toroidal position considered. The plasma refractive index is given by

$$n_e(r) = 1 - 8.97 \times 10^{-14} \lambda^2 n_e(r) \ ,$$

where λ is the laser wavelength in cm. According to recent predictions (59) the electron density profile in JET will have the form

$$n_e(r) = \hat{n}_e(1 - (\frac{r}{a})^8).$$

We solve equation 5.6.1 numerically to evaluate the deviations α_x for various electron densities, laser wavelengths and values of the impact parameter x_i/a. The method takes into account that the path through the plasma will be different to $2y_o$ because of curvature. In addition, the case of a plasma of elliptical cross-section - horizontal radius a and vertical radius b - is treated.

The largest displacements will be suffered by the main laser beam at the entrance to the beam dump, figure 5.6.1(b). If x_o, y_o are the coordinates of the beam at its point of exit from the plasma the beam displacement at the dump entrance will be

$$d = x_o - x_i + (\ell - y_o)\tan \alpha_x .$$

For JET, we take ℓ to be 350 cm, with a = 125 cm and b = 210 cm.

In figure 5.6.2 we plot d versus x_i/a, for the case of a circular and an elliptical cross-section, with $\hat{n}_e = 3 \times 10^{14}$ cm^{-3} and $\lambda = 385$ μm. As can be seen, for an impact parameter of ~ 0.9 the displacements are very large, over 42 cm in the case of a plasma that is elliptically shaped and over 29 cm for a plasma with a circular cross-section. The displacement decreases rapidly with decreasing impact parameter and for values of $x_i/a \lesssim 0.4$ we see that $d < 8$ cm. In table 5.6.1 we tabulate the peak values of d (for an impact parameter of 0.9) for the three wavelengths of D_2O and for various electron densities. Also tabulated are the beam deviations α_x after the laser beam has traversed the plasma. We see that at 385 μm, if the plasma density were increased from 3×10^{13} to 3×10^{14} cm^{-3} the beam displacement would increase by over 38 cm i.e. the beam dump would have to be moved by that amount to trap the main laser beam. This would cause problems.

However, because of the proposed scattering arrangement using a pair of vertical ports, figure 5.2.1, the impact parameter employed would be ~ 0.05. Even at 385 μm and a density of 3×10^{14} cm^{-3}, the maximum displacement of the laser beam at the dump would be less than 1 cm and could be safely ignored. Under the same conditions, the displacement of the scattered beam at the collection window is even less because the beam only traverses half of the plasma cross-section - the displacement would be $\lesssim 0.4$ cm, which is not serious. Finally, in the case of the laser beam being focused onto the plasma equatorial plane the worst possible displacement of the focal spot due to refraction would be $\lesssim 0.2$ cm.

5.7 Electron Cyclotron Emission and Bremsstrahlung

At the higher densities and temperatures envisaged for the operation of JET, at 385 μm the level of electron cyclotron emission becomes sufficiently high to dominate all other sources of noise associated with detection. Without the use of a viewing dump and if no advantage were taken of the polarisation characteristics of the radiation, the level of e.c.e. reaching the mixer could be so high that scattering measurements would be very difficult without a significant increase in the power of the FIR laser above the 1 MW level. For propagation at right angles to the plasma magnetic field there are two modes of emission, both linearly polarised. The extraordinary mode has the electric vector perpendicular to the magnetic field while the ordinary mode has the electric vector parallel to the field. Emission in the extraordinary mode dominates.

According to recent calculations (60) at temperatures up to 3 keV and for toroidal magnetic fields of less than 28 kG, the level of e.c.e. will be negligible at 800 GHz. However, for B = 34 kG, T_e = 10 keV and $n_e = 10^{14}$ cm^{-3} the emission levels are $P_e = 1.5 \times 10^{-13}$ W/cm^2/str/Hz and $P_o = 7.5 \times 10^{-14}$ W/cm^2/str/Hz for the extraordinary and ordinary mode, respectively. These values take into account the effects of reflections off the torus walls and of polarisation scrambling. Taking the maximum possible collection entendue - that set by the heterodyning condition, $\pi r^2 d\Omega \lesssim \lambda_o^2$ - the total power arriving at the mixer is $P_t = 3.3 \times 10^{-16}$ WHz^{-1}. This is a factor of 1000 higher than the achievable receiver NEP at 385 μm. Consulting Table 5.1.1, taking the above plasma parameters, for a bandwidth of 1 GHz and an NEP of 3.3×10^{-16} WHz^{-1}, the laser power required is 18.5MW. It is clear that this is unacceptable, and steps will have to be taken to reduce the level of e.c.e. at the mixer.

If reflections can be avoided, by using a viewing dump, then the emission is reduced and $P_e = 3 \times 10^{-14}$ W/cm^2/str/Hz whilst the power in the ordinary mode is negligible. Under these conditions, the laser power required to yield a scattered signal of the same power as the noise is $\sim$ 2.5 MW, which is still on the high side. However, taking advantage of the low emission in the ordinary mode, a scattering arrangement in which the laser beam was polarised with the electric vector perpendicular to that of the extraordinary mode would enable a polariser to be used in the detection system to discriminate against the e.c.e. Referring to figure 5.2.1, this would entail the laser beam being polarised perpendicular to the plane of scattering. Through the use of a polariser, one would expect to achieve an improvement of $\lesssim$ 10 in NEP.

Thus, for a laser wavelength of 385 μm the effects of e.c.e. will have to be taken into account in any scattering system designed for JET. With care, it should be possible to avoid the need for laser powers much in excess of 1 MW for all but the most extreme operating conditions. Owing to the uncertainties involved in the calculation of e.c.e. powers it is difficult to predict the upper limits of measurement - a tentative estimate would be $\sim$ 15 keV for a field of 34 kG and an electron density of $\sim 2 \times 10^{14}$ cm^{-3}.

Finally, the level of bremsstrahlung radiation has been calculated over the full ranges of plasma parameters for a z_{eff} of 2, using the expression (61)

$$P_b = 5.05 \times 10^{-48} g\, n_e \Sigma(n_i z^2).\ T_e^{-\frac{1}{2}} \exp(-4.14 \times 10^{-15} \nu/T_e)\ \text{W/cm}^3\text{/str/Hz},$$

where g is the Gaunt factor (set equal to 1) and ν is the frequency. We roughly estimate the plasma volume within the field of view to be a cylinder of length 420 cm and diameter 5 cm (equal to that of the collection window). The collection solid angle is set by the heterodyning condition and is $\sim 2.2 \times 10^{-4}$ str. Even for the extreme

conditions of $n_e = 3 \times 10^{14}$ cm^{-3} and $T_e = 1$ keV, $P_b = 1.0 \times 10^{-19}$ WHz^{-1} at 385 μm. It is not anticipated that this level of radiation will cause any problems.

5.8 The Effects Due to Plasma Micro-Turbulence

Probably the biggest unknown in any attempt to measure T_i by FIR-laser scattering is whether or not the presence of micro turbulence in the plasma will have any deleterious effects on the measurement. Because of electron density irregularities, δn_e, in a plasma, either random or coherent, a scattered intensity proportional to $(\delta n_e)^2$ is detected due to the bunched electrons emitting constructively. Suppose there exists a turbulence mechanism such that the fluctuation level $(\frac{\delta n_e}{n_e})_{tu}$ is a factor F larger than the thermal level $(\frac{\delta n_e}{n_e})_{th} \propto \frac{\sqrt{n_e}}{n_e}$. The intensity scattered from those turbulent fluctuations characterised by wave vector $\underline{k}$ and frequency ω will therefore be F^2 times the intensity scattered from thermal fluctuations of the same $\underline{k}$ and ω. Clearly, it does not require a level of micro turbulence of more than a few times the thermal level, in the $(\underline{k},\omega)$ regime in which we would attempt to measure T_i, before all information concerning the ion thermal motion would be lost against the intense background radiation scattered from the turbulent fluctuations.

Fortunately, the (k,ω) regime which characterises ion thermal motion appears to be one in which turbulence is rare. Assuming that the scattering parameter $\alpha = 1/k\lambda_D$ is chosen to be close to unity then the scale length for scattering, λ_f, is $\sim \lambda_D$. Furthermore, the frequencies ν_f of the thermal fluctuations which would be recorded lie in the range o.5 - 2 GHz, approximately. Although there is a paucity of experimental results on micro turbulence in tokamaks, up to date there have been no reports of turbulence of such

short wavelength and high frequency being observed. Recent studies (62,63) have indicated that the regime in which the most intense micro turbulence occurs is for wavelengths of $\sim 50\ \lambda_D$, or more, and frequencies of $\lesssim 1$ MHz. It has been observed in a FIR-scattering measurement (62) that the scattered intensity varies as $\omega^{-2.5}$ and $k^{-3.5}$ with

$$\left(\frac{\delta n_e}{n_e}\right)_{tu} \simeq 8 \times 10^4 \left(\frac{\delta n_e}{n_e}\right)_{th} \text{ for } \nu_f \lesssim 2 \times 10^5 \text{ Hz}$$

and $120\ \lambda_D \lesssim \lambda_f \lesssim 410\ \lambda_D$. Scaling from these results, for $\lambda_f \sim \lambda_D$ and $\nu_f \gtrsim 0.5$ GHz the level of micro turbulence would be negligible. However, even in the case of the studies reported in reference (63) the laser power employed was such that fluctuation levels a factor of 20 above the thermal level would have barely been detectable. Even this relatively-low level would, of course, be sufficient to completely ruin any attempt to measure T_i.

In conclusion, whilst there is no concrete evidence either way to determine whether or not micro turbulence will rule out measurements of T_i, on balance it appears that provided λ_f and ν_f are suitably chosen ($\sim \lambda_D$ and $\gtrsim 500$ MHz, respectively) there should be no problems in this respect. However, should it prove to be impossible to measure T_i the diagnostic would be a very useful tool with which to study plasma micro-turbulence.

5.9 Summary

We now summarise the main finding of this section and state the range of plasma parameters over which T_i could be measured using the proposed scattering system, together with its estimated performance.

To date, there has been insufficient work on micro turbulence in tokamak plasmas to be able to predict with certainty whether or not the turbulence level in JET will preclude any measurement of T_i. However, the accumulated results indicate that it is unlikely that such a measurement cannot be made. Impurities present in the plasma, with a z_{eff} of $\lesssim 2$, have little effect on the determination of T_i. The finite range of collection angles used has little influence on the accuracy of the measurement. An examination of beam refraction by the plasma has shown that, using the proposed scattering geometry, the effects are negligible - even at 385 μm. Bremsstrahlung radiation from the plasma should not, in any operating regime, present difficulties by becoming a dominant source of noise. Electron cyclotron emission will become the dominant noise source at the higher temperatures and magnetic fields envisaged for JET operation; this limits the maximum temperature at which measurements can be made.

Using a laser of wavelength 385 μm, of power 1 MW and pulse duration 1 μsec in conjunction with a receiver of NEP $\lesssim 3 \times 10^{-19}$ WHz^{-1}, from a computer simulation study it is estimated that T_i could be measured with an accuracy of at least $\pm$ 20% in the electron density range 3×10^{13} - 3×10^{14} cm^{-3} and in the temperature range 3 - 12 keV (assuming $T_e = T_i$). Without recourse to a more powerful laser, the lower limits for a useful measurement would be $\sim 10^{13}$ cm^{-3} and $\sim$ 2 keV while 15 keV probably represents the upper temperature limit. The spatial resolution achievable should never be worse than 20 cm, with an average separation between the points of measurement, across approximately half of the plasma diameter in the vertical direction, of $\sim$ 32 cm. If the CO_2 pump laser were multiply pulsed during one JET discharge, as discussed in section 3.2.5, several values of ion temperature could be obtained with a minimum time separation of $\sim$ 0.1 sec between successive measurements. Using a longer separation, $\gtrsim$ 1 sec, up to 10 successive measurements would be possible.

TABLE 5.1.1 Variation of Laser Power P_o with Laser Wavelength, Detection Bandwidth and Plasma Parameters

$n_e(cm^{-3})$	T(keV)	P_o/NEP for $\Delta\nu$ = 1 GHz				P_o/NEP for $\Delta\nu$ = 2 GHz			
		α	66μm	114μm	385μm	α	66μm	114μm	385μm
10^{13}	1	1.3	6.0×10^{24}	3.5×10^{24}	3.1×10^{24}	0.7	4.5×10^{25}	4.5×10^{25}	3.6×10^{25}
10^{13}	4	1.3	6.0×10^{24}	3.5×10^{24}	1.6×10^{24}	0.7	4.2×10^{25}	2.4×10^{25}	2.2×10^{25}
3×10^{13}	1	2.3	1.3×10^{24}	7.5×10^{23}	6.7×10^{23}	1.2	5.2×10^{24}	5.2×10^{24}	4.1×10^{24}
3×10^{13}	4	2.3	1.3×10^{24}	7.5×10^{23}	3.5×10^{23}	1.2	4.8×10^{24}	2.8×10^{24}	2.5×10^{24}
3×10^{13}	10	2.3	1.3×10^{24}	7.5×10^{23}	2.2×10^{23}	1.2	4.8×10^{24}	2.8×10^{24}	1.6×10^{24}
3×10^{13}	20	2.3	1.3×10^{24}	7.5×10^{23}	2.2×10^{23}	1.2	4.8×10^{24}	2.8×10^{24}	1.2×10^{24}
10^{14}	4	4.2	3.3×10^{23}	1.9×10^{23}	8.7×10^{22}	2.1	8.2×10^{23}	4.7×10^{23}	4.2×10^{23}
10^{14}	10	4.2	3.3×10^{23}	1.9×10^{23}	5.6×10^{22}	2.1	8.2×10^{23}	4.7×10^{23}	2.8×10^{23}
10^{14}	20	4.2	3.3×10^{23}	1.9×10^{23}	5.6×10^{22}	2.1	8.2×10^{23}	4.7×10^{23}	2.0×10^{23}
3×10^{14}	4	7.3	1.0×10^{23}	5.9×10^{22}	2.8×10^{22}	3.6	2.2×10^{23}	1.3×10^{23}	1.2×10^{23}
3×10^{14}	10	7.3	1.0×10^{23}	5.9×10^{22}	1.8×10^{22}	3.6	2.2×10^{23}	1.3×10^{23}	7.5×10^{22}
3×10^{14}	20	7.3	1.0×10^{23}	5.9×10^{22}	1.8×10^{22}	3.6	2.2×10^{23}	1.3×10^{23}	5.4×10^{22}

P_o is obtained by multiplying the figures in the columns by the detector NEP

TABLE 5.2.1 Variation of Scattering Angle θ with Laser Wavelength, Detection Bandwidth and Plasma Parameters

$n_e(cm^{-3})$	T(keV)	θ^o for $\Delta\nu$ = 1 GHz				θ^o for $\Delta\nu$ = 2 GHz			
		α	66μm	114μm	385μm	α	66μm	114μm	385μm
10^{13}	1	1.3	6.1	10.6	36.3	0.7	12.3	21.2	77.0
10^{13}	4	1.3	3.1	5.3	17.9	0.7	6.1	10.6	36.3
3×10^{13}	1	2.3	6.1	10.6	36.3	1.2	12.3	21.2	77.0
3×10^{13}	4	2.3	3.1	5.3	17.9	1.2	6.1	10.6	36.3
3×10^{13}	10	2.3	1.9	3.3	11.3	1.2	3.9	6.7	22.7
3×10^{13}	20	2.3	1.4	2.4	8.0	1.2	2.7	4.7	16.0
10^{14}	4	4.2	3.1	5.3	17.9	2.1	6.1	10.6	36.3
10^{14}	10	4.2	1.9	3.3	11.3	2.1	3.9	6.7	22.7
10^{14}	20	4.2	1.4	2.4	8.0	2.1	2.7	4.7	16.0
3×10^{14}	4	7.3	3.1	5.3	17.9	3.6	6.1	10.6	36.3
3×10^{14}	10	7.3	1.9	3.3	11.3	3.6	3.9	6.7	22.7
3×10^{14}	20	7.3	1.4	2.4	8.0	3.6	2.7	4.7	16.0

TABLE 5.3.1 Variation of Spatial Resolution ℓ with Laser Wavelength, Detection Band-width and Plasma Parameters

$n_e(cm^{-3})$	T(keV)	ℓ(cm) for $\Delta\nu$ = 1 GHz				ℓ(cm) for $\Delta\nu$ = 2 GHz			
		α	66μm	114μm	385μm	α	66μm	114μm	385μm
10^{13}	1	1.3	5.8	3.4	3.3	0.7	1.6	1.6	2.0
10^{13}	4	1.3	23.2	13.5	6.4	0.7	5.8	3.4	3.3
3×10^{13}	1	2.3	5.8	3.4	3.3	1.2	1.6	1.6	2.0
3×10^{13}	4	2.3	23.2	13.5	6.4	1.2	5.8	3.4	3.3
3×10^{13}	10	2.3	58.1	33.6	10.0	1.2	14.5	8.4	5.1
3×10^{13}	20	2.3	115.8	67.2	19.9	1.2	29.1	16.8	7.1
10^{14}	4	4.2	23.2	13.5	6.4	2.1	5.8	3.4	3.3
10^{14}	10	4.2	58.1	33.6	10.0	2.1	14.5	8.4	5.1
10^{14}	20	4.2	115.8	67.2	19.9	2.1	29.1	16.8	7.1
3×10^{14}	4	7.3	23.2	13.5	6.4	3.6	5.8	3.4	3.3
3×10^{14}	10	7.3	58.1	33.6	10.0	3.6	14.5	8.4	5.1
3×10^{14}	20	7.3	115.8	67.2	19.9	3.6	29.1	16.8	7.1

F = 40 assumed for f-number of focusing optics

TABLE 5.4.1 Relative Variation of Angle $\delta\theta$ of Collection Cone with Laser Wavelength, Detection Band-width and Plasma Parameters

$n_e(cm^{-3})$	T(keV)	$\delta\theta/\theta$(%) for $\Delta\nu$ = 1 GHz				$\delta\theta/\theta$(%) for $\Delta\nu$ = 2 GHz			
		α	66μm	114μm	385μm	α	66μm	114μm	385μm
10^{13}	1	1.3	12.7	12.7	4.0	0.7	11.7	6.8	1.9
10^{13}	4	1.3	12.7	12.7	8.0	0.7	12.7	12.7	4.0
3×10^{13}	1	2.3	12.7	12.7	4.0	1.2	11.7	6.8	1.9
3×10^{13}	4	2.3	12.7	12.7	8.0	1.2	12.7	12.7	4.0
3×10^{13}	10	2.3	12.7	12.7	12.7	1.2	12.7	12.7	6.3
3×10^{13}	20	2.3	12.7	12.7	12.7	1.2	12.7	12.7	9.0
10^{14}	4	4.2	12.7	12.7	8.0	2.1	12.7	12.7	4.0
10^{14}	10	4.2	12.7	12.7	12.7	2.1	12.7	12.7	6.3
10^{14}	20	4.2	12.7	12.7	12.7	2.1	12.7	12.7	9.0
3×10^{14}	4	7.3	12.7	12.7	8.0	3.6	12.7	12.7	4.0
3×10^{14}	10	7.3	12.7	12.7	12.7	3.6	12.7	12.7	6.3
3×10^{14}	20	7.3	12.7	12.7	12.7	3.6	12.7	12.7	9.0

TABLE 5.5.1 Standard Conditions for the Data Analysis Simulation Program

1.	Plasma	$n_e = 3.10^{13} cm^{-3}$, $T_e = T_i = 4$ keV, deuterium T_e and n_e accurately known
2.	Laser	$\lambda = 66$ μm, T(pulse duration) = 800 ns, power such that $P_S/P_N = 1$ in receiver
3.	Scattering geometry	$\Theta = 6.25^o$
4.	Detection	B = 2 GHz, 10 channels
5.	Statistics	31 simulations / run
6.	Correlation Parameters	$\alpha = 1.12$, $\beta = (T_e/T_i \cdot \frac{\alpha^2}{1+\alpha^2})^{\frac{1}{2}} = 0.75$
7.	Scaling	same results obtained if λ, Θ scaled according to $\lambda/\sin(\Theta/2) = \text{const}$

TABLE 5.5.2 The Effect of Variations in Pulse Length and Laser Power

S/N ratio P_S/P_N	Pulse length T (μsec)	$\Delta\bar{T}_i$ (%)	$\bar{+}\Delta T_i/T_i$ (%)	90% conf. int. of σ_{T_i} (%)
1	0.2	+3.9	34.9	28.9 - 44.4
1	0.8	-1.1	12.6	10.4 - 15.6
1	3.2	+1.4	11.1	9.2 - 14.2
3	0.2	+4.4	15.4	12.7 - 19.6
3	0.8	+1.5	9.0	7.4 - 11.5
3	3.2	-1.7	7.0	5.8 - 9.0

$$\frac{\Delta T_e}{T_e} = \frac{\Delta n_e}{n_e} = 0.1, \text{ otherwise standard conditions}$$

TABLE 5.5.3 Determination of the Cut-Off Frequency F_ϕ when Fitting Impurity-Free Spectra to the High Frequency Part of a Simulated Spectrum with the Impurities given in the Text

F_ϕ (MHz)	$\Delta\bar{T}_i$ *) (%)	$\bar{+}\ \Delta T_i/T_i$ (%)	90% conf. int. of σ_{T_i} (%)
400	- 8.7	13.9	11.5 - 17.7
600	- 3.1	12.3	10.2 - 17.7
700	- 3.0	14.7	12.2 - 18.7
800	- 1.4	13.9	11.5 - 17.7

Other conditions standard as defined in Table 5.5.1

*) Values in this column are averages of 10 runs with varying number of channels (viz 5 to 16 channels)

TABLE 5.5.4 The Effect of Variations in α

α	Θ	Detector Bandwidth (MHz)	Lower Cut-off Frequency (MHz)	Laser Power (MW)	$\pm\Delta T_i/T_i$ (%)	90% conf. int. of σ_{T_i} (%)
1.19	35^o	1930	800	1.34	14.1	11.7 - 17.9
1.38	30^o	1660	650	0.84	12.1	10.0 - 15.4
1.65	25^o	1390	600	0.50	12.6	10.5 - 16.1
2.05	20^o	1120	500	0.28	15.6	12.9 - 19.8
2.63	15.6^o	872	350	0.15	17.8	14.8 - 22.7
3.28	12.5^o	700	280	0.09	18.7	15.5 - 23.8

λ = 385 μm; $\frac{\Delta T_e}{T_e} = \frac{\Delta n_e}{n_e} = 0.1$, otherwise standard conditions

Detector NEP = 3×10^{-19} WHz^{-1}, f - 80 focusing optics

TABLE 5.6.1 Variation of Beam Displacement d and Deviation α_x with Laser Wavelength and Plasma Electron Density

$n_e(cm^{-3})$	$\lambda(\mu m)$	d(cm)	α_x(millirads)
3×10^{13}	66	0.13	0.37
10^{14}	66	0.42	1.22
3×10^{14}	66	1.25	3.67
3×10^{13}	114	0.38	1.10
10^{14}	114	1.25	3.65
3×10^{14}	114	3.86	10.91
3×10^{13}	385	4.43	12.63
10^{14}	385	14.61	41.13
3×10^{14}	385	42.58	116.2

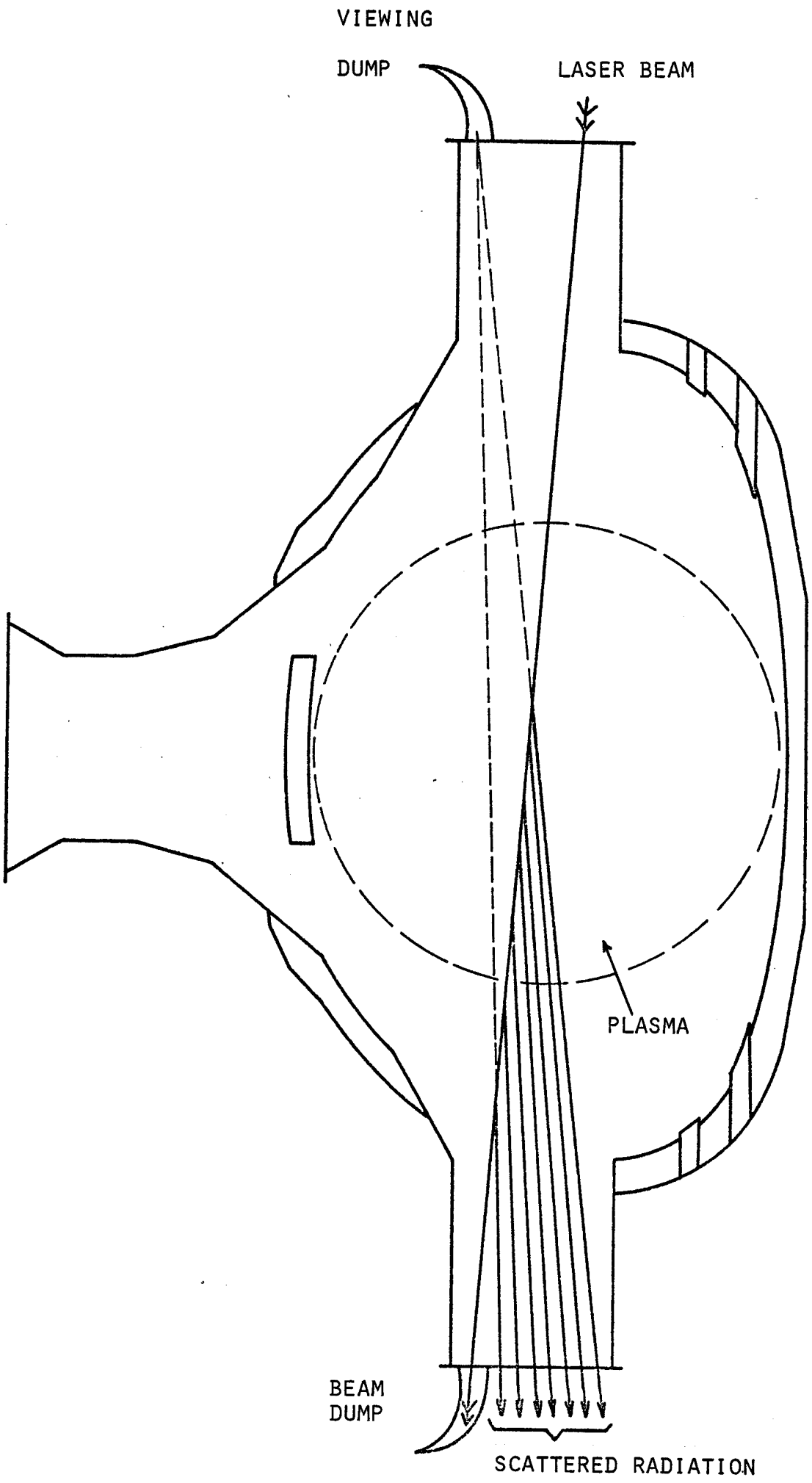

Fig. 5.2.1 : Arrangement of Incident and Scattered Beams in JET

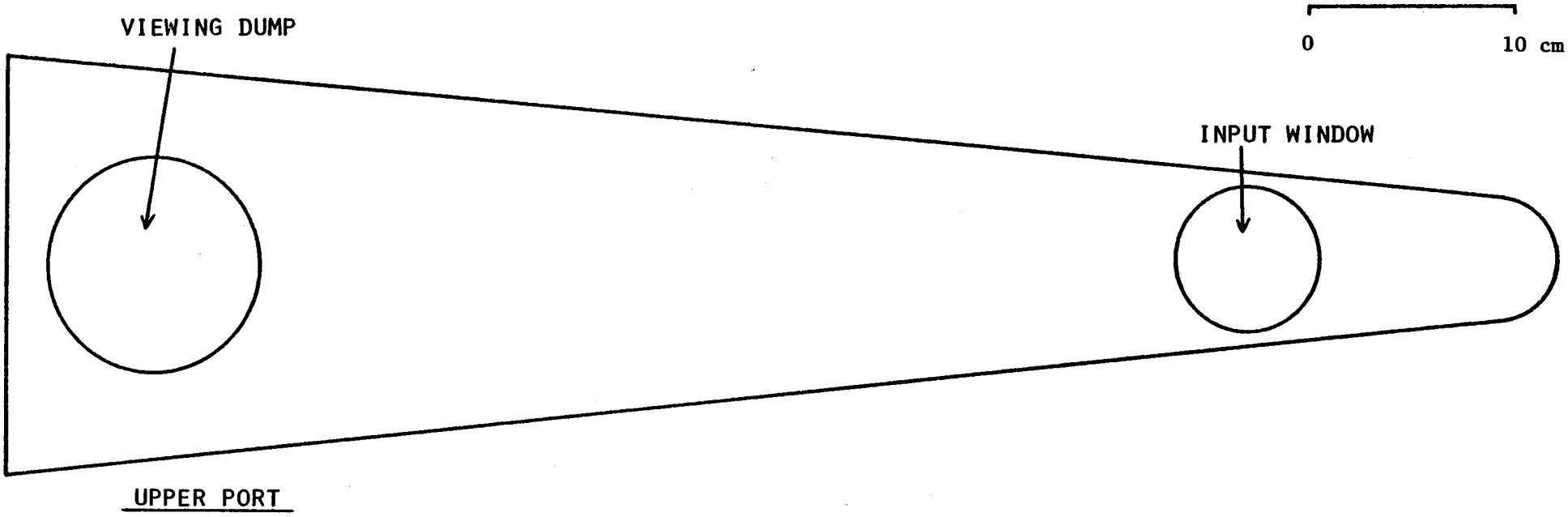

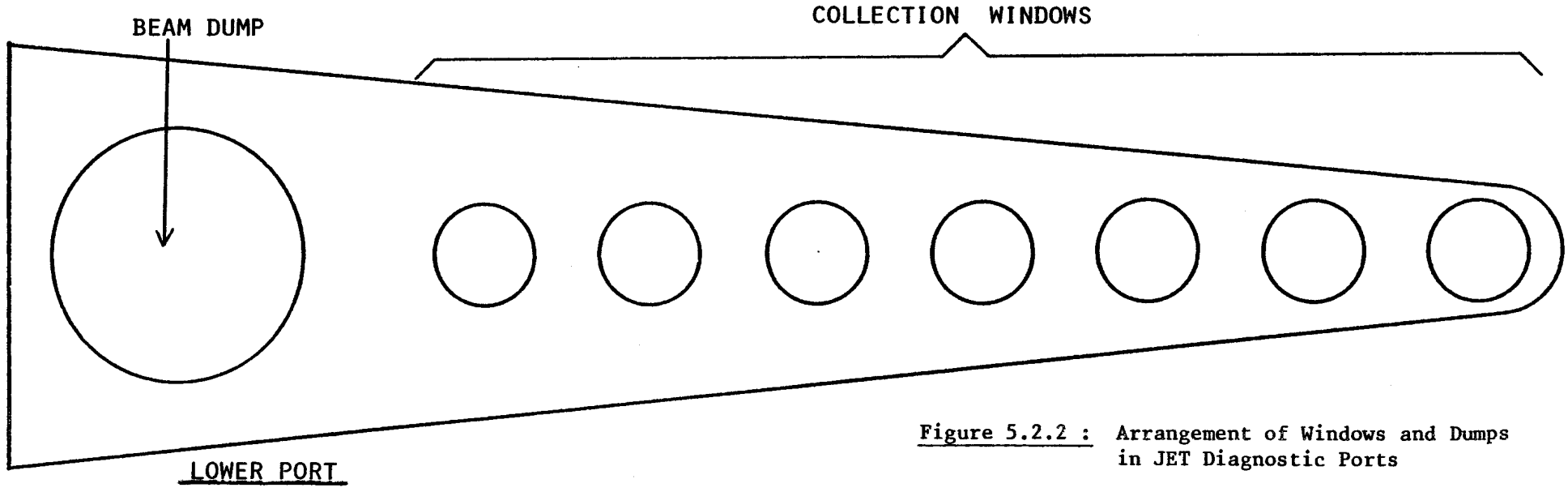

Figure 5.2.2 : Arrangement of Windows and Dumps in JET Diagnostic Ports

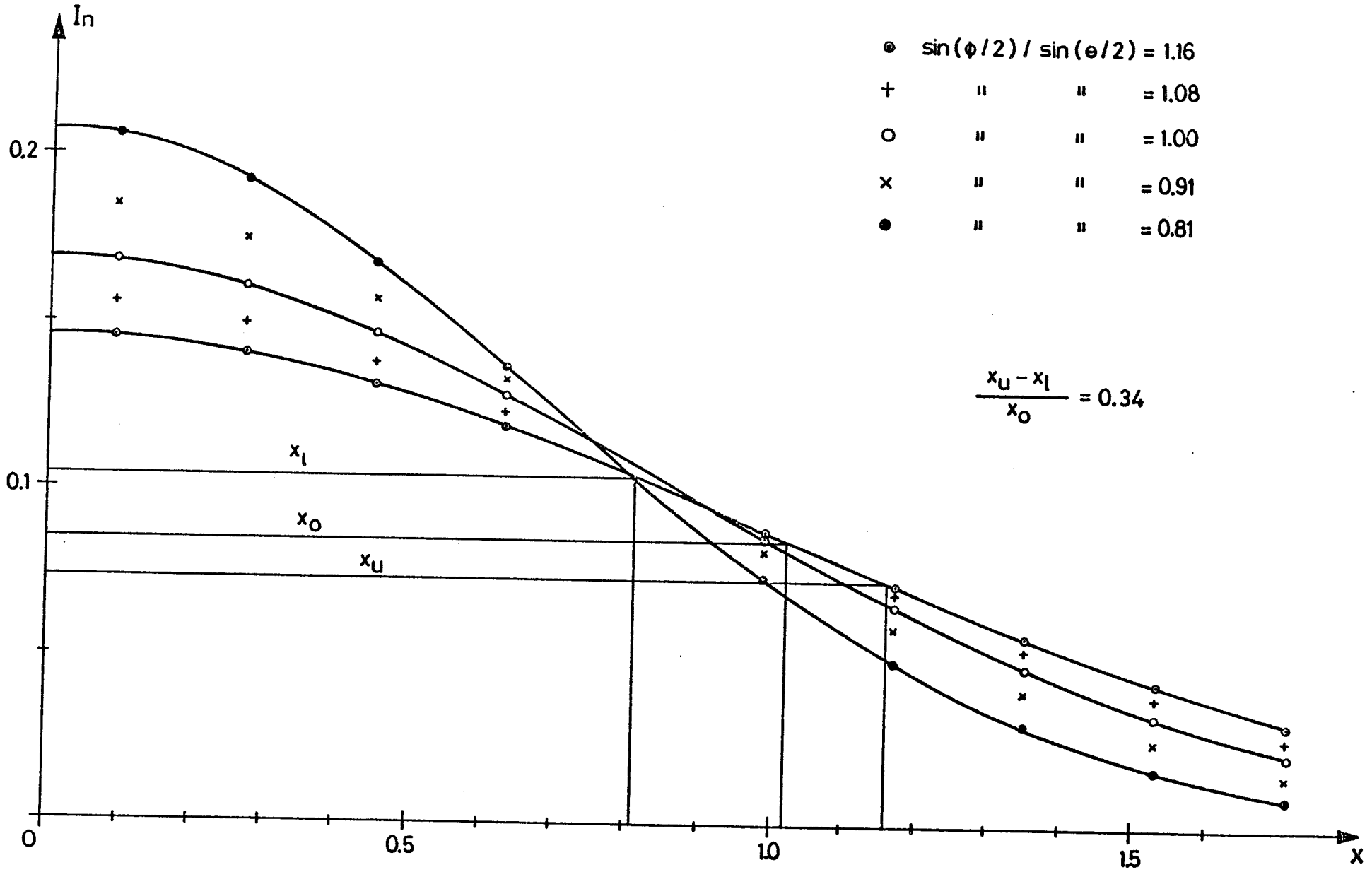

Figure 5.4.1 : Variation of Ion Feature with Angle within Collection Cone

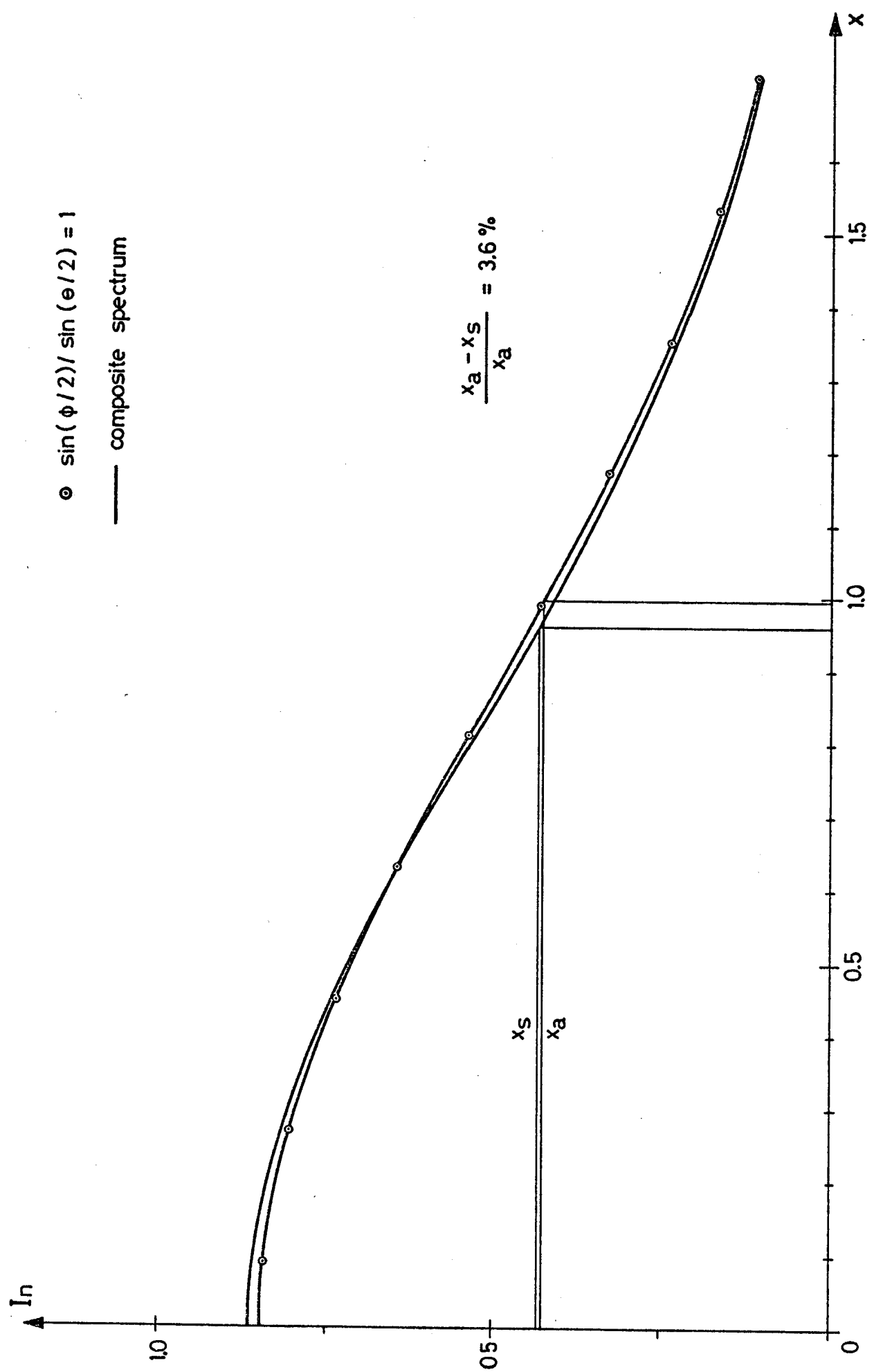

Figure 5.4.2 : Ion Feature Averaged over Collection Cone and Feature for Average Angle

Figure 5.5.1 : Variation of Accuracy of T_i with Precision in n_e and T_e

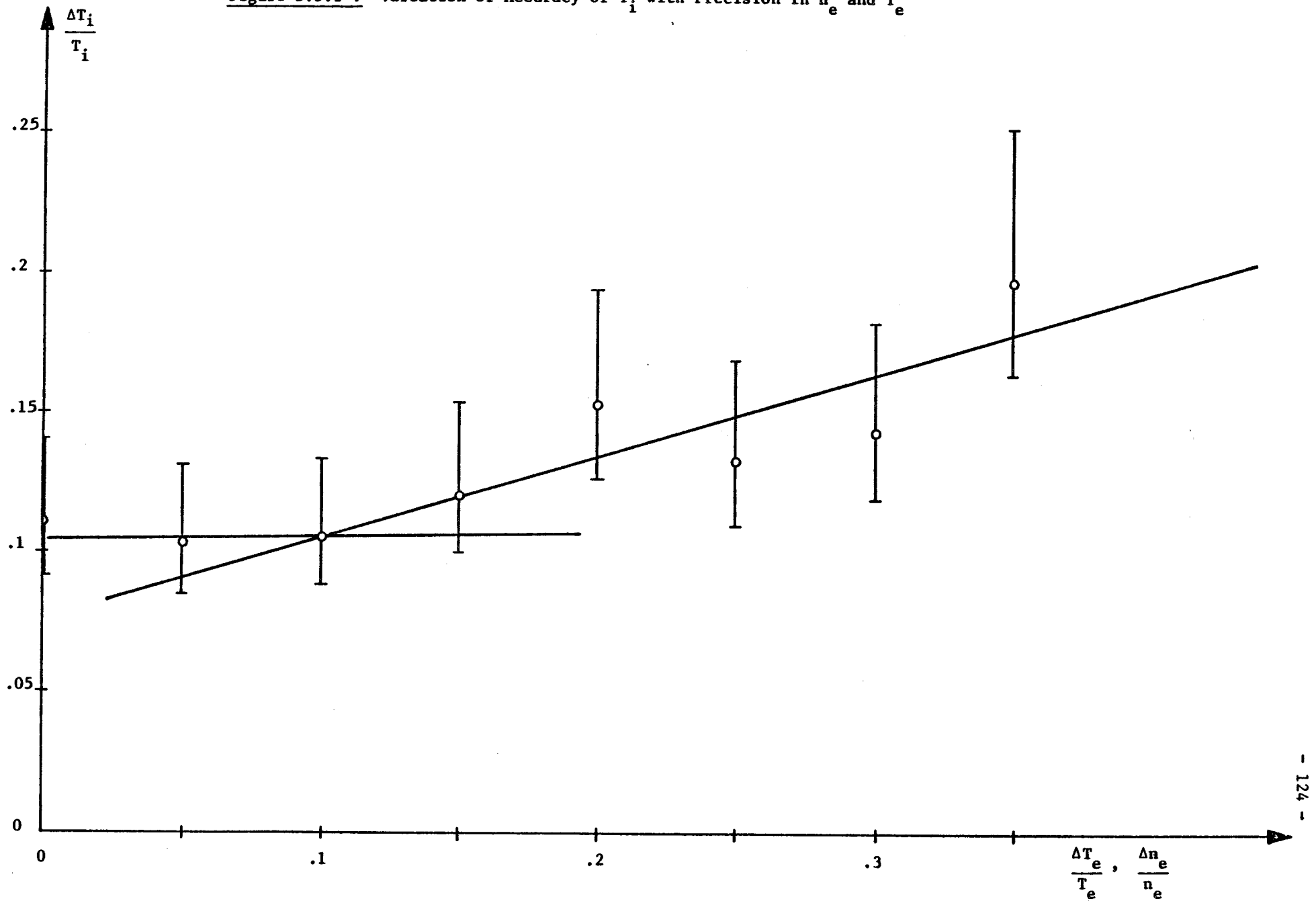

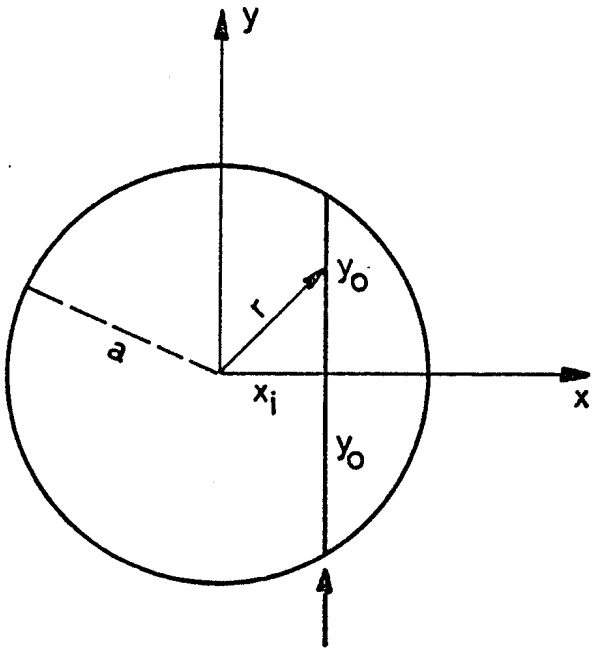

(a)

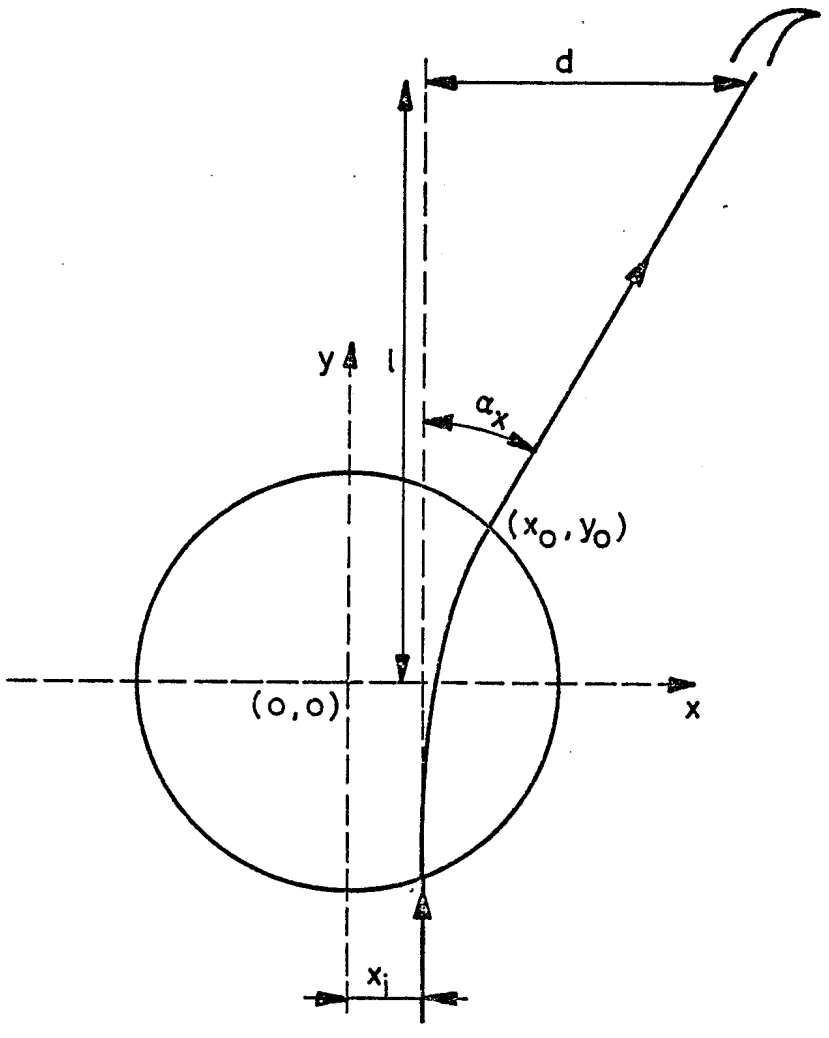

(b)

Figure 5.6.1 : Coordinate Systems Used for Calculating Refractive Deviations and Displacements

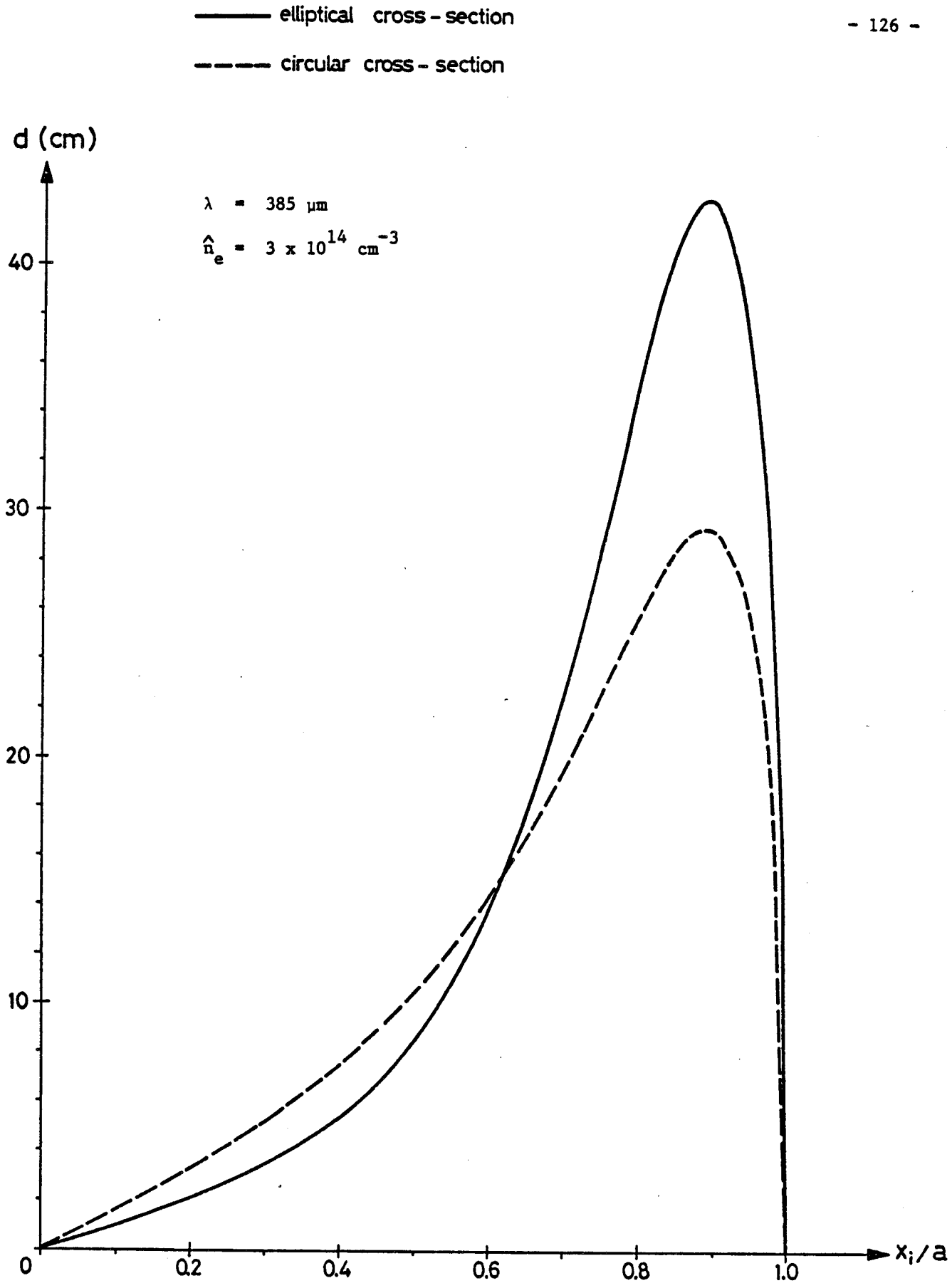

Figure 5.6.2 : Variation of Laser Beam Displacement at Dump with Impact Parameter

6. SOME PRACTIAL DETAILS

In this section we examine the practical requirements of interfacing the FIR-laser scattering diagnostic with JET. Among the topics considered are the construction of the windows and dumps, the geometries of the incident and scattered radiation, the siting of the equipment, the space it requires, and data acquisition and control. It is intended that the diagnostic will be suitable for use during the D-T phase of operation of JET. Consequently, the philosophy of the design study has been that from the outset the system should be capable of being operated fully by remote control. During the non-active phase any weaknesses of the system should manifest themselves - having corrected these, high reliability should have been achieved by the start of operation with D-T.

Since the diagnostic technique has yet to be proven, we have not concerned ourselves in providing detailed designs of, e.g., the layout of the optical components or a means of checking the alignment, but have adopted a more general approach. Also, we have not studied in detail a number of specific problems such as that of obtaining good seals for the windows and the effects of the radiation emitted by the plasma on the various components in the torus hall. Indeed, even in the case of the routine diagnostics for JET many of these problems remain an open question, but will have to be overcome before operation on the tokamak is possible. Consequently, we plan to capitalise on the time and effort invested by other groups, working on more fundamental diagnostics, in finding answers to these problems and to adopt the same solutions whenever possible - during which time we will be developing and testing our diagnostic on the Lausanne TCA tokamak (64) and establishing the ranges of parameters over which the technique is viable. This not only avoids the duplication of effort but also has the advantage of standardisation, with the attendant benefits for servicing and replacement.

6.1 Windows and Dumps

In section 5.2, we have discussed the proposed arrangement of the windows and dumps. The most suitable window material for our purposes is crystalline quartz, z-cut so that the incident and scattered laser radiation propagates through it in the extraordinary mode. This ensures minimum absorption. At 385 μm, for the extraordinary ray, quartz has a refractive index of 2.156 and an absorption coefficient of 0.1 cm^{-1} (65). The window thickness t needed to withstand a certain pressure p is related to the diameter d by $t/d = 4(p/M)^{\frac{1}{2}}$, where M is the mechanical strength coefficient. Taking M as 6.6×10^8 Nm^{-2} (66) and for a pressure differential of 1 atmosphere, the 70 mm input window should have a thickness of 3.5 mm whilst that of the 50 mm collection windows should be 2.5 mm. These thicknesses incorporate a safety margin of 4. We find that, for one window of each type in series, the transmission through the pair is $\sim$ 53%. In other words, at 385 μm, we would need to double the laser powers from those given in table 5.1.1 to overcome the losses introduced by reflections from, and absorption in, the input and collection windows.

At present, there is no completely satisfactory method for producing quartz-to-metal seals - necessary for mounting the windows in the port covers - although encouraging results have recently been obtained by a company in Princeton (67). By the time JET is operational it is anticipated that this problem will have been completely overcome.

The beam and viewing dumps will be made from pyrex glass, which has an absorption coefficient of $\gtrsim$ 50 cm^{-1} at 385 μm (68). Since electron cyclotron emission appears to pose a problem at the more extreme operating conditions of JET, as discussed in section 5.7, the viewing dump must be such that its efficiency is not dependent on the polarisation of the radiation incident on it. This criterion is satisfied by a Rayleigh horn. To avoid any risks of fracture due to stressing the glass during the bakeout of the torus, the horn should not be subjected to any

pressure differentials. This can be achieved by attaching a vacuum-tight enclosure of stainless steel to the torus, the horn forming a lining to the enclosure.

For the main laser beam, since the plane of polarisation is well defined we may use a dump that comprises three plates of pyrex glass aligned at Brewster's angle with respect to the beam, as depicted in figure 6.1.1. The beam falls onto the first plate where most of the radiation is absorbed. The small fraction which is reflected is incident on the second plate, and so on. By placing a fused quartz window behind the first plate, we may use a He-Ne laser to check alignment of the input optics and observe the beam as it leaves the dump.

It will be necessary to protect the windows and dumps from the debris produced during a discharge. To this end, moveable shutters will be strategically placed to protect these components. The shutters will be synchronised to open prior to the laser pulse, for a few seconds. It is envisaged using a device similar to that proposed for use with the ruby-laser scattering diagnostic (No 8.2).

6.2 Beam Paths and Alignment

The arrangement of the beam paths at the tokamak for the incident and scattered radiation is depicted in figure 6.2.1., together with details of the optical elements used.

Both the main laser beam and the beam of scattered radiation would have to traverse a minimum distance of $\sim$ 25 m between the torus and the diagnostics area, situated beyond the biological screen, in which the laser and detector would be housed. This requires many optical elements in each path to guide the beam around obstacles it encounters.

From Gaussian beam theory (69), we have found that at 385 μm free-space propagation of the TEM_{oo} mode over distances of many tens of metres is possible without undue losses due to diffraction, so that we are not obliged to use waveguides. We note that should another FIR wavelength be used on JET it might be necessary, depending on the laser transition, to propagate the beams in an environment of N_2 or dry air, to avoid excessive absorption by water vapour in the atmosphere (the 66 μm line of D_2O is an example of such a wavelength). This may be achieved by enclosing the beam paths by means of plastic tubing and flowing a suitable gas through it.

We intend using reflective optics entirely, to avoid the losses due to absorption and surface reflections associated with refractive elements. Also, because such optics are non dispersive we may use an optical laser for their precise alignment without introducing any errors for the FIR-laser radiation. For both the input and collection optics the focusing elements consist of a concave and convex mirror arranged to form an off-axis Cassegrainian telescope. The overall spherical aberration of each telescope is small, since the aberrations of the two mirrors are of opposite sign and largely cancel one another. Focusing changes can be readily accomplished by relatively-small variations of the separation of the two mirrors.

Returning to figure 6.2.1, the input optics comprise a concave mirror of 750 cm radius of curvature, a convex mirror of 560 cm radius of curvature and a plane mirror to direct the beam into the torus. The centres of curvature of the spherical mirrors coincide. The longitudinal spherical aberration for a parallel beam of diameter 12.5 cm, incident on the concave mirror, is about 6 mm, which is acceptable. If the separation between the two curved mirrors is increased by 40 cm the focal length of the telescope is reduced by 245 cm. This range of focusing is adequate to cover all of the plasma cross-section that is accessible to the collection windows, as discussed in section 5.2. It

is intended to mount the input optics on a small frame which is attached directly onto the input port structure. During a normal discharge it has been estimated that this structure would move by $\sim$ 0.04 mm, which should not cause any problems due to changes in alignment.

The collection optics are very similar to the input optics but perform the reverse role - that of providing a collimated beam. The focal lengths of the telescope mirrors are + 200 and - 100 cm. To select the appropriate collection window, the corresponding plane mirror in an array would be moved into position to direct the radiation into the telescope. Aberrations in this instrument would introduce an additional divergence of about 0.9 millirads. The collection optics would be mounted on a frame bolted to the floor of the torus pit.

For remote manipulation and monitoring of the positions of the mirrors and other elements it is proposed to use, if possible, the air-driven stepping motors and position sensors under development for the interferometer of Véron.

A satisfactory method of aligning the system remotely has not yet been devised. As previously mentioned, the all reflective optics enable a He-Ne or an Argon-ion laser to be used for this purpose. When monitoring the beam position and profile at various locations during alignment, it is intended to use bundles of fibre optics to relay this information to the operator outside the biological shield. At each end of a bundle, the fibres are arranged to form a rectangular grid with a spacing of a few mm. There would be a 1 : 1 correspondence between the fibres at each end so that any light pattern incident at one end of a bundle would be reproduced at the other. One of the grids mounted on the optical systems at the torus would be moved into a predetermined position to intercept the alignment beam. The pattern produced would be examined by the operator and any necessary adjustment

of the optical elements made. This process would be repeated along the chain until the whole system was in a state of good adjustment. Eventually, the procedure could be computer controlled so that checking and optimisation of alignment would be performed automatically before each tokamak discharge.

The checking and optimisation of the input and collection optics would be facilitated if an alignment target could be introduced into the torus from time to time. It is envisaged that a probe similar to that intended for use with the ruby-laser scattering diagnostic (No 8.2) would suffice. The probe would normally be housed in its own vacuum chamber, separated from the torus by a valve.

At present there is insufficient information available concerning the degradation of the transmission of quartz windows and fibre-optic cables due to irradiation by neutrons and γ-rays, which will be produced in copious amounts during the D-T phase of operation of JET. Although it is intended to use a radiation-resistant fibre-optic cable which has a relatively low performance, such as Du Pont Pifax S-120 types 30 and 40c, and even though a decrease in transmission by a factor of 10 could be tolerated, it is possible that radiation shielding will be needed for the cables.

6.3 Space Requirements

It is planned to locate the lasers and detection system behind the biological screen at a distance of $\gtrsim$ 25 cm from the torus. Since octant 4 has been provisionally allocated for the diagnostic, the equipment would be housed in the area primarily designated for additional heating and for tests.

The equipment would weigh approximately 15 tonnes and would occupy a total floor area of about 28 m^2. When arranged so as to afford reasonable access, an area of at least 45 m^2 would be needed. A minimum headroom of 350 cm is required. In addition, a screened room of area 400 x 300 cm and height 250 cm would be needed to house the detection system - or the equivalent space in a larger room would be suitable.

6.4 Data Acquisition and Control

The data acquisition and control requirements are listed in appendix 6.4.1. To monitor the state or performance of the various equipment we would need 63 channels. In addition, to control this equipment an additional 64 channels would be needed. For data aquisition purposes - where we have selected a detection system which has the largest requirements, to illustrate the worst case - 33 channels would be needed to transfer the data from the three transient digitisers to the local computer. Also, it is envisaged that 3 extra channels of each kind would be required as spares. Finally, for a single laser pulse 12,300 10-bit words of memory would be needed on the local computer.

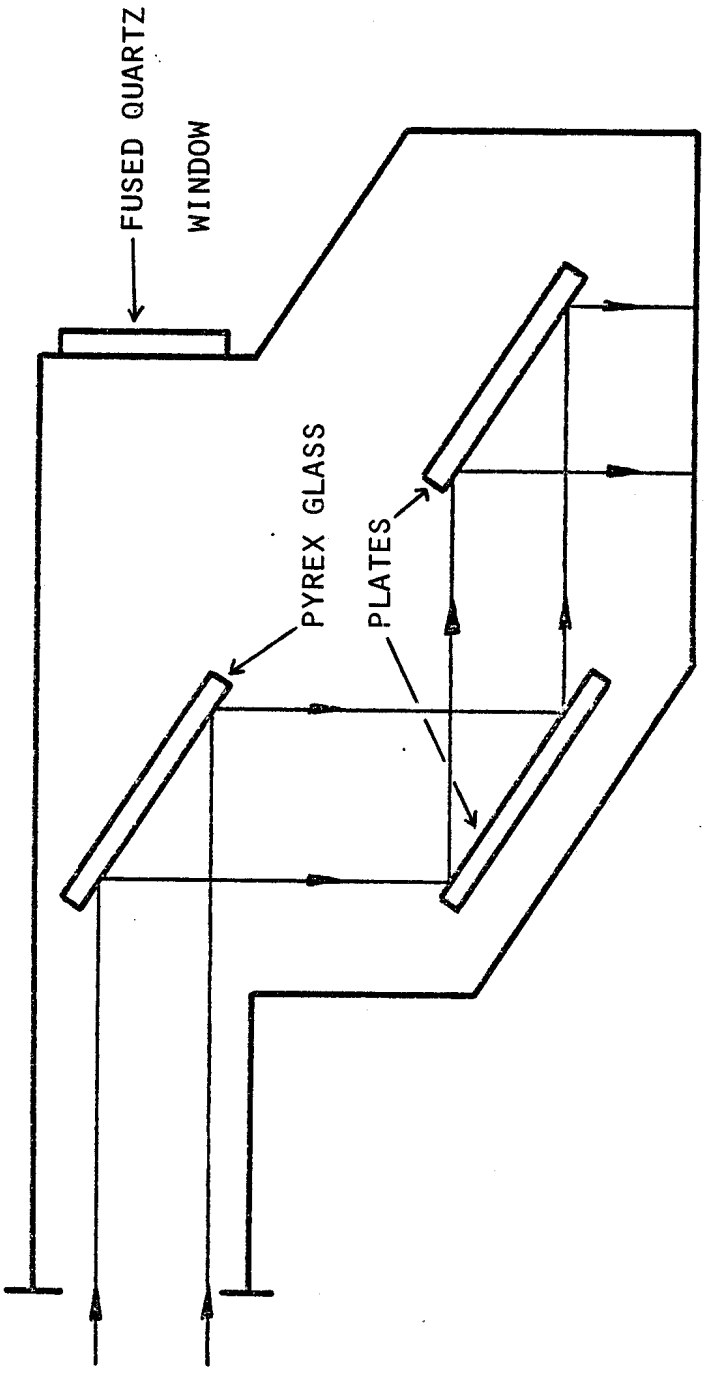

Figure 6.1.1 : Laser Beam Dump

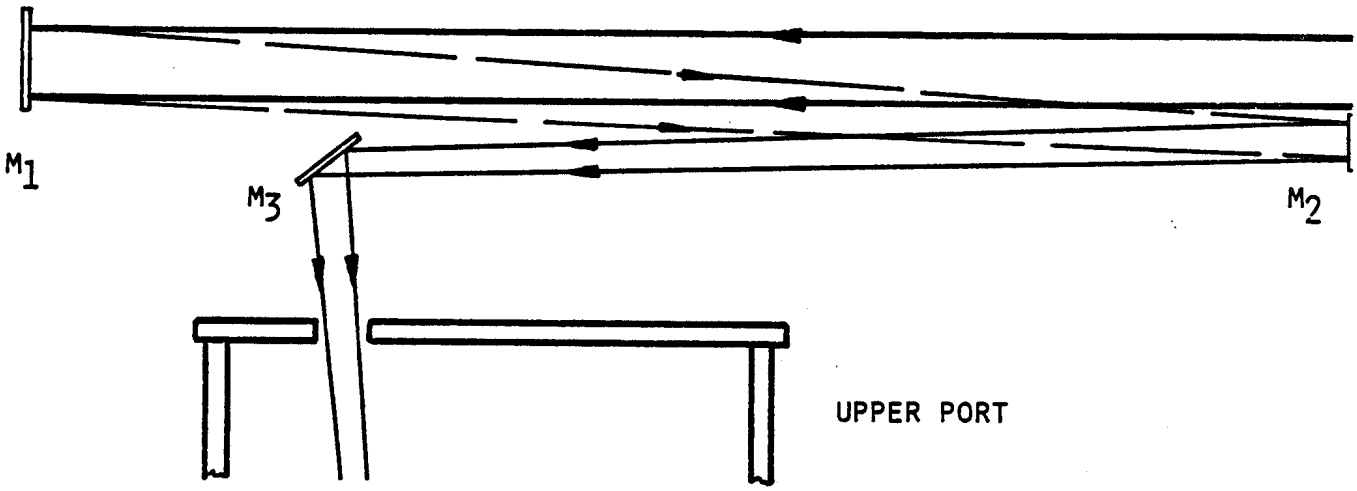

INPUT OPTICS

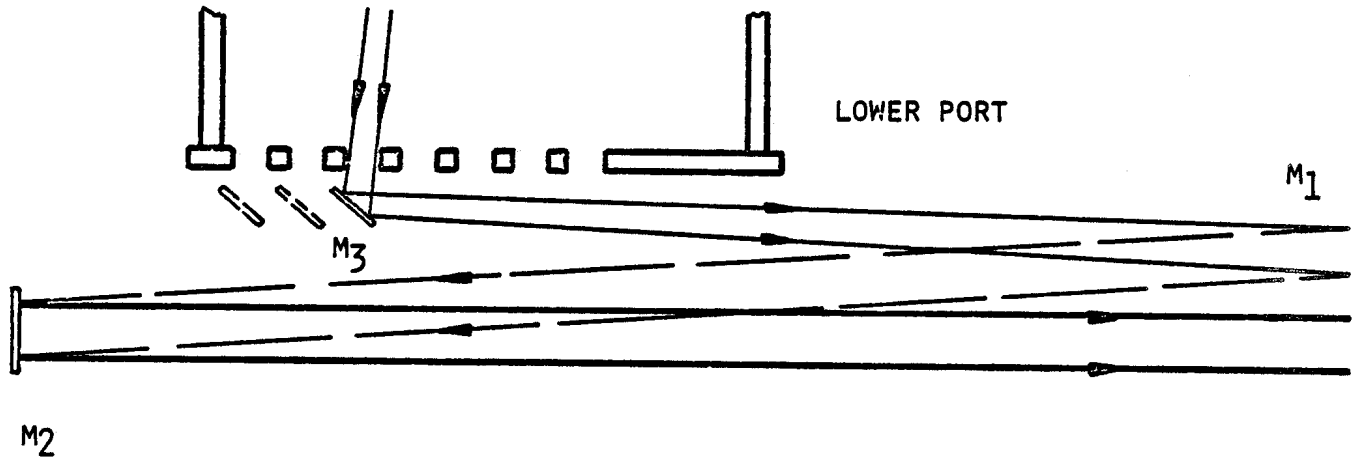

COLLECTION OPTICS

M_1 - CONCAVE MIRROR

M_2 - CONVEX MIRROR

M_3 - PLANE MIRROR(S)

Figure 6.2.1 : Arrangement of Input and Collection Optics

Appendix 6.4.1

MONITORING, CONTROL AND DATA ACQUISITION REQUIREMENTS

Monitoring (Analogue Signals)

Device(s)	Parameter	Digitising Time Interval	No of Channels
4 CO_2 Lasers	Current I(t)	10 nsec	4
"	Voltage V(t)	10 nsec	4
"	Photon Flux $\emptyset$ (t)	2 nsec	4
"	Photon Energy E	1 integrated value	4
E-Beam Laser	Electron Gun Vacuum	1 sec (cont.reading)	1
5 Power Supplies	Charging Voltage	"	5
"	Dumps down	"	5
FIR Laser	Photon Flux $\emptyset$ (t)	2 nsec	2
"	Photon Energy E	1 integrated value	2
"	Gas Pressure	1 sec (cont.reading)	2
Telescopes and Mirrors	Position and/or Orientation	"	30
Spare			3
			66

Controls

Device(s)	Control	No of Channels
5 Charging Units	Switch on	5
"	Dump	5
"	Increase Set Voltage	5
"	Decrease Set Voltage	5
4 CO_2 Lasers	Trigger	4
2 Vacuum Pumps	Switch on	2
2 "	Switch off	2
3 Transient Digitisers	Reset	3
"	Gate	3
Telescopes and Mirrors	Position and/or Orientation	30
Spare		3
		67

Appendix 6.4.1 (cont.)

DATA TRANSFER

Each of the three transient digitisers outputs ten-bit words, the bits in parallel. This requires 30 data channels. In addition, 3 control channels would be required. Allowing for 3 spare channels, this makes a total of 36 channels.

MEMORY ALLOCATION

Each of the three transient digitisers would output 4096 ten-bit words to the local mini-computer. A total of 12,288 words of memory would be needed. An additional 10% for reserve would be advisable, making a grand total of 13,516 words.

MULTI-PULSE OPERATION

All of the preceding figures are for the case ofa single laser pulse during each tokamak discharge. In the case of multi-pulse operation, e.g. five pulses during the 20 sec discharge, the memory allocation needed would be correspondingly larger. Also, I(t), V(t), $\emptyset$(t) and E would have to be digitised for each pulse. Similarly, a number of control channels would be activated once for each laser pulse, as well as data transfer being activated after each pulse.

7. COST OF DIAGNOSTIC AND TIME SCHEDULE FOR COMPLETION

In this section we estimate the cost of the diagnostic from its initial development, through the various stages, to commissioning on JET. Also, we draw up a tentative time-table for the progression of the diagnostic from initial development work to commissioning on the tokamak.

7.1 Cost Estimate

In table 7.1.1 we provide a detailed cost estimate for the diagnostic. A cost of S.Fr. 1,850,000 - 2,076,000 is foreseen in total {S.Fr. 3.90 $\simeq$ £ 1.0}. Of this S.Fr. 307,000 - 457,000 are required for development, S.Fr. 49,000 - 69,000 are required for design, S.Fr. 1,392,000 are required for manufacture, construction and assembly, S.Fr. 27,000 - 41,000 are required for testing and calibration, S.Fr. 33,000 - 46,000 are required for transport and installation and S.Fr. 43,000 - 72,000 are required for commissioning on JET. A breakdown of the costs of the hardware is provided in table 7.1.2.

The ranges in the costs for the various stages arise from uncertainties in the man-power requirements for their completion. To the figures quoted, an extra 10% at least should be added to cover the costs of overheads and contingencies. It should be noted that the costs quoted are based on prices which were current at the end of 1979, and that there is no built-in factor to allow for inflation.

7.2 Time Scale for the Diagnostic

A provisional time-table for the progression of the FIR-laser scattering system from initial development to final installation on JET is drawn up in table 7.2.1. It is envisaged that the diagnostic could be installed on the tokamak during the autumn of 1983.

Implicit in the above is the assumption that a contract would be placed with the CRPP in sufficient time to permit adherence to the time table. We estimate that there would be a minimum delay of 18 months after receipt of the contract before the diagnostic would be available for use on JET, and that mid 1982 would be the earliest at which such a contract could be accepted.

Table 7.1.1

Summary of Estimated Costs for JET Diagnostic System No. 15.2 Far Infra-Red scattering

Prepared under JET Contract No. B-Z-412 by Lausanne Laboratory

{All Costs are in Swiss Francs (S.Fr.)}

Phase	Scientific and Engineering Effort			Design and Technical Support			Computing (3)	Travel incl. accommodation	Hardware (1)	Misc. (2)	Total
	Man Years	Cost/ Man Year	Total Cost	Man Years	Cost/ Man Year	Total Cost					
1. Initial Development	4 - 6	55,000	220,000 - 330,000	1 - 2	40,000	40,000 - 80,000	25 hrs 36,000	45 man days 11,000			307,000 - 457,000
2. Detailed Design	0.25	"	13,750	0.5- 1	"	20,000 - 40,000	10 hrs 14,400	5 man days 1,100			49,250 - 69,250
3. Manufacture Construction & Assembly	0.5	"	27,500	0.5	"	20,000		5 man days 1,100	1,343,155		1,391,755
4. Testing and Calibration	0.25-0.5	"	13,750 - 27,500	1 month	"	3,330	5 hrs 7,200	10 man days 2,500			26,780 - 40,530
5. Transport and Installation on JET	1-2 months	"	4,580 - 9,170	1-2 months	"	3,330 - 6,670		2 men full time 6,500 - 11,600		transp. 18,200	32,610 - 45,640
6. Commissioning on JET	0.25-0.5	"	13,750 - 27,500	1 month	"	3,330	5 hrs 7,200	2 men full time 16,700 - 32,000		gas for CO_2 Lasers 2,000	42,980 - 72,030

Notes:
(1) Please provide a separate sheet with a breakdown of Hardware costs into sub-assemblies, e.g. support frame, detectors, electronics, etc.
(2) Please specify any miscellaneous items.
(3) Please include the development of software for controlling the diagnostic and interpreting the data.

These costs estimates will not be used for contractual purposes.

TOTAL COST 1,850,375 - 2,076,205

Table 7.1.2

BREAKDOWN OF HARDWARE COSTS

Item	Cost (S.Fr.)
E-beam CO_2 Laser	529,500
TEA CO_2 Lasers	115,000
Power Supplies	10,000
Trigger Units	5,100
Oscillator Frame (Invar)	8,000
Mounting Frames for TEA Lasers	3,000
Windows, Optics and Holders	41,300
Monitors of Discharges in CO_2 Lasers	2,500
FIR Oscillator	22,730
FIR Amplifier	2,500
Optics and Windows	11,000
Vacuum Pump	6,025
Windows for Torus	9,000
Vacuum Valves for Protection	70,000
Beam Dumps	10,000
Input and Collection Optics and Mounts	17,000
Motors for Controlling Above	80,000
Framework for Input and Collection Optics	20,000
Tubes for Beam Propagation	5,000
Detector plus Mixer	56,000
Laser for Local Oscillator	75,000
Transient Digitisers	200,000
Gas Handling Equipment	2,500
Alignment Laser	16,000
Screened Room	26,000
Total	1,343,155

Table 7.2.1

Time Scale for the Diagnostic

1980-1981 (autumn)	Development Work
1981 (autumn) - 1982	Testing of Diagnostic on TCA
July 1982 - Dec. 1982	Detailed Design for JET
Dec. 1982 - June 1983	Manufacture, Construction and Assembly
June 1983 - September 1983	Testing and Calibration
October 1983 - December 1983	Installation and Commissioning

8. CONCLUDING REMARKS

This study has resulted in the production of a conceptual design for a diagnostic to measure the plasma ion temperature in JET by Thomson scattering using a far-infrared laser.

It is concluded that using existing D_2O lasers and Schottky-diode mixers at 385 μm a measurement of T_i could be performed with an accuracy of $\pm$ 50%. To achieve accuracies of better than $\pm$ 20% it will be necessary to improve the laser performance such that the pulse duration is extended by at least a factor of 10 to $\gtrsim$ 1 μsec, whilst maintaining the power level at around 1 MW.

Using a laser of the above performance, together with a mixer of NEP $\lesssim 3 \times 10^{-19}$ WHz^{-1}, an accuracy of $\pm$ 20% can be achieved in the determination of T_i in JET, over the following ranges of parameters: $n_e = 3 \times 10^{13}$ to 3×10^{14} cm^{-3}, T_i (= T_e) = 3 to 12 keV. For access defined by a pair of large vertical slit ports, a little over half the plasma vertical diameter can be scanned with an average separation of $\sim$ 32 cm between the points of measurement. The achievable spatial resolution should always be better than 20 cm. Multiple pulsing of the FIR laser would permit $\sim$ 10 measurements to be taken during a time interval of $\sim$ 10 sec.

It is apparent that there are a number of points which require further investigation and development before a FIR scattering measurement on JET becomes a practical proposition. The most important of these are :

(a) The D_2O laser performance at 385 μm will need extending to pulses of duration $\gtrsim$ 1 μsec and power 1 MW.

(b) A study of the effects of neutron and γ-ray irradiation on the transmission properties of quartz and glass elements and on fibre-optic cables will be required, so that adequate shielding precautions can be taken during the D-T phase of JET operation.

(c) Rigorous testing will be needed of the optical components and mounts over beam paths which are representative of those on JET, to ensure adequate long-term stability.

(d) A simple and reliable system will have to be developed for the remote checking and adjustment of the various beam paths and optical elements.

(e) The data acquisition and control system software will need developing and testing before the diagnostic is installed on JET.

It is not foreseen that any of the above will present insurmountable obstacles to the successful application of the diagnostic technique to JET.

9. REFERENCES

(1) D.E. Evans and J. Katzenstein, Rep. Prog. Phys. 32, 207, (1969).

(2) D.E. Evans, Plasma Phys. 12, 573, (1970).

(3) E. Holzhauer and J. H. Massig, Plasma Phys. 20, 867, (1978).

(4) P.D. Morgan, M.R. Green, M.R. Siegrist and R.L. Watterson, Comments on Plasma Physics and Controlled Fusion 5, 141, (1979).

(5) D.E. Evans, Physica 82C, 27, (1976).

(6) T.G. Blaney, J. Phys. E: Sci. Instrum. 11, 856, (1978).

(7) T.Y. Chang, IEEE Trans. Microwave Theory Tech. MTT-22, 983, (1974).

(8) D.T. Hodges, Infrared Phys. 18, 375, (1978).

(9) D.T. Hodges, Proceedings of the Second International Conference on Infrared Physics (Zurich, 1979), p. 50.

(10) M. Rosenbluh, R.J. Temkin and K.J. Button, Appl. Opt. 15, 2635, (1976).

(11) J.J. Gallagher, M.D. Blue, B. Bean and S. Perkowitz, Infrared Phys. 17, 43, (1977).

(12) S.J. Petuchowski, A.T. Rosenberger and T.A. De Temple, IEEE J. Quant. Electr. QE-13, 476, (1977).

(13) G.W. Chantry, Submillimetre Spectroscopy, (Academic Press, New York, 1971), p. 291.

(14) J.D. Wiggins, Z. Drozdowicz and R.J. Temkin, IEEE J. Quant. Electr. QE-14, 23, (1978).

(15) F. Keilmann, R.L. Sheffield, J.R.R. Leite, M.S. Feld and A. Javan, Appl. Phys. Lett. 26, 19, (1975).

(16) T.L. Worchesky, K.J. Ritter, J.P. Sattler and W.A. Riessler, Opt. Lett. 2, 70, (1978).

(17) P. Woskoboinikow, H.C. Praddaude, W.J. Mulligan, D.R. Cohn and B. Lax, J. Appl. Phys. 50, 1125, (1979).

(18) P. Woskoboinikow, H.C. Praddaude, W.J. Mulligan and D.R. Cohn, Conference Digest of Fourth International Conference on Infrared and Millimeter Waves and Their Applications (Miami, 1979), p. 237.

(19) A.E. Siegman, Laser Focus, 42, (May 1971).

(20) B. Hawker, Specac Ltd., Orpington, U.K. Private communication.

(21) M.R. Green, I. Kjelberg, P.D. Morgan, M.R. Siegrist, R.L. Watterson and E. Akhmetov, J. Phys. D: Appl. Phys. 13. To be published, (1980).

(22) A. Gondhalekar, E. Holzhauer and N.R. Heckenberg, Phys. Lett. 46A, 229, (1973).

(23) L.C. Johnson, Plasma Physics Lab., Princeton University. Private communication.

(24) D.A. Reynolds, T. Stamatakis and A.C. Walker, Proceedings of Fourth National Quantum Electronics Conference (Edinburgh, 1979), paper 14.

(25) M.R. Green, P.D. Morgan and M.R. Siegrist, Ecole Polytechnique Fédérale de Lausanne, Switzerland, Report LRP 141/78, (1978).

(26) A.E. Siegman, An Introduction to Lasers and Masers, (McGraw-Hill Book Co., New York, 1971), p. 334.

(27) J.P. Nicholson and K.S. Lipton, Appl. Phys. Lett. 31, 430, (1977).

(28) Krytron High Voltage Square Wave Generator, Application Note K5502B-2, EG&G Electro-Optics Div., Salem, Mass., (1975).

(29) P.D. Morgan, CRPP Internal Memorandum, CRPP INT/99/80, (1980).

(30) D. Andreou and V.I. Little, Opt. Commun. 6, 180, (1972).

(31) L.M. Franz and J.S. Nodvick, J. Appl. Phys. 34, 2346, (1963).

(32) A.C. Walker, UKAEA Culham Laboratory, Abingdon. Private communication.

(33) J. de Melo, The Harshaw Chemical Co., Crystal and Electronics Products, Solon, Ohio. Private communication.

(34) S. J. Czuchlewski, A.V. Nowak, E. Foley and J.F. Figueira, Opt. Lett. 2, 39, (1978).

(35) H. Fujita, Annual Progress Report on Laser Fusion Program 1977-78 (ILE-APR-78), Institute of Laser Engineering, Osaka University, 67, (1978).

(36) M.R. Green, P.D. Morgan, M.R. Siegrist, R.L. Watterson, M.A. Dupertuis, I. Kjelberg, J.L. Scartezzini, R. Duperrex and H. Van den Bergh, J. Phys. D: Appl. Phys. 13. To be published, (1980).

(37) P. Woskoboinikow, H.C. Praddaude and W. J. Mulligan, Opt. Lett. 4, 201, (1979).

(38) R.H. Kingston, Detection of Optical and Infrared Radiation, (Springer, New York, 1978), p. 13.

(39) A.T. Forrester, J. Opt. Soc. Amer. 51, 253, (1961).

(40) H.R. Fetterman, B.J. Clifton, P.E. Tannenwald and C. D. Parker, Appl. Phys. Lett. 24, 70, (1974).

(41) M. McColl, IEEE Trans. Microwave Theory Tech. MTT-25, 54, (1977).

(42) G.T. Wrixon, ESA Journal 3, 201, (1979).

(43) B.T. Ulrich, Infrared Phys. 18, 429, (1978).

(44) B.T. Ulrich, Infrared Phys. 17, 467, (1977).

(45) P.L. Richards, Semiconductors and Semimetals 12, ed. R.K. Willardson and A.C. Beer, (Academic Press, New York, 1977), ch. 6.

(46) T.I. Smith, J. Appl. Phys. 45, 1875, (1974).

(47) D.J.E. Knight and P.T. Woods, J. Phys. E: Sci.Instrum. 9, 898, (1976).

(48) T.G. Blaney, Rev. Phys. Appl. 9, 279, (1974).

(49) Y. Taur and A.R. Kerr, Appl. Phys. Lett. 32, 775, (1978).

(50) E. Gornik, Institute of Experimental Physics, University of Innsbruck. Private communication.

(51) E.E. Haller, M.R. Hueschen and P.L. Richards, Appl. Phys. Lett. 34, 495, (1979).

(52) B.T. Ulrich, IPP Garching. Private communication.

(53) H.R. Fetterman, P.E. Tannenwald, C.D. Parker, J. Melngailis, R.C. Williamson, P. Woskoboinikow, H.C. Praddaude and W.J. Mulligan, Appl. Phys. Lett. 34, 123, (1979).

(54) H.Z. Cummins and H.L. Swinney, Progress in Optics 8, ed. E. Wolf, (North Holland, Amsterdam, 1970), ch. 3.

(55) S. Brandt, Statistical and Computational Methods in Data Analysis, (North Holland, Amsterdam, 1970), p. 87.

(56) W.D. Stanley, Digital Signal Processing, (Reston Publishing Co., Reston VA, 1975), p. 48.

(57) H. Kräutle, E. Sauter and G.V. Schultz, Infrared Phys. 17, 477, (1977).

(58) J. Hugill, S.J. Fielding, R.D. Gill, M. Hobby, G.M. McCracken, J.W.M. Paul, N.J. Peacock, B.A. Powell, R. Prentice and P.E. Stott, Proc. 8th Europ. Conf. on Controlled Fusion and Plasma Physics 1, 39, (1977).

(59) G. Magyar and P.E. Stott, JET Diagnostic Memo. 1, (1979).

(60) A.E. Costley, National Physical Laboratory, Teddington. Private communication.

(61) S. Glasstone and R.H. Lovberg, Controlled Thermonuclear Reactions (Van Nostrand, Princeton, 1960), p. 32.

(62) A. Semet, A. Mase, W.A. Peebles and N.C. Luhmann, Jr., Conference Digest of Fourth International Conference on Infrared and Millimeter Waves and Their Applications (Miami, 1979).

(63) R.E. Slusher and C.M. Surko, Phys. Fluids 23, 472, (1980).

(64) A.D. Cheetham, A. Heym, F. Hofmann, K. Hruska, R. Keller, A. Lietti, J.B. Lister, A. Pochelon, H. Ripper, R. Schreiber and A. Simik, Ecole Polytechnique Fédérale de Lausanne, Switzerland, Report LRP 162/80, (1980).

(65) E.E. Russell and E.E. Bell, J. Opt. Soc. Amer. 57, 341, (1967).

(66) N. Coron, J.P. Moalic, G. Dambier and J.P. Baluteau, Infrared Phys. 20, 53, (1980).

(67) G. Magyar, JET, Abingdon. Private communication.

(68) M.F. Kimmitt, Far-Infrared Techniques, (Pion Ltd., London, 1970), p. 29.

(69) H. Kogelnik and T. Li, App. Opt. 5, 1550, (1966).

10. ACKNOWLEDGEMENTS

It is a pleasure to acknowledge the continuing support given to the FIR-scattering project at Lausanne, and the encouragement given during the course of this design study, by A. Heym and E.S. Weibel of the CRPP.

The section concerning Josephson-junction detectors was written in conjunction with B.T. Ulrich of IPP Garching, from whom much useful knowledge concerning the detection of FIR radiation has been gained.

The authors are grateful for illuminating discussions with G.T. Wrixon of Cork University, with F. Troyon and J. Vaclavik of CRPP Lausanne, with D.E. Evans, A.C. Selden, T. Stamatakis and A.C. Walker of UKAEA Culham Laboratory, with G. Magyar and T.E. Stringer of JET, and with G. Dodel of Stuttgart University.

Much useful information concerning the workings of E-beam CO_2 lasers has been obtained from Systems, Science and Software, Hayward, CA, while P. Woskoboinikow of the Francis Bitter National Magnet Laboratory, MIT has supplied us with his most recent, and in most cases unpublished, results on D_2O lasers. We are very grateful for this assistance.

This work has been partly supported by the Swiss National Science Foundation.